

Analytical Modeling of Piezo-SMA Composite
as an Actuator and Energy Harvester

Onur Cem Namli

A dissertation
submitted in partial fulfillment of the
requirements for the degree of

Doctor of Philosophy

University of Washington
2012

Reading Committee:

Minoru Taya, Chair

Jiangyu Li

Yuanchang Liang

Program Authorized to Offer Degree:
Department of Mechanical Engineering

University of Washington

Abstract

Analytical Modeling of Piezo-SMA Composite as an Actuator and Energy Harvester

by Onur Cem Namli

Chair of the Supervisory Committee:
Professor Minoru Taya
Department of Mechanical Engineering

Piezoelectric materials and shape memory alloys (SMAs) are very common materials for actuators and sensors; however their composites as electrical generators are least explored, although the use of piezoelectric materials as the mechanical energy harvester is becoming popular. In this dissertation piezoelectric material and SMA are used as constituents for an active composite of two types; one is a composite of piezoelectric material and SMA as an actuator and the second one is a composite as a thermal energy harvester. The analytical modeling and experimental study related to Piezo-SMA active composites are examined for both cases. Eshelby's inclusion problems are combined into a single model to treat the coupled behavior of electro-mechanics inherent in the piezo-SMA composite where the piezo is matrix phase and SMA is filler phase. SMA undergoes phase transformation such as stress-induced martensite transformation and temperature induced austenite transformation. Basic design and experimental work done on active composite are discussed in the areas of material characterization and mechanical modeling.

TABLE OF CONTENTS

TABLE OF CONTENTS.....	I
LIST OF FIGURES.....	III
ACKNOWLEDGEMENTS	VII
CHAPTER 1. MOTIVATION AND INTRODUCTION	1
1.1. MOTIVATION.....	1
1.2. INTRODUCTION	4
1.3. PIEZOELECTRICITY.....	9
1.3.1. <i>Piezoelectricity Mechanism</i>	9
1.3.2. <i>Direct Effect</i>	11
1.3.3. <i>Converse Effect</i>	12
1.3.4. <i>Examples of Piezo Actuators</i>	13
1.3.5. <i>Examples of Piezo Sensors</i>	22
1.4. ENERGY HARVESTING BY PIEZOELECTRICITY	28
1.5. SHAPE MEMORY ALLOYS (SMAS)	32
CHAPTER 2. MODELING OF PIEZOELECTRIC - SHAPE MEMORY ALLOY COMPOSITE AS A FAST RESPONSIVE ACTUATOR MATERIAL	40
2.1. MODELING ELECTROMECHANICAL COUPLING WITH ESHELBY’S THEORY	41
2.1.1. <i>Mixed Boundary Condition Problem</i>	46
2.1.2. <i>Stress-only Boundary Condition</i>	47
2.1.3. <i>E-Field Boundary Condition</i>	50
2.2. ONE-DIMENSIONAL MODEL BASED ON PARALLEL CONNECTION	51
2.2.1. <i>Analysis of a composite under applied stress only</i>	52
2.2.2. <i>Analysis of a composite under both applied stress and electric field</i>	54
2.3. ONE-DIMENSIONAL MODEL BASED ON SERIAL CONNECTION.....	56
2.4. THE STIFFNESS PROPERTIES OF THE PIEZO-SMA COMPOSITE.....	58

2.5. THE EXPERIMENTAL STUDY TO FABRICATE THE PIEZO-SMA LAMINATED COMPOSITE	68
2.6. RESULTS AND DISCUSSION	75
CHAPTER 3. THE PIEZO-SMA COMPOSITE FOR THERMAL ENERGY HARVESTING	80
3.1. ANALYTICAL MODEL OF THE PIEZO-SMA ENERGY HARVESTER.....	81
3.1.1. <i>One-Dimensional Modeling</i>	83
3.1.2. <i>Three-Dimensional Modeling with Eshelby's Theory</i>	88
3.1.3. <i>3-D Modeling with Superposition Principle</i>	93
3.2. SHAPE MEMORY ALLOY (SMA) MATERIAL CHARACTERIZATION.....	104
3.3. ELECTRICAL MODEL.....	111
3.4. EXPERIMENTAL STUDY.....	115
3.5. PIEZOELECTRIC MATERIAL (PZT) CHARACTERIZATION	118
3.6. EXPERIMENTAL PROCEDURE	130
CHAPTER 4. CONCLUSIONS.....	142
REFERENCES.....	144

LIST OF FIGURES

Figure 1.1. Interaction between mechanical, thermal and electrical properties, Ikeda (1990), Taya (2005).	6
Figure 1.2. Current measurement of a NLC cell setup (Marino et al., 2007).	10
Figure 1.3. The effect of a force on a piezoelectric material.	12
Figure 1.4. Deformation of a piezoceramic material when voltage is applied.	13
Figure 1.5. (a) Schematic of test facility to measure direct ME response. (b) Sample holder with the suspended composite under test (Record et al., 2007). ...	14
Figure 1.6. Diagram showing ceramic multilayer actuator and its measurement using X-ray diffractory and laser vibrometer (Jeong et al., 2004).....	16
Figure 1.7. Diagram showing the internal stress configuration in the inner structure of multilayer actuator subjected to an electric field along x_3 axis. The electric energy driven by electric field exerts mechanical elongation along x_3 axis and contraction along x_1 axis (Jeong et al., 2004).	17
Figure 1.8. A schematic of piezoelectric bimorph grasper in the (a) open and (b) fully-closed positions (Grujicic et al., 2005).	18
Figure 1.9. Types of super-helix, or “coiled coil” whose size can be compared to British coins: (a) a flat toroidal coiled coil; (b) two coiled coils of different sizes and multiple turns (Seffen, 2007).	20
Figure 1.10. Proposed 2 d.o.f. wing mechanism translating and rotating a folded polymer wing using two independently actuated parallel four-bar structures, and its kinematic and force parameters (Sitti, 2003).	21
Figure 1.11. Four-bar design proposal for enabling very high stroke amplification if necessary (Sitti, 2003).	22
Figure 1.12. The piezoelectric tube mounted inside an aluminum shield. The x-axis capacitive sensor is shown secured at right angles to a cube mounted onto the tube tip. And the y-axis capacitive sensor is secured at right angles to the perpendicular face of the aluminum cube (Bhikkaji et al., 2007).....	23
Figure 1.13. Fatigue characteristics of PZT and PNZT (2 at.%) films (Cimaa and Remiens, 2005).	25
Figure 1.14. Scanning electron micrograph of a large clump of virus particles attached to a cantilever beam, scale bar is 1 μm (Johnson et al., 2006).	27
Figure 1.15. Plain view of accelerometer layout (Beeby et al., 2001).....	28
Figure 1.16. Three major phases associated with piezoelectric energy harvesting. [Uchino and Ishii, 2010]	29
Figure 1.17. Superelastic behavior in SMA (Lagoudas, 2008).....	33
Figure 1.18. Shape Memory Effect in a stress-strain-temperature space and the respective microstructures of a typical NiTi SMA material (Lagoudas, 2008).....	34
Figure 1.19. Four phase transformation temperatures shown on temperature axis (Simsek, 2009).	36

Figure 1.20. Lattice shapes and deformation mechanisms of shape memory alloys under different inputs (Mok, 2003).....	37
Figure 2.1. Analytical model for piezoelectric composite containing non-piezoelectric SMA fillers, (a) original problem, which is converted to (b) Eshelby's equivalent inclusion problem.	43
Figure 2.2. Bi-linear stress-strain curve of SMA.	49
Figure 2.3. Composite with 1-D parallel connection is subjected to applied stress, where h_s and h_p represent the thicknesses of SMA-phase and piezo-phase, respectively.	52
Figure 2.4. Free-body diagram showing forces acting on piezo and SMA layers of 1-D parallel model.	52
Figure 2.5. Free-body diagram of the composite with applied stress and electric field.	54
Figure 2.6. Composite with 1-D series connection is subjected to an applied stress, where h_p and h_s represent the thicknesses of PZT and SMA layers, respectively.	57
Figure 2.7. Stress-Strain curve of a SMA composite where the first and the third stages are 100% austenite and 100% martensite phase respectively, and the second stage is a mixture of both phases.	59
Figure 2.8. (a) Piezo-SMA composite and (b) equivalent Eshelby's inclusion problem for analysis of the first and the third stages in Stress-Strain diagram.	60
Figure 2.9. Eshelby's inhomogeneity inclusion problem for the simulation of the second stage behavior of Stress-Strain curve of a SMA composite.	64
Figure 2.10. Schematic view of Spark Plasma Sintering (SPS) machine.	69
Figure 2.11. Schematic view for preparing the specimen for SPS process.	70
Figure 2.12. Cross section of PZT-NiTi laminated composite.	72
Figure 2.13. Poling setup for Piezo-SMA laminated composite.	75
Figure 2.14. Total strain of the piezo-SMA composite with applied electric field.	77
Figure 2.15. Total strain of the piezo-SMA composite with applied electric field for different volume fractions of SMA phase, by using 3-D model with Eshelby's theory.	78
Figure 3.1. Modeling of Piezo-SMA composite.	84
Figure 3.2. Schematic Stress-Strain curve of SMA to introduce prestrain, ϵ^{TR} . . .	86
Figure 3.3. Analytical model for predicting residual stresses in SMA filler and piezo matrix, (a) original problem is converted to (b) Eshelby's equivalent inclusion problem.	89
Figure 3.4. Free energy – Temperature diagram of SMA.	94
Figure 3.5. Stress–Strain curve for SMA which is at martensite phase.	96
Figure 3.6. Schematic view of 2-phase Piezo-SMA composite with fixed displacement boundary condition.	96

Figure 3.7. Temperature - Stress for heating cycle of Piezo-SMA composite.	97
Figure 3.8. Temperature vs. Stress for cooling cycle of Piezo-SMA composite..	98
Figure 3.9. Stress-strain curve for SMA at a temperature higher than Austenite transformation finish temperature.....	99
Figure 3.10. Original problem can be solved by superposition principle.....	99
Figure 3.11. Original problem converted into Eshelby's equivalent inclusion problems.....	100
Figure 3.12. Martensite volume fraction as a function of Temperature of Piezo-SMA composite.....	103
Figure 3.13. Setup used for homogenization of NiTi based SMA.....	105
Figure 3.14. DSC result of 51.2Ti-48.8Ni (at.%) SMA.....	106
Figure 3.15. Stress-Strain response of 51.2Ti-Ni (at.%) SMA, at 300K	107
Figure 3.16. Effective piezo stress based on 1-D model as a function of temperature (Namli and Taya, 2011).....	109
Figure 3.17. Effective piezo stress based on 3-D model with Eshelby's Theory as a function of temperature (Namli and Taya, 2011).	110
Figure 3.18. Martensite volume fraction of the piezo-SMA composite during thermal cycling based on 3-D model with Eshelby's Theory.....	111
Figure 3.19. Schematic representation of PZT that is connected to electrical loading.....	117
Figure 3.20. Voltage and Current response for 0.01 Hz, 2kN loading	119
Figure 3.21. Average power at the electrical load for different electrical loading 0.01 Hz, 2kN loading	120
Figure 3.22. Voltage and Current response for 0.05 Hz, 2kN loading	122
Figure 3.23. Average power at the electrical load for different electrical loading 0.05 Hz, 2kN loading	123
Figure 3.24. Voltage and Current response for 0.1 Hz, 2kN loading	124
Figure 3.25. Average power at the electrical load for different electrical loading 0.1 Hz, 2kN loading	125
Figure 3.26. Voltage and Current response for 0.5 Hz, 2kN loading	126
Figure 3.27. Average power at the electrical load for different electrical loading 0.5 Hz, 2kN loading	127
Figure 3.28. Average power at the electrical load for all frequency conditions in logarithmic scale, with respect to load resistance.....	128
Figure 3.29. Average power at the electrical load for small frequency conditions with respect to load resistance	129
Figure 3.30. Schematic representation of the Piezo-SMA composite module in thermal energy harvesting experiment.....	130
Figure 3.31. Temperature cycle simulation for piezo-SMA thermal energy harvester	132
Figure 3.32. Output voltage and Temperature results for Thermal Cycling process, 0.01 Hz	133

Figure 3.33. Experimental setup for piezo-SMA composite subjected to thermal cycling.....	134
Figure 3.34. Experimental setup to simulate thermal cycling with the use of Instron machine that creates zero displacement boundary condition. (a) Piezo only, (b) Piezo-SMA Laminate.....	136
Figure 3.35. Temperature and Voltage response for 0.05 Hz and 0.1 Hz experimental study (Namli and Taya, 2011).....	138

ACKNOWLEDGEMENTS

First and foremost I offer my sincerest gratitude to my supervisor, Dr. Minoru Taya, who has supported me throughout my graduate program with his patience and knowledge whilst allowing me the room to work in my own way. I would like to thank Dr. Yuanchang Liang, who shared his knowledge in shape memory alloys and taught me all the experimental devices that I used throughout my research within the lab, CIMS. I would also like to thank Prof. Tsutomu Mori and former research associates, Dr. Hiro Nakayama, Dr. Keiko Kikuchi, Dr. Hiroshi Sato, Dr. Miseon Choi for guiding my research for the past several years and helping me to develop my background.

I would like to express my very great appreciation to AFOSR (grants FA 9550-09-01-0584 and FA 9550-06-01-0326) for the support in this dissertation, also to University of Washington Mechanical Engineering, Chemical Engineering, and Physics and Astronomy Departments for helping me to develop my teaching background throughout my study.

I would also like to thank my parents and my sister. They were always encouraging me with their best wishes all the way from Istanbul.

I would like to thank Mr. Omer Yetemen who as a good friend and a roommate was always willing to help and give his best suggestions. Many thanks to Mr. Ahmet Keles who as a good friend was there for me when the times were tough. It would have been a difficult time without them.

I would to take the opportunity to thank my former employer, Assan Aluminum, for giving me a warm and a friendly work environment with lots of real life experiences learned.

I want to thank all the people that I spent time with here in Seattle on this journey. They are on their way with my best wishes.

Chapter 1. Motivation and Introduction

1.1. Motivation

Piezoelectric materials and shape memory alloys (SMAs) are very common materials for actuators and sensors; however their composites as electrical generators are least explored, although the use of piezoelectric materials as the mechanical energy harvester is becoming popular. In this dissertation piezoelectric material and SMA are used as constituents for an active composite of two types; one is a composite of piezoelectric material and SMA as a fast responsive actuator and the second one is a composite as a thermal energy harvester. The analytical modeling and experimental study related to Piezo-SMA active composite are examined in Chapter 2 for actuator material and in Chapter 3 for thermal energy harvester.

In piezoelectric materials, the speed of actuation and sensing is fast, but the order of induced strain is modest while SMA exhibits larger strain, but has much slower speed of actuation. When two materials are combined to form a composite, which is called as piezo-SMA composite, one would expect a unique property to arise. This is the original motivation of the study related to active composite as an actuator; the modeling and the experimental study carried out for the composite structure are summarized in Chapter 2 of the dissertation.

Thermal energy harvester using piezo-SMA composite is also modeled in the second part of the study, i.e. Chapter 3. Composite is subjected to fluctuating temperature where the boundary conditions are described in details in the modeling part. The main mechanism of such a piezo-SMA composite is synergistic effect of piezoelectric material and SMA, which are connected in series. The composite is then subjected to fluctuating temperature which induces large strain first in the SMA phase, then immediately inducing stress to the piezoelectric phase, thus, generating charge by direct piezoelectric effect. In order to make this problem more analytically traceable, two models of the composite is examined in Chapter 3; simple laminated model and 3-D Model with Eshelby's theory.

In both actuator and thermal energy harvester parts, Eshelby's inclusion problems are combined into a single model to treat the coupled behavior of electro-mechanics inherent in the piezo-SMA composite where the piezo phase is matrix and SMA phase is filler. SMA phase can undergo phase-change such as stress-induced martensite transformation and temperature induced austenite transformation.

In the chapter 2, three dimensional (3-D) model with Eshelby's theory for piezo-SMA composite is examined, then, a simpler case; one dimensional (1-D) parallel laminated model is discussed. In 1-D laminated model, both piezoelectric material and SMA are assumed to have perfect bonding between each other. A stress so

called bias stress is applied to initiate martensitic transformation in the SMA phase; at this point an additional stress which can be induced by applying electrical field to piezoelectric phase is expected to induce more stress on SMA phase and cause a large strain in the active composite.

In Chapter 3 where piezo-SMA composite is examined as a thermal energy harvester, composite is modeled as materials of two discs, one of piezoelectric ceramic and the other of SMA material. The materials are connected in series and constrained together to have zero displacement boundary condition is applied. Since the composite is modeled to have zero displacement boundary condition, the piezoelectric material is in compression throughout the process. Temperature fluctuation between martensite finish temperature (M_F) and austenite finish temperature (A_F) induces phase transformation in the SMA. Compressive stress is induced during Austenitic transformation; due to heating in SMA phase with fixed displacement boundary condition, compressive stress reduces while SMA transforms to martensitic phase during cooling. The change in the compressive stress is converted into electrical energy by inverse piezoelectricity by the piezo electric phase of the composite. The model predicts the available power amount according to the properties of materials and thermal fluctuation. The impedance of the system is examined with different thermal fluctuating frequencies. Higher frequencies which result in lower impedance give more power available to electrical loading. The experimental and predicted results are in agreement for

higher frequencies; however the prediction is not accurate for lower frequencies of thermal fluctuation due to the internal loss.

1.2. Introduction

An “active composite” should be distinguished from a conventional composite that is primarily used in structural design as a main material. An active composite can be manufactured to control its shape when subjected to different loads with different boundary conditions. One or more constituents of an active composite and hence the composite itself exhibits coupling between at least two of the following three effects: mechanical, thermal, and electrical, see Fig.1.1. Thus, besides the polymer matrix, other constituents of an active composite can be a piezoceramic, a shape memory alloy, and/ or a magnetostrictive material. A variety of piezoelectric composite materials, usually called piezocomposites, can be made by combining a piezoelectric ceramic (PZT) with either a non-piezoelectric or a piezoelectric phase. Measurements showing the potential for improvement in the performance of naval hydrophones provided a major impetus to research on piezocomposites (Harrison, 1976).

Piezocomposites have been used as electromechanical and medical ultrasonic imaging transducers. They are more suitable for damage monitoring due to the ease with which their mechanical properties can be manufactured and better impedance matching with that of the host structure. By changing the shape, the size, the volume fraction of the piezoelectrics, and the material of the other phases,

a cost-effective piezo-composite with the desired electromechanical coupling constants and impedance can be manufactured. Newnham et al.'s (1978, 1980) connectivity theory characterized piezocomposites according as the phases are connected in series or in parallel. They also determined the effective properties of these composites. Banno (1983) extended their analyses to discontinuous PZT fibers, and Smith and Auld (1991) to continuous PZT fibers by studying the thickness-mode oscillations in thin plates of 1–3 piezocomposites. Badcock and Birt (2000) have proposed a technique used to prepare and pole 0–3 piezocomposites, and have also computed their electromechanical properties.

One way that researchers used to compute effective properties of a piezocomposite is to use the Eshelby tensor for a PZT inclusion in an infinite matrix. Several researchers, Deeg (1980), Wang (1992), Dunn and Taya (1993), Chen (1994), Hwang and Yu (1994), Jiang et al. (1997), have derived Eshelby tensors for piezocomposites. Li (1998) extended the Eshelby formulation to anisotropic coupled field among elastic, electric, and magnetic properties and derived Eshelby tensor explicitly for two simple geometries of inclusion; elliptical cylindrical and penny-shaped inclusions. If both the matrix and the inclusions exhibit coupled electromechanical properties, then the Eshelby tensor is expressed in terms of four Green's functions which are difficult to obtain in closed form. Dunn and Taya (1993) considered ellipsoidal PZT inclusions in a non-piezoelectric elastic matrix and used various micromechanics models to study their electromechanical properties. Dunn (1994) proved that a piezocomposite can exhibit pyroelectric

effects even though neither of its constituents is pyroelectric. He also estimated the effective thermal expansion and pyroelectric coefficients of a two-phase pyroelectric composite (Dunn, 1993b).

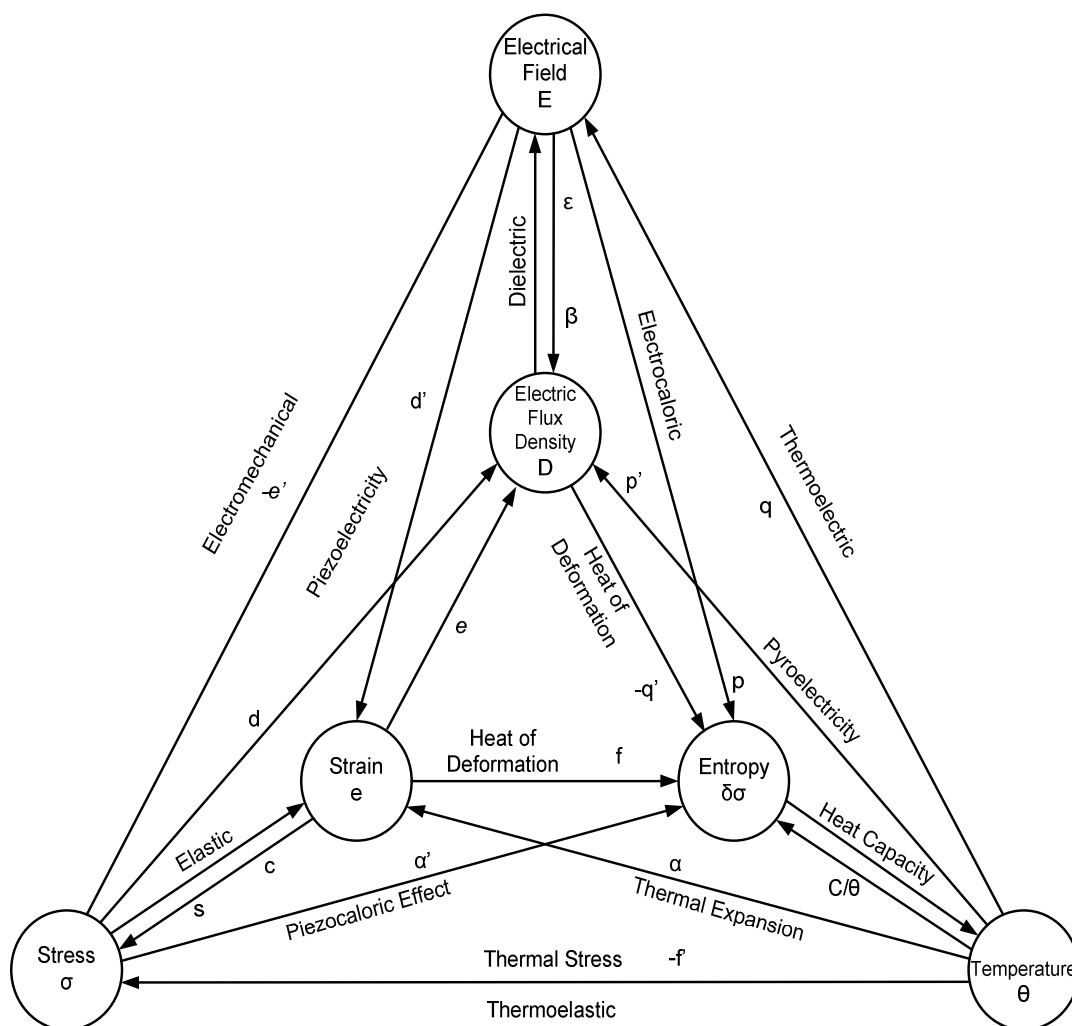


Figure 1.1. Interaction between mechanical, thermal and electrical properties, Ikeda (1990), Taya (2005).

The interactions among densely distributed inclusions or inhomogeneities are usually approximated by the Mori–Tanaka (1973) mean field approach. For small concentrations of inclusions, one can use the rule of mixtures to compute the effective properties of a piezocomposite. An alternative to these analytical techniques is to numerically analyze deformations of a representative volume element of a piezocomposite, and determine material properties of an equivalent homogenized system, Gabbert et al. (1999). Li et al. (1999) obtained the exact thermal properties and piezoelectric properties of a polycrystalline piezoelectric material by assuming a uniform field where the properties of texture orientation is affecting the material properties.

Piezoelectric materials have the ability to be used as mechanisms to transform mechanical energy into electrical energy that can be used to generate power for other devices. Mechanical stresses applied to piezoelectric materials distort internal dipole moments and generate electrical potentials (voltages) in direct proportion to the applied forces. These same crystalline materials also lengthen or shorten in direct proportion to the magnitude and polarity of applied electric fields. The practice of harnessing energy around a system and converting it into usable power is termed power harvesting.

Power harvesting from piezoelectric materials has been investigated for several different potential applications. Many researchers have looked at utilizing the energy loss from a biological activity to provide energy for electronic devices.

Several recent studies have investigated piezoelectric power generation. One study used lead zirconate titanate (PZT) wafers and flexible, multilayer polyvinylidene fluoride (PVDF) films inside shoes to convert mechanical walking energy into usable electrical energy, Kymissis et al. (1998), Shenck et al. (2001). This system has been proposed for mobile computing and was ultimately able to provide continuously 1.3 mW of power at 3V when walking at a rate of 0.8 Hz.

Other projects have used piezoelectric films to extract electrical energy from mechanical vibration in machines to power MEMS devices, Glynn-Jones et al. (2001). This work extracted a very small amount of power ($< 5\mu\text{W}$) from the vibration and no attempt was made to condition or store the energy. Similar work has extracted slightly more power ($\approx 70\ \mu\text{W}$) from machine and building vibrations, Roundy (2002).

Piezoelectric materials have also been studied to generate electricity from pressure variations in microhydraulic systems, Hagood et al. (1999). The power would presumably be used for MEMS but this work is still in the conceptual phase. Other work has used piezoelectric materials to convert kinetic energy into a spark to detonate an explosive projectile on impact, Engel (2000). Still other work has proposed using flexible piezoelectric polymers for energy conversion in windmills, Hugo Schmidt (1992), and to convert flow in oceans and rivers into electric power, Taylor et al. (2001).

The above studies have all successful applications in extracting electrical power from piezoelectric elements. This dissertation presents a theoretical analysis of piezoelectric power generation that is not presented before by using piezoelectric material and Shape Memory Alloy (SMA) together as a hybrid composite.

1.3. Piezoelectricity

Piezoelectricity is the phenomenon whereby electric polarization is generated in certain acentric crystals when they are subjected to mechanical stress, which is known as *the direct effect* in piezoelectricity. Materials showing this phenomenon must also show a geometrical strain, which is proportional to the applied electric field, which is known as *the converse effect* in piezoelectricity. Natural crystals such as quartz, tourmaline, and zinblende are the classical piezoelectric materials. For many years, these materials have served as transducers for converting mechanical energy into electrical energy and vice versa. In general, natural crystals have rather low piezoelectric coefficients. Ceramic piezoelectric materials were developed in the second half of the 20th century and have been constantly improved since then. Modified lead zirconate titanate [Pb(Zr, Ti)O₃] ceramics (commonly known as PZT) are the leading materials for piezoelectric applications such as actuators and sensors.

1.3.1. Piezoelectricity Mechanism

There is a growing interest in thin films of PZT (lead zirconium titanate PbZr_{0.47}Ti_{0.53}O₃) because of their potential applications. For instance, the insertion

of PZT in asymmetric nematic liquid crystal cells induces a rectified electro-optical response similar to that observed in such cells because of the insertion of metal oxide layers with ionic conductivity. Several PZT films have been investigated, obtained by different thermal treatments after sol-gel synthesis and spin coating deposition by Marino et al., 2007. The observed rectifying effect, due to the insertion of PZT films in asymmetric liquid crystal cells, has been attributed to the presence of an internal field made from the reorientation of nanodomains of PZT. The presence of such internal fields is demonstrated and an estimation of it is given. Moreover, asymmetric nematic liquid crystal (NLC) cells made with PZT films show considerable improvements in both contrast and response time.

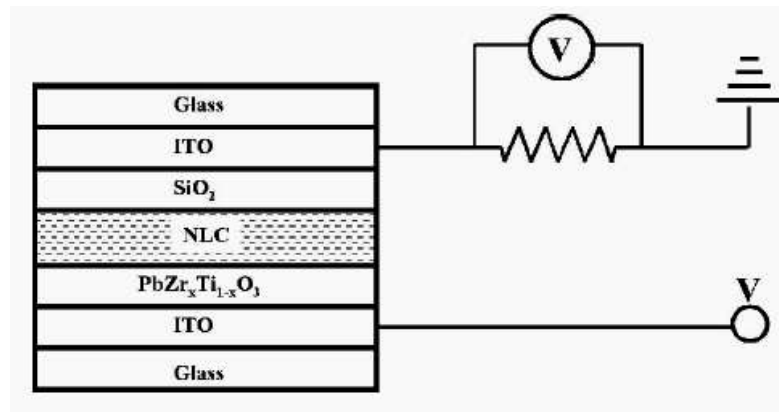


Figure 1.2. Current measurement of a NLC cell setup (Marino et al., 2007).

The insertion of a ferroelectric layer in NLC cells constitutes an alternative method for driving the liquid crystal response by an external voltage, shown in Fig 1.2. In fact, by inducing a polar orientation of the ferroelectric film, it is possible to generate a permanent internal field opposite (in polarity) to the external field,

without any charge migration. Thin films of PZT are attracting the interest of many researchers because of their application in nonvolatile memories. The properties of such ferroelectric materials have been considered in the last 10 years, taking into account problems such as elastic and dielectric properties, polarization fatigue, aging, field and frequency dependence of the piezoelectricity (Dana et al., 1991, Lin et al., 1992 and Damjanovic, 1998)

1.3.2. Direct Effect

Mechanical compression or tension on a poled piezoelectric ceramic element changes the dipole moment, creating a voltage. Compression along the direction of polarization, or tension perpendicular to the direction of polarization, generates voltage of the same polarity as the poling voltage. Tension along the direction of polarization, or compression perpendicular to the direction of polarization, generates a voltage with polarity opposite that of the poling voltage, see Fig.1.3. These actions are generator actions called as direct effect. The ceramic element converts the mechanical energy of compression or tension into electrical energy. This behavior is used in fuel-igniting devices, solid-state batteries, force-sensing devices, and other products. Values for compressive stress and the voltage (or field strength) generated by applying stress to a piezoelectric ceramic element are linearly proportional to a material-specific stress.

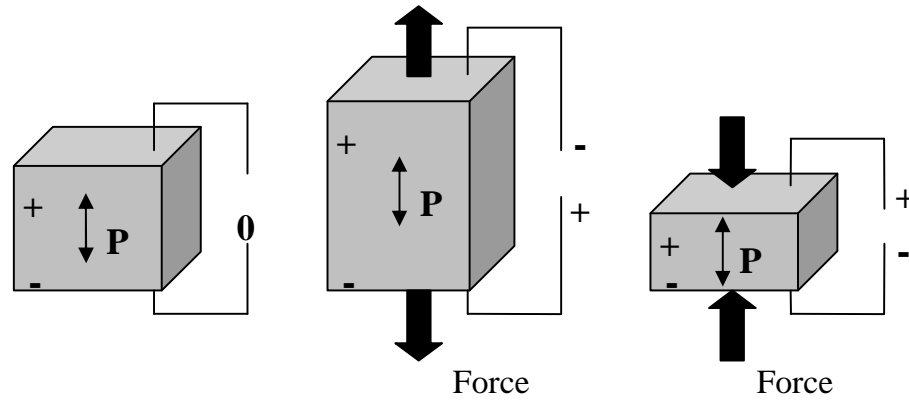


Figure 1.3. The effect of a force on a piezoelectric material.

1.3.3. Converse Effect

If a voltage of the same polarity as the poling voltage is applied to a piezoceramic element, in the direction of the poling voltage, the element will lengthen and its diameter will become smaller. If a voltage of polarity opposite that of the poling voltage is applied, the element will become shorter and broader, see Fig.1.4. If an alternating voltage is applied, the element will lengthen and shorten cyclically, at the frequency of the applied voltage. This motor action is called converse effect, and electrical energy is converted into mechanical energy. The principle is adapted to piezoelectric motors, sound or ultrasound generating devices, and many other products.

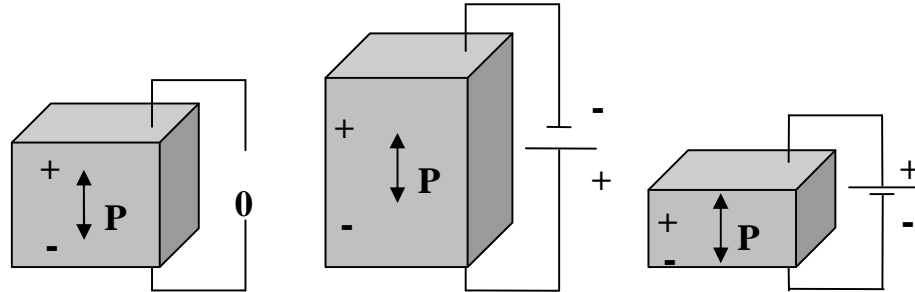


Figure 1.4. Deformation of a piezoceramic material when voltage is applied.

1.3.4. Examples of Piezo Actuators

The multilayer actuator is composed of a number of ceramic layers alternating with internal electrodes. Individual internal electrodes are electrically connected in parallel with two external electrodes attached to the sides. When an electric field is applied to the element, the element expands along the longitudinal direction in accordance with the converse piezoelectric effect. Important features of multilayer ceramic actuators are low driving voltage, quick response, high generative force, and high electromechanical coupling. However, they only exhibit displacements in the range of 10 μm , which may not be sufficient for some applications.

Results from measurements of the direct and converse magnetolectric (ME) effect on a three-layer, epoxy-bonded, laminate composite are presented in Record et al., 2007. The laminae are single transversely polarized piezoelectric elements (PZ29) sandwiched between two longitudinal-magnetically polarized

magnetostrictive TD elements (Terfenol-D-TX GMM). The direct ME effect was determined by measuring laminate output with a Helmholtz-generated AC field (up to 7 Oe) in the range 50 Hz–100 kHz biased by a DC field (0–1000 Oe), Fig.1.5.

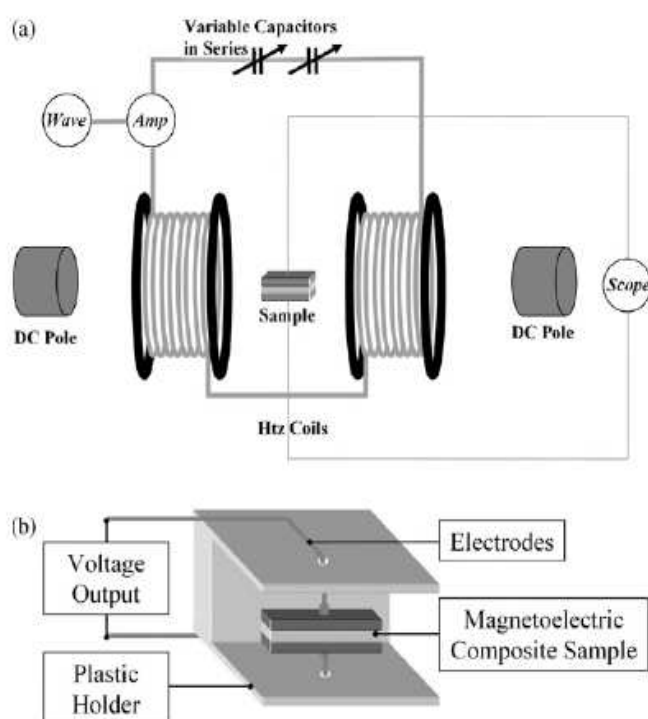


Figure 1.5. (a) Schematic of test facility to measure direct ME response. (b) Sample holder with the suspended composite under test (Record et al., 2007).

Peak voltage output occurred at the mechanical resonant frequency of the sample, its value depending on the strength and direction of the applied magnetic field. The peak output was 3061mV at 3Oe AC field and 1000 Oe bias, equivalent to $74.4\text{Vcm}^{-1}\text{Oe}^{-1}$. The peak output coefficient, however, was $93.6\text{Vcm}^{-1}\text{Oe}^{-1}$ at

0.1 Oe AC field and 1000 Oe DC bias. The reduction at higher drive amplitudes was attributed to increased Young's modulus of the TD phase. Anomalous peaks in the low frequency spectrum of sample output are explained. The converse magnetoelectric effect was measured by recording the voltage induced in a solenoid encompassing the ME while exposed to a DC bias field and the PZ phase driven by a 10VAC source. The peak output is shown to depend on the strength of the applied DC magnetic field and developed a maximum field of 15.4 Oe at the mechanical resonant frequency of the sample. The sample's capability as a micro-power source was demonstrated in a simple device prototype, achieving 110 μ W of DC power. The results from the converse magnetoelectric tests demonstrate that magnetoelectric composite samples could be used in MEMS applications, not only as power source, but also a transducer for half-duplex communication and low magnetic field detection.

The piezoelectricity and polarization of multilayer actuator, being designed to stack ceramic layer and electrode layer alternately, were investigated under a consideration of geometry, the thickness ratio of the ceramic layer to electrode layer by Jeong et al., 2004. The actuators were fabricated by tape-casting of 0.42PbTiO₃-0.38PbZrO₃-0.2Pb(Mn_{1/3}Nb_{2/3})O₃ followed by laminating, burn-out and co-firing process. The actuators of 5 \times 5 mm² in cross section size were formed in a way that 50-200 μ m thick ceramics were stacked 10 times alternately with 5 μ m thick electrode. Increase in polarization and electric field-displacement with increasing thickness ratio of the ceramic/electrode layer and thickness/cross

section ratio were attributed to the change of non-180/180° domain ratio which was affected by the interlayer internal stress and Poisson's ratio of ceramic layer. The piezoelectricity and actuation behaviors were found to depend upon the volume ratio (or thickness ratio) of ceramic layer relative to ceramic layer, see Fig.1.6. Comparing with the experimental results and simple calculation based on the existence of the internal stress, the relationship between field-induced deformation and the geometric structure in the actuator was described.

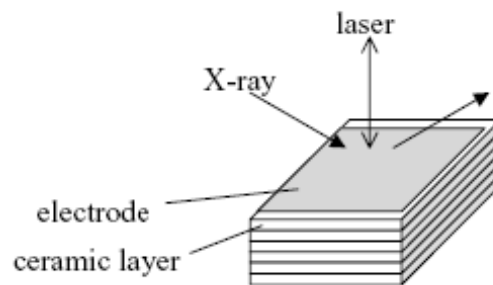


Figure 1.6. Diagram showing ceramic multilayer actuator and its measurement using X-ray diffractory and laser vibrometer (Jeong et al., 2004).

The piezoelectricity and polarization of multilayer actuator, being designed to stack PT–PZ–PMN ceramic layer and Ag–Pd electrode layer alternately, were investigated under a consideration of stacking conditions including the thickness of the ceramic layer, see Fig.1.7. Increase in polarization and electric field-displacement with thickness of the ceramic layer was attributed to the change of non-180 /180° domain ratio. The relative amount of non-180° domain reorientation observed from the XRD diffraction indicates that the internal stress is generated

between the two layers in a manner that the ceramic tends to contract along x_3 axis and to elongate along x_1 axis. In addition, the piezoelectricity and actuation behaviors were found to depend upon the volume ratio (or thickness ratio) of ceramic layer to total layer. The 60 μm -thick ceramic layer actuator showed lower dependence of dielectric polarization and permittivity and piezoelectric coefficient on electric field than those of 120 μm -thick actuator. The change in dielectric and piezoelectric properties may be caused by the retardation of non-180° domain wall motion due to the internal stress generated between the two layers. Such internal stress effect was identified by comparison of the measured dielectric and piezoelectric results with the results calculated by the simple composite model.

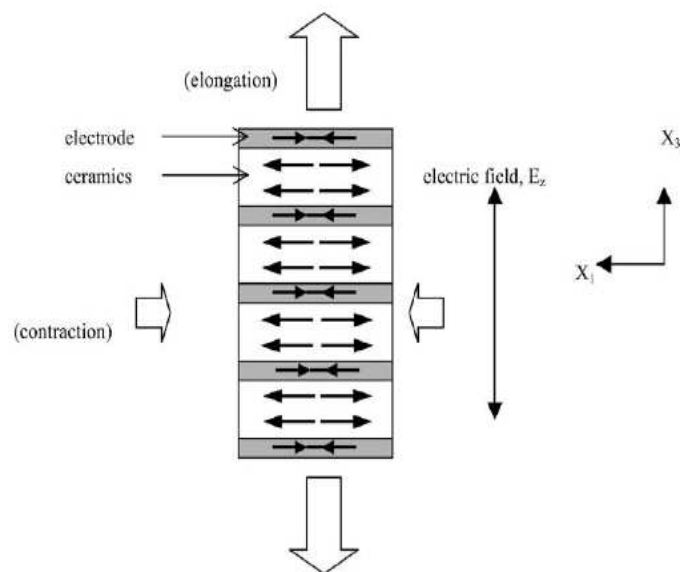


Figure 1.7. Diagram showing the internal stress configuration in the inner structure of multilayer actuator subjected to an electric field along x_3 axis. The electric energy driven by electric field exerts mechanical elongation along x_3 axis and contraction along x_1 axis (Jeong et al., 2004).

Bimorphs usually consist of two thin ceramic sheets bonded together with their poling directions opposed and normal to the interface. When an electric field is applied to a bimorph, one of the plates expands while the other contracts. This mechanism creates a bending displacement. In contrast to the multilayer actuator, bimorphs are capable of generating large bending displacements of several hundred micrometers, but the response time (1ms) and the generative force (1.0 N) are low.

The potential use of piezoelectric bimorph actuators in minimally invasive surgery suture-needle grasper/holder applications is explored computationally by Grujicic et al., 2005, shown in Fig.1.8. Upon defining the design/functional requirements for such surgical tools, a finite element analysis of the underlying piezoelectric boundary value problem is combined with the genetic algorithm optimization routine to arrive at an optimal morphology of the suture-needle grasper/holder.

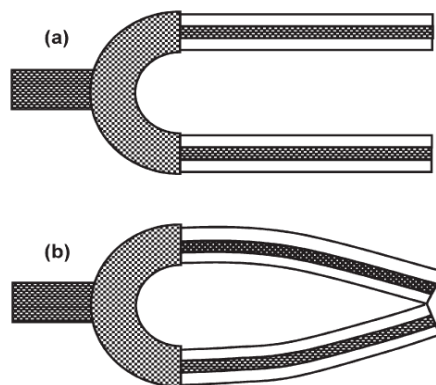


Figure 1.8. A schematic of piezoelectric bimorph grasper in the (a) open and (b) fully-closed positions (Grujicic et al., 2005).

Based on the results obtained in this study, the following main conclusions can be drawn. (1) PZT-based piezoelectric bimorph actuators appear to be suitable for use in the minimally invasive surgery suture-needle grasper/holder applications. (2) To obtain a compromise between a high actuator-tip deflection encountered in actuators with thin piezoelectric layers and a high tip blocked force encountered in the actuators with thick piezoelectric layers, actuators with variable thicknesses of their piezoelectric layers should be used and the thickness variation along the actuator length optimized in order to maximize the grasper performance. (3) The use of the poling direction different from the one standard through-the-thickness direction to increase the grasper performance is found to have only a limited effect. An increase in the grasper width, on the other hand, can significantly increase the grasper-jaws opening to enable an easy grasp of the suture needle.

The electromechanical coupling behavior of a novel, highly coiled piezoelectric strip structure is developed in full, in order to examine its performance and efficiency in the study by Seffen, 2007, Fig.1.9. The strip is doubly coiled for compactness, and compared to a standard straight actuator of the same cross-section; it is shown that the actuator offers better generative forces and energy conversion, and substantial actuated displacements, however, at the expense of a much lower stiffness. The device is therefore proposed for high-displacement, quasi-static applications.

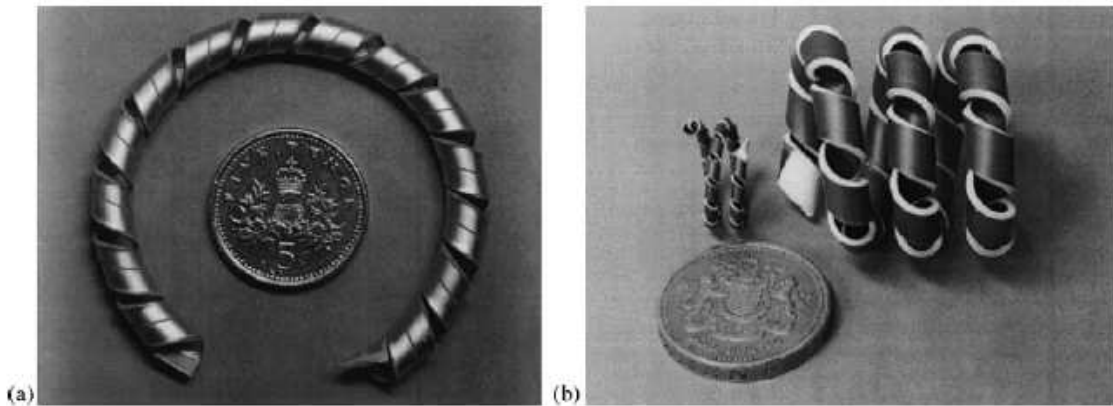


Figure 1.9. Types of super-helix, or “coiled coil” whose size can be compared to British coins: (a) a flat toroidal coiled coil; (b) two coiled coils of different sizes and multiple turns (Seffen, 2007).

From an actuation viewpoint, the localized helical curving of a piezoelectric coiled coil bimorph strip offers two complementary features: the amplification of activated bending strains into substantial axial displacements and the development of a uniform bending moment everywhere along the strip under an axial force for an optimal structural behavior. Compared to a commercially available straight tip-loaded strip, which is not uniformly stressed, the coiled coil generates 33% more blocking force, and is 36% more energetically efficient when the structures are approximately the same size; freely actuated displacements increase tenfold and more.

A piezoelectrically actuated four-bar mechanism with two flexible links is proposed to be used in a micromechanical flying insect robot wing thorax for stroke amplification. PZT-5H and PZN-PT based unimorph actuators are utilized

at the input link of the four-bar for a compact and light weight thorax transmission mechanism by Sitti, 2003. The kinematics and dynamics of the proposed wing structure with two parallel four bar mechanisms are analyzed, Fig.1.10, optimal four-bar link size selection method is introduced, and quasi-static forces generated at the wing are computed for evaluating the feasibility of the design. Using laser micro-machining and folding techniques, prototype four-bar structures are constructed. In the experiments, for a $10 \times 1 \times 0.12 \text{ mm}^3$ PZT-5H actuator based four-bar mechanism, stroke amplification of around 20-25 is held, and an attached polyester wing is resonated at 29 Hz with around 90° flapping motion. These results match closely with the predicted theoretical values.

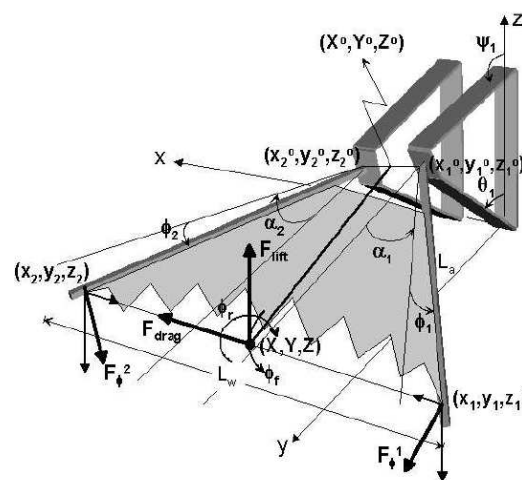


Figure 1.10. Proposed 2 d.o.f. wing mechanism translating and rotating a folded polymer wing using two independently actuated parallel four-bar structures, and its kinematic and force parameters (Sitti, 2003).

PZT-5H and PZN-PT based unimorph actuators are utilized at the input link of the four-bar for a compact design, Fig1.11. The kinematics, dynamics, link size optimization with kinematically singular case considerations, and quasi-static force analysis of the proposed wing structure is realized. Using laser micro-machining and folding techniques, prototype four-bars are constructed, and it is shown that the single four-bar structure can have around 90° stroke motion at 29 Hz with a rigid polyester wing on it. Thus, the proposed design is promising with introduced theoretical models and experimental results. Two degree of freedom flapping and rotating wing mechanism would enable biomimetic flight lift forces where the actuators could supply the desired input forces.

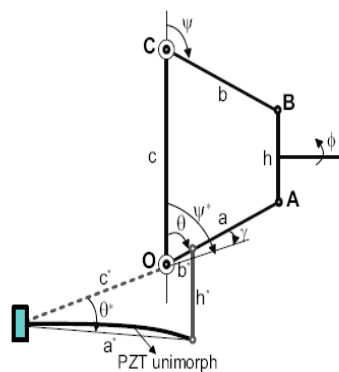


Figure 1.11. Four-bar design proposal for enabling very high stroke amplification if necessary (Sitti, 2003).

1.3.5. Examples of Piezo Sensors

As in most applications of nanotechnology, speed and precision are important requirements for getting good topographical maps of material surfaces using

Scanning Tunneling Microscopes (STM) and Atomic Force Microscopes (AFM). Many STMs and AFMs use piezoelectric tubes for scanning and positioning at nanometer resolution. In the work by Bhikkaji et al., 2007, a piezoelectric tube of the type typically used in STMs and AFMs is considered, see Fig.1.12. Scanning using this piezoelectric tube is hampered by the presence of a low-frequency resonance mode that is easily excited to produce unwanted vibrations. The presence of this low-frequency resonance mode restricts the scanning speed of the piezoelectric tube. Concept of a Positive Velocity and Position Feedback (PVPF) controller is introduced and a controller is designed to damp this undesired resonance mode. To achieve good precision, inputs are then shaped for the closed loop system to track a raster pattern.

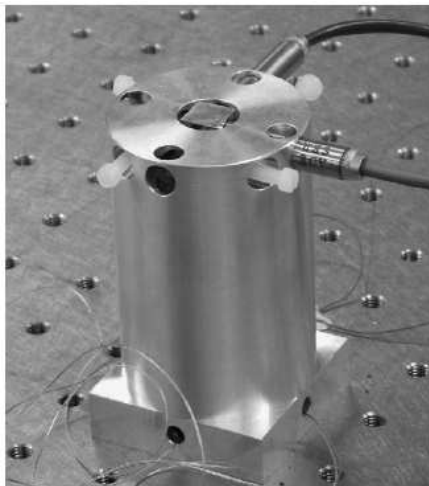


Figure 1.12. The piezoelectric tube mounted inside an aluminum shield. The x-axis capacitive sensor is shown secured at right angles to a cube mounted onto the tube tip. And the y-axis capacitive sensor is secured at right angles to the perpendicular face of the aluminum cube (Bhikkaji et al., 2007).

A piezoelectric tube of the type typically used in STMs and AFMs was considered. This piezoelectric tube was interpreted as a linear system, and a linear model was constructed for it using standard system identification techniques. A lightly damped resonant mode was observed in the linear model in the frequency region of interest. Attempts were made to actuate the piezoelectric tube in a raster pattern in open loop without a feedback controller damping the resonance mode.

In the article by Cima and Remiens, 2005, a new type of sensor involving ferroelectric domain displacements is theoretically and experimentally studied. The principle of such sensors, called ferroelectric active sensors (FAS), is based on the remnant polarization measurement; see Fig.1.13, carried out during a transfer of electric charges caused by polarization switching. As demonstrator, the case of thermal sensors is treated. The active area of the sensor is a PNZT film, realized on silicon substrate. The theoretical performances of the device are evaluated and compared with classical pyroelectric responses. It is finally experimentally shown that this kind of sensor needs to overcome the problem of material fatigue.

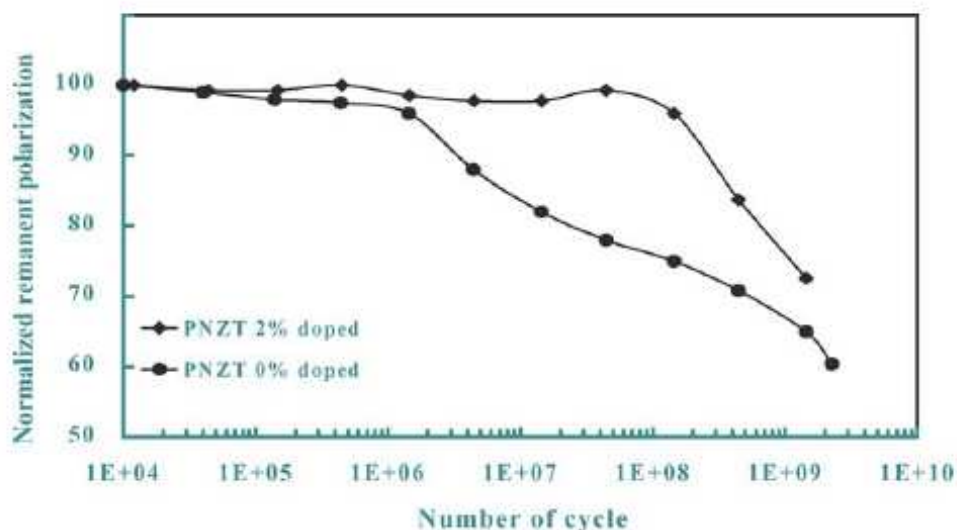


Figure 1.13. Fatigue characteristics of PZT and PNZT (2 at.%) films (Cimaa and Remiens, 2005).

It is shown in this article that the ferroelectric active sensors (FAS) can be applied to thermal measurement. The material figure of merit of FAS is summarized by its pyroelectric coefficient, excluding the material permittivity. It has been concluded that PZT materials, exhibiting a high pyroelectric coefficient, are good candidates for FAS. It can be noticed that FAS can also be employed for mechanical measurement, due to the piezoelectric properties of the ferroelectric capacitor.

Rapid means of characterizing and detecting virus particles are very important for a wide variety of applications. In the study by Johnson et al., 2006, it is used vaccinia virus, a member of the Poxviridae virus family and the basis of the smallpox vaccine, as the test case and characterized these particles using atomic force microscopy and micron-scale cantilever beams, with the long-term goal of

developing devices for the direct rapid detection of air-borne virus particles. The cantilever beams, driven by thermal noise and a PZT piezoelectric ceramic, served as resonating sensors to measure the mass of these virus particles, see Fig.1.14. Two different size cantilevers were used, with dimensions of $21\ \mu\text{m}\times 9\ \mu\text{m}$ and $6\ \mu\text{m}\times 4\ \mu\text{m}$. All cantilevers are measured approximately 200 nm in thickness. The resonant frequency spectra of the cantilevers were measured using a microscope scanning laser Doppler vibrometer before and after the addition of virus particles, and scanning electron micrographs were taken in order to quantify the number of virus particles attached to the cantilevers. The change in resonant frequency as a function of the number of adsorbed virus particles was the basis of the mass detection scheme. The average masses of a single vaccinia virus particle are measured to be $12.4\pm 1.3\ \text{fg}$ and $7.9\pm 4.6\ \text{fg}$, obtained from the larger and smaller cantilever beams, respectively, which are almost in the expected range of 5–10 fg. The measurable mass sensitivity of cantilevers driven by the piezoelectric ceramic is found to be an order of magnitude greater than the sensitivity of cantilevers driven by thermal noise. These cantilever structures can be integral parts of biosensors for the detection of airborne virus particles.

It has been used cantilever beams as micromechanical resonant sensors, augmented by a piezoelectric device, to detect the mass of vaccinia virus particles. Piezo-driven cantilevers were found to have quality factors an order of magnitude greater than thermal-driven cantilevers, allowing for mass detection in the femtogram range.

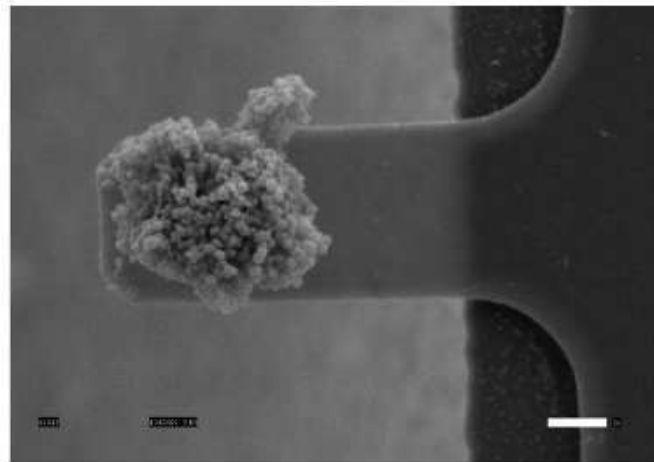


Figure 1.14. Scanning electron micrograph of a large clump of virus particles attached to a cantilever beam, scale bar is 1 μm (Johnson et al., 2006).

In the study by Beeby et al., 2001, authors describe a piezoelectric micro-machined silicon accelerometer fabricated using a combination of thick-film printing and silicon micromachining and introduces a microprocessor implemented self-validation routine for the device, Fig.1.15. The thick-film printed PZT elements act as sensors detecting the deflections of the internal mass and also as actuators capable of performing a self-test routine. The self-validation procedure is performed at resonance and therefore, a microprocessor is used to identify the resonant frequency associated with each device and confirm the operation of the PZT element. Whilst, this approach is certainly feasible, its implementation can be simplified by reducing the cross-talk between drive and detection elements and altering the geometry of the accelerometer. The performance of the device demonstrates the suitability of thick-film printed piezoelectrics for this type of application.

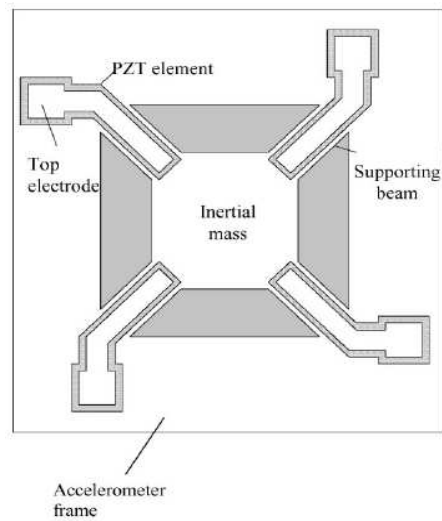


Figure 1.15. Plain view of accelerometer layout (Beeby et al., 2001).

1.4. Energy harvesting by Piezoelectricity

Energy recovery from wasted or unused power has been a research topic for a long time. Power exists in various mechanical forms such as ambient vibrations, water flow, wind, human motion and shock waves. In recent years, industrial and academic researchers have focused their attention on harvesting energy from vibrations using piezoelectricity. These efforts have provided the initial research guidelines and have brought light to the problems and limitations of implementing the piezoelectric transducer. In Chapter 3 of this dissertation another type of waste energy is considered as the power source to be harvested by using the basic principles of piezoelectricity. The waste thermal energy is considered to be the main source of energy that triggers the phase transformation in Shape Memory Alloy. Due to phase transformation the mechanical energy then transferred into electrical energy by direct piezoelectric effect. More details will be discussed in

Chapter 3. In this section of the dissertation, the background on mechanical energy harvesting by piezoelectricity will be discussed.

There are three major phases/steps associated with piezoelectric energy harvesting (see Fig. 1.16): (i) mechanical to mechanical energy transfer, including mechanical stability of the piezoelectric transducer under large stresses, and mechanical impedance matching, (ii) mechanical to electrical energy transduction, relating with the electromechanical coupling factor in the composite transducer structure, and (iii) electrical to electrical energy transfer, including electrical impedance matching. A suitable DC/DC converter is required to accumulate the electrical energy from a high-impedance piezoelectric device into a rechargeable low-impedance battery, [Uchino and Ishii, 2010].

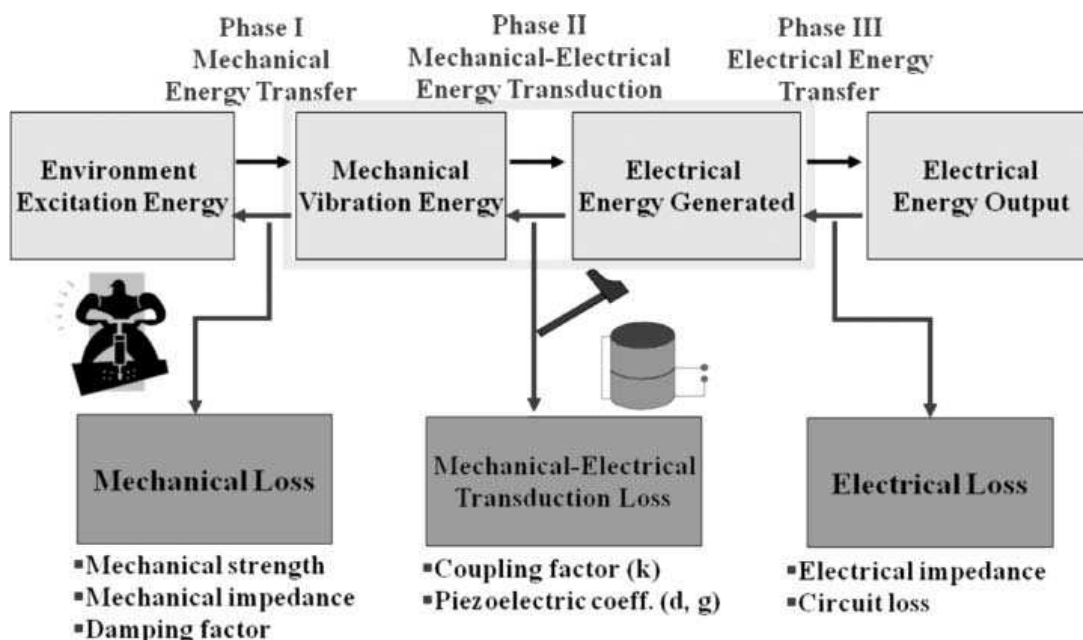


Figure 1.16. Three major phases associated with piezoelectric energy harvesting. [Uchino and Ishii, 2010]

Mechanical impedance matching is one of the important factors in energy conversion in piezoelectric devices. Wasted or unused mechanical energy should be transferred properly to the energy harvester in piezoelectric devices. Mechanical impedance of the material is usually defined by the density and the elastic stiffness of the material. In the energy conversion the receiving part of the mechanical energy in the piezoelectric device is better to be designed to match the mechanical impedance with the mechanical energy source such as vibration source. Mechanical strength and damping factor are also the other important parameters in addition to impedance matching in piezoelectric energy harvesting concept.

Mechanical energy transferred to the piezoelectric transducer is converted into electrical energy through piezoelectric effect. Voltage induced by the piezoelectricity can be explained by the simple piezoelectric equations;

$$V = g \frac{Ft}{A} \quad (1.1)$$

$$g = d/\epsilon_0\epsilon_r \quad (1.2)$$

Here, g , F , t and A are piezoelectric voltage constant, applied force, thickness, and area of the piezoelectric material, respectively. Piezoelectric voltage constant can be written in terms of piezoelectric charge constant, dielectric constant in vacuum and relative dielectric constant as in shown in Eq.(1.2). The output electrical power available from the piezoelectric material can be calculated as,

$$\begin{aligned}
P &= \frac{1}{2} CV^2 \cdot f \\
&= \frac{1}{2} \cdot g_{33} \cdot d_{33} \cdot F^2 \cdot \frac{t}{A} \cdot f
\end{aligned}
\tag{1.3}$$

C and f are the capacitance of the piezoelectric material and the frequency of the mechanical energy source or vibration, respectively. Hence the output power of the energy harvester can be evaluated by the product of piezoelectric voltage constant and piezoelectric charge constant as “Figure of merit” of the energy harvester. Best material for energy harvesting in piezoelectricity can be selected by checking the figure of merit of the material by comparing the piezoelectric voltage and charge constants product of the material.

Piezoelectric materials generally convert mechanical energy to electrical energy with relatively high voltage which means output impedance is relatively high. On the other hand, energy storage devices such as a rechargeable battery have low-input impedance. Thus, large portion of the excited electrical energy is reflected back, if the battery is connected immediately after the rectified voltage. In order to improve energy transfer efficiency, electrical impedance matching is required. Various converters can step down the voltage to adapt the electrical impedance: Forward converter, Buck Converter, Buck-Boost Converter, Flyback Converter etc. These converters have low-output impedance and low-loss characteristics, (Uchino and Ishii, 2010).

1.5. Shape Memory Alloys (SMAs)

Shape memory alloys (SMA) are generally defined as materials with an intrinsic ability to remember their initial crystal structure. This memory shows itself at the macroscopic level mainly in two unusual behaviors, the superelasticity (SE) and the shape memory effect (SME), Auricchio et al., 2001. For the isothermal case, where temperature is constant, and the stress-strain graph of alloy showing superelastic -also called pseudoelastic- behavior is shown in Fig. 1.17. This behavior can be described as undergoing large deformations compared to other conventional engineering materials without any residual strain or deformations. In Figure 1.17, a hysteresis loop can be seen. This hysteresis loop arises upon phase transformation, and heat dissipation observed as a result of this hysteresis. However, as described earlier phenomenon takes place at isothermal case; thus, for this condition to occur, it is assumed that ambient temperature is kept constant and the loading is done slowly, so that the difference between material temperature and the surroundings disappears, and the dissipated heat does not change the temperature of the material.

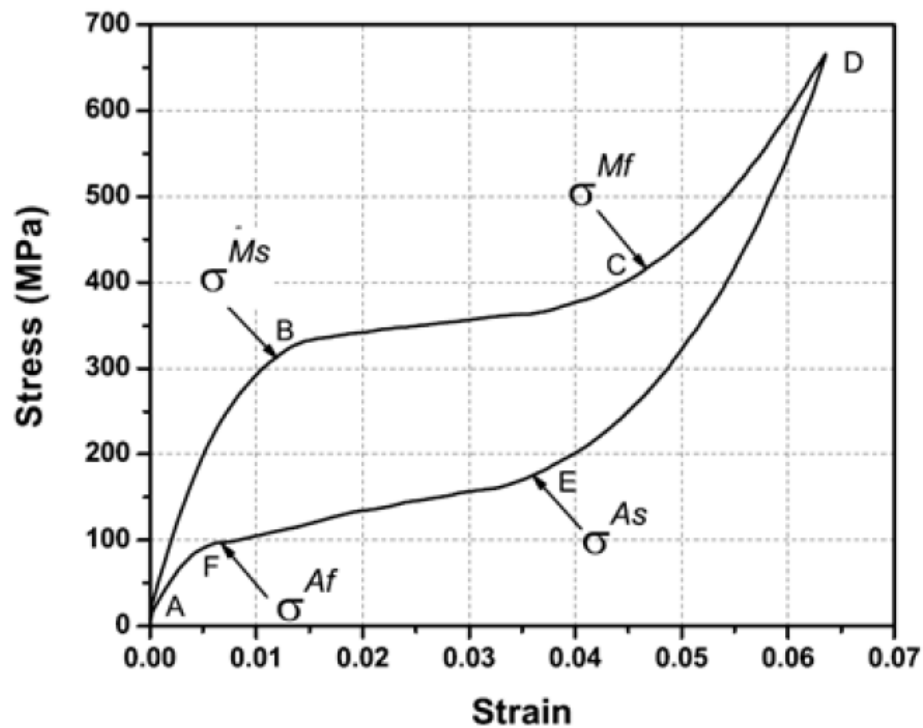


Figure 1.17. Superelastic behavior in SMA (Lagoudas, 2008).

For the non-isothermal case, the behavior of an SMA can be seen on a stress-temperature-strain space in Fig. 1.18. Micromechanical properties of an alloy can change under loading and can even be recovered back to its initial shape by heating. This phenomenon is the main objective of this dissertation, will be discussed in Chapter 3 where the shape recovery stress is used in piezo-SMA composite. When shape memory alloys are plastically deformed at one temperature, they have the ability to completely recover their original shape upon an increase in temperature which is often called as shape-memory effect, Kumar et al., 2003. Superelasticity, on the other hand, indicates the material's ability to

undergo large deformations, up to 10-15% strains, without showing notable permanent deformations, Lagoudas, 2008.

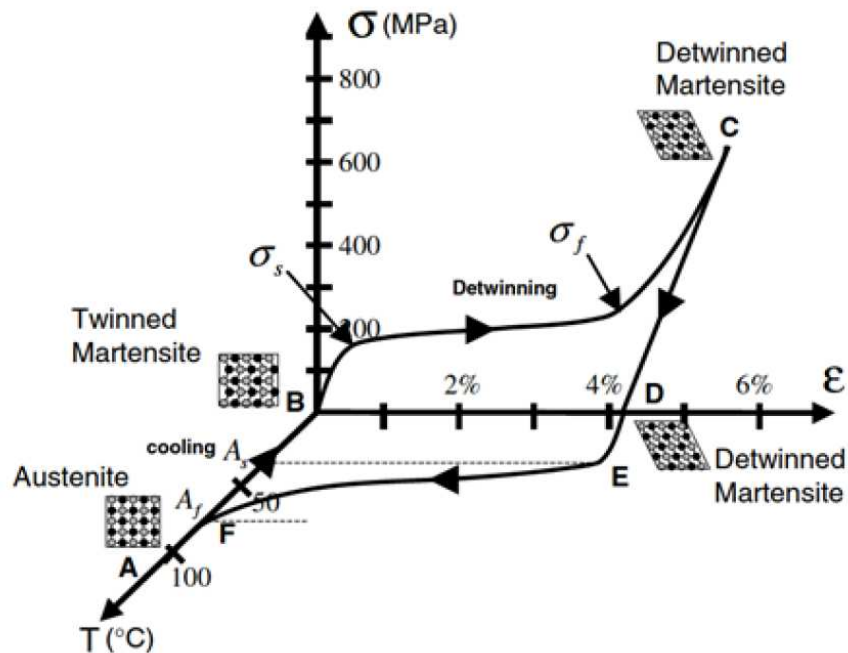


Figure 1.18. Shape Memory Effect in a stress-strain-temperature space and the respective microstructures of a typical NiTi SMA material (Lagoudas, 2008).

SMA has been receiving increasingly more attention and study since the discovery and the first publication of shape memory effect by Chang and Read in 1951 as a constituent in smart composite structures. In 1962 the shape memory phenomenon attracted worldwide attention with the announcement of a shape memory alloy Nickel Titanium (NiTi), Kumar et al., 2003. The inventors W. J. Buehler and R. Wiley named the alloy "NITINOL". The name comes from the chemical symbol "NiTi" followed by "NOL", the acronym for Naval Ordnance Laboratory, the prior designation of the Naval Surface Weapons Center. With the demand for its

properties, the NITINOL technology community prepared a manual, Goldstein, 1980.

Nickel Titanium alloys have properties that are useful in a wide variety of areas. Since recoverable strains of up to 8% can be obtained in NiTi alloys over a relatively narrow temperature range, and since by constraining NiTi alloys stresses of up to 700 MPa can be generated (Otsuka and Wayman, 1999), these two extremes of 8% strain with little or no force generation, and 700 MPa stress, provide a broad envelope to design components with different strain outputs. Although not all of them commercially successful, it is estimated that there are over 10,000 patents based on SMA's. In addition to SME, where strain is recovered upon heating, the SE can also be used in designs, where the material undergoes a transformation cycle with no external temperature change, simply by loading above A_F (Austenite finish temperature). Shape-memory alloys are the basis for innovative applications, ranging from devices used in orthodontia (arch-wires) to self-expanding microstructures for the treatment of organ occlusions (stents) or ranging from coupling devices to micro-actuators, Auricchio et al., 2001.

It is useful to introduce micromechanics for better understanding of superelasticity and shape memory effect. Shape-memory alloys present reversible martensitic phase transformations, that is, solid-solid diffusionless transformations between a crystallographically more-ordered phase, the austenite phase or parent phase, and a

crystallographically less-ordered phase, the martensite phase. Typically, the austenite phase is stable at lower stresses and at higher temperatures, while the martensite phase is stable at higher stresses and at lower temperatures, Auricchio et al., 2001.

The phase transformation (from austenite to martensite or vice versa) is typically marked by four transition temperatures, named as Martensite start, M_S , Martensite finish, M_F , Austenite start, A_S , and Austenite finish, A_F . The ordering between these temperatures under constant stress is as follows; $M_F < M_S < A_S < A_F$ (Rahman, 2008). These four temperatures are given in Fig. 1.19 with the microstructural shapes of austenite and martensite phases as the result of diffusionless transformation. From this figure, it can be seen that a change in temperature within $M_S < T < A_S$ range does not lead to a phase change, and, also, within $M_F < T < A_F$ range, both the martensite and austenite phases may coexist. The phase transformation may take place with temperature, with temperature and loading simultaneously (SME) or with loading only keeping temperature constant (SE).

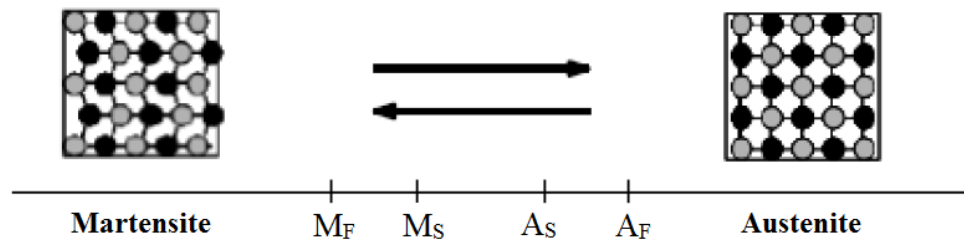


Figure 1.19. Four phase transformation temperatures shown on temperature axis (Simsek, 2009).

Deformation mechanisms and their lattice structures are shown in Fig 1.20. From 1980 up to now, constitutive modeling of shape memory alloys has been a subject of active research. In general, the models developed can be categorized as micro, micro-macro or macro models according to the length-scale of the theory. Micro models describe phenomena occurring at micro-scale level, such as nucleation, interface motion, twin growth, etc (Auricchio et al., 2001). Micro-models, generally, do not take into account martensitic volume and austenitic volume fractions as internal variables, but as consequences of interface motion.

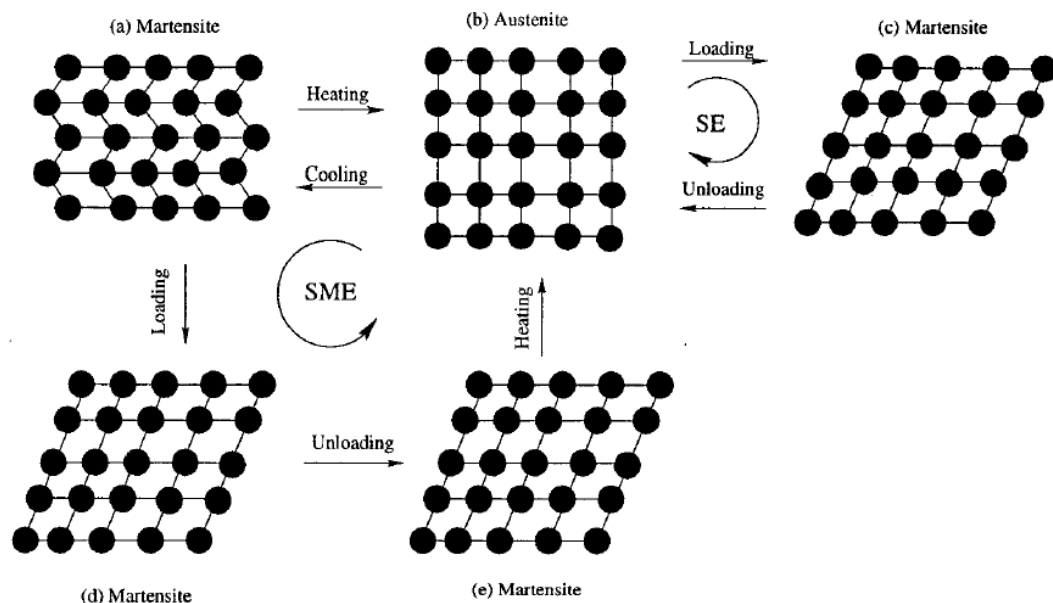


Figure 1.20. Lattice shapes and deformation mechanisms of shape memory alloys under different inputs (Mok, 2003).

Currently, the level achieved in SMA production technologies, together with a deeper knowledge of the micro-scale and macro-scale phenomena, has created the possibility of performing complex experimental investigations, such as combined

tension/torsion or general non-proportional loading tests. As a result, researchers have also moved toward the development of more sophisticated and accurate constitutive models. To name a few models; first of all, Tanaka et al., in 1982 and 1986, studied constitutive behavior of shape memory alloys, using Free Energy concepts and martensite fraction evolution. For the hardening during transformation, an exponential hardening rule is used but material properties (e.g., elastic modulus) are assumed to remain constant during phase transformation, Lagoudas, 2008 and Tanaka et al., 1986. Second, Liang and Rogers, in 1990, proposed another One-Dimensional (1-D) model, using Helmholtz Free Energy concepts, similar to Tanaka et al.'s work, but this time using a cosine hardening rule for the hardening during phase transformation. Later, in 1992, they extended it to a three-dimensional (3-D) model. Lagoudas and Boyd developed another model in 1996. In this model, a potential function is defined using Gibbs Free Energy concept and the variables of the potential function are stress, temperature, and, volumetric martensite fraction. In their paper named "A General Macroscopic Description of the Thermomechanical Behavior of Shape Memory Alloys", Leclercq and Lexcellent proposed a model based on Helmholtz Free Energy and used classical plasticity concepts in explaining the phase transformation surfaces, Leclercq and Lexcellent, 1996. A.C. Souza et al. in 1998 based their model on Generalized Standard Materials approach where internal variables are defined to describe the phase transformation process. They proposed a 3-D phenomenological model of SMAs. In addition to Generalized Standard Materials,

a potential is defined via Helmholtz Free Energy and from this potential 4 constitutive relations are found, giving mean stress, deviatoric stress, transformation stress and, entropy density. Potential function is a function of linear strain, deviatoric strain, transformation strain and, of temperature (notice that since Helmholtz Energy is used, strain is an internal variable in contrast to Lagoudas and Boyd's Gibbs free energy model where stress is an internal variable). Auricchio and Sacco, in their 1997 work on a 1-D model able to simulate the superelastic behavior of shape memory alloys. Martensite fraction is used and evolutionary equations in rate form are proposed for martensite fraction. For the evolution of elastic modulus different methodologies such as Voigt scheme, Reuss scheme, and Mori-Tanaka scheme with elliptical or spherical inclusions are considered. Reuss and Mori-Tanaka schemes are preferred, since experimentally Reuss scheme is realized best experimentally and since Mori-Tanaka scheme represents a feasible upper bound. Extensive work has been done to characterize these materials qualitatively through theoretical models, Tanaka, et al. (1982), Liang et al. (1990), Brinson et al. (1993) and Boyd et al. (1996). Birman (1997) gave a review of work done in the areas of alloy characterization, constitutive modeling, and applications. Compilations of papers have also been published, most recently by Otsuka and Wayman (1998). Elastic behavior of SMA fiber composites has been examined by researchers Liang et al. (1990), Brinson et al. (1993) and Boyd et al. (1996) and Taya et al. (1993).

Chapter 2. Modeling of Piezoelectric - Shape Memory Alloy Composite as a Fast Responsive Actuator Material

A hybrid composite of a piezoelectric ceramic and shape memory alloy (SMA) is proposed as a new actuator material with fast actuation speed and large strain. Analytical modeling of the composite is constructed based on Eshelby's theory where linear piezoelectric constitutive equations and bi-linear super-elastic equations of SMA are used. The predictions of the strain induced by applied stress and electric field are also modeled with two simple designs of piezo-SMA composites, 1-D series and 1-D parallel laminated composites. The predictions based on the proposed model indicate that 1-D parallel laminate provides the highest strain induced under bias stress and applied electric field among other composite geometries examined.

Piezoelectric materials and shape memory alloys (SMAs) are very common materials for actuators and sensors. In the conventional actuator materials, the speed of actuation and sensing is fast, but the order of induced strain is modest while the latter exhibits larger strain, but at much slower speed of actuation. Shape memory alloy (SMA) of super elastic grade has a large strain (up to 5% or so) once it is stressed to the stress level of stress-induced martensite transformation, while piezoelectrics exhibits small-strain (typically less than 1%) with fast actuation speed under applied electric field. If the above two materials are combined to form a composite, which is termed as piezo-SMA composite, one

would expect some unique property to arise. Several researchers Dunn and Taya (1993a; 1993b), Kuo and Huang (1997); Odegard (2004); Qin (2004) predicted that the electromechanical properties of piezoelectric composites consist of piezo matrix and non-piezo filler. The concept of piezo-SMA composite was considered by Jiang and Batra (2002) who formulated the composite model by considering the piezo and SMA phases as filler, which are embedded in isotropic polymer matrix and the Eshelby's method in their analysis. This study, on the other hand, analyzes piezo SMA composite where piezo phase is treated as the matrix and SMA as filler, which can undergo phase-change such as stress-induced martensite transformation as this requires use of Eshelby's method.

In the subsection of Chapter 2, first Eshelby's theory to calculate the effective composite behavior of the piezo-SMA composite will be introduced; later in the following subsections One-dimensional parallel model and One-Dimensional serial model will be summarized, and at the end of the Chapter experimental study carried on to manufacture Piezo-SMA laminate composite will be discussed.

2.1. Modeling Electromechanical Coupling with Eshelby's Theory

The mechanical and electrical behavior of a piezoelectric material can be modeled by two linearized constitutive equations. These equations contain two mechanical and two electrical variables. The direct effect can be modeled by following matrix equations, IEEE Standard on Piezoelectricity, ANSI standard 176-1987.

$$\sigma_{ij} = C_{ijmn} \epsilon_{mn} + e_{nij} (-E_n) \quad (2.1a)$$

$$D_i = e_{imn} \epsilon_{mn} - \kappa_{in} (-E_n) \quad (2.1b)$$

The constitutive equations for a linear piezoelectric material can be represented in matrix notation as, Dunn and Taya (1993a; 1993b), Taya (2005)

$$\Sigma = \mathbf{RZ} \quad (2.2)$$

where Σ represents flux tensor of 9x1, the first six columns of the vector components are the stress components, and the last three are the electric displacements. \mathbf{Z} is the field tensor of 9x1, the first six column of the vector components are elastic strain, and the last three vector components are electric field. \mathbf{R} is the electro-elastic property tensor of 9x9. Flux, field and electro-elastic property tensors can be represented as

$$\Sigma = \begin{bmatrix} \boldsymbol{\sigma}_{6 \times 1} \\ \mathbf{D}_{3 \times 1} \end{bmatrix}, \mathbf{Z} = \begin{bmatrix} \boldsymbol{\epsilon} \\ -\mathbf{E} \end{bmatrix}, \mathbf{R} = \begin{bmatrix} \mathbf{C} & \mathbf{e}^T \\ \mathbf{e} & -\boldsymbol{\kappa} \end{bmatrix} \quad (2.3)$$

respectively, where $\boldsymbol{\sigma}$, \mathbf{D} , \mathbf{C} , \mathbf{e} , $\boldsymbol{\kappa}$, $\boldsymbol{\epsilon}$, and \mathbf{E} denote stress, electrical displacement, elastic moduli, piezoelectric constant, dielectric constant, strain, and electric field matrices, respectively. Piezo phase is assumed to be transversely isotropic piezoelectric material.

Consider an Eshelby's inclusion model for a piezoelectric material: the composite of interest consists of an infinite piezoelectric matrix ($D - \Omega$) containing a finite

volume fraction, f , of spheroidal SMA fillers (Ω), as shown in Fig.2.1(a). The SMA fillers are considered as non-piezoelectric, but exhibit a bi-linear stress-strain curve, that reflects the stress-induced phase transformation. The fillers have electro-elastic modulus \mathbf{R}_f while the matrix has electro-elastic modulus \mathbf{R}_m .

The composite is subjected to the far-field uniform applied stress and electric displacement Σ^o . Fillers in the piezoelectric matrix can be simulated by Eshelby's equivalent inclusions, resulting in Fig.2.1(b) where the electro-elastic stiffness tensor \mathbf{R}_m is homogeneous in the entire domain (D).

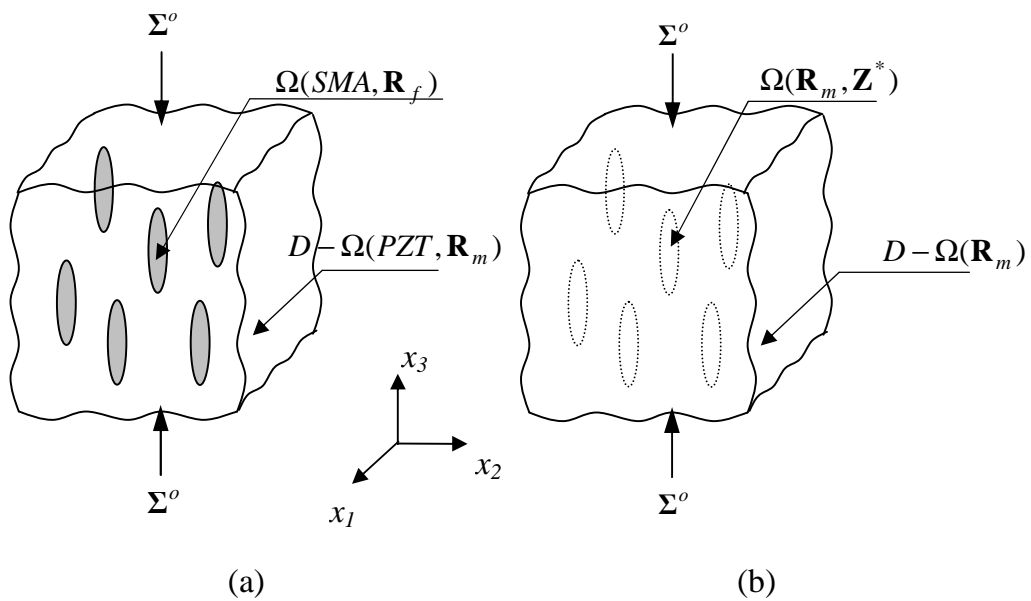


Figure 2.1. Analytical model for piezoelectric composite containing non-piezoelectric SMA fillers, (a) original problem, which is converted to (b) Eshelby's equivalent inclusion problem.

When a piezo-SMA composite is subjected to a far-field uniform flux vector (applied stress and electric displacement) Σ^o , the flux vector (stress and electric displacement) in the filler, Σ_f , can be written as

$$\Sigma_f = \mathbf{R}_f (\mathbf{Z}^o + \bar{\mathbf{Z}} + \mathbf{Z}) = \mathbf{R}_m (\mathbf{Z}^o + \bar{\mathbf{Z}} + \mathbf{Z} - \mathbf{Z}^*) \quad (2.4)$$

where, \mathbf{Z} is the disturbance of the uniform field vector due to the presence of the fillers and $\bar{\mathbf{Z}}$ is the average disturbance of the field vector (strain and electric field) in the matrix. \mathbf{Z}^* is the fictitious eigen field vector (involving eigen strain and eigen electric field) by means of equivalent inclusion method. \mathbf{Z}^o is the uniform field vector (strain and electric field) provided by uniform flux vector, Σ^o that would exist in the absence of the filler and they are related as

$$\Sigma^o = \mathbf{R}_m \mathbf{Z}^o \quad (2.5)$$

The flux vector (stress and electric displacement) in the matrix, Σ_m , can be written as

$$\Sigma_m = \mathbf{R}_m (\mathbf{Z}^o + \bar{\mathbf{Z}}) \quad (2.6)$$

The disturbed field vector (strain and electric field) in the filler, \mathbf{Z} , is related with fictitious eigenfield vector \mathbf{Z}^* through a piezoelectric Eshelby tensor \mathbf{S} as

$$\mathbf{Z} = \mathbf{S} \mathbf{Z}^* \quad (2.7)$$

The flux boundary condition (Σ^o) and the volume integral of the disturbance flux vector (being zero over the entire composite domain) leads to the following relation that relates $\bar{\mathbf{Z}}$ to \mathbf{Z} and \mathbf{Z}^* as

$$\bar{\mathbf{Z}} + f(\mathbf{Z} - \mathbf{Z}^*) = 0 \quad (2.8)$$

where f denotes the volume fraction of the SMA fillers. \mathbf{Z}^* is computed from Eqs.(2.4, 2.5, 2.7 and 2.8) as

$$\mathbf{Z}^* = \mathbf{B}(\mathbf{R}_m - \mathbf{R}_f)\mathbf{Z}^o \quad (2.9)$$

$$\mathbf{B} = \{(\mathbf{R}_f - \mathbf{R}_m)[(1-f)\mathbf{S} + f\mathbf{I}] + \mathbf{R}_m\}^{-1} \quad (2.10)$$

where \mathbf{I} is 9×9 identity matrix and the superscript of “-1” denotes inverse of matrix.

The overall field vector (strain and electric field) of the composite \mathbf{Z}_c is computed by using the weighted volume average (rule of mixture) of that over each phase and given by

$$\mathbf{Z}_c = (1-f)\mathbf{Z}_m + f\mathbf{Z}_f = [\mathbf{I} + f\mathbf{B}(\mathbf{R}_m - \mathbf{R}_f)]\mathbf{Z}^o \quad (2.11)$$

where \mathbf{Z}_m and \mathbf{Z}_f represent total field vectors (strain and electric fields) in the matrix and filler, respectively. The total flux vectors (stress and electric displacement) of each component are expressed as

$$\boldsymbol{\Sigma}_f = [\mathbf{R}_m - (1-f) \cdot \mathbf{R}_m \cdot (\mathbf{S} - \mathbf{I}) \cdot \mathbf{B} \cdot (\mathbf{R}_f - \mathbf{R}_m)] \cdot \mathbf{R}_m^{-1} \cdot \boldsymbol{\Sigma}^o \quad (2.12a)$$

$$\boldsymbol{\Sigma}_m = [\mathbf{R}_m + f \cdot \mathbf{R}_m (\mathbf{S} - \mathbf{I}) \cdot \mathbf{B} \cdot (\mathbf{R}_f - \mathbf{R}_m)] \cdot \mathbf{R}_m^{-1} \cdot \boldsymbol{\Sigma}^o \quad (2.12b)$$

The overall flux vector (stress and electric displacement) of the composite is then given by

$$\boldsymbol{\Sigma}_c = (1-f)\boldsymbol{\Sigma}_m + f \boldsymbol{\Sigma}_f = \boldsymbol{\Sigma}^o \quad (2.13)$$

The effective electro-elastic modulus of the composite \mathbf{R}_c is defined as

$$\boldsymbol{\Sigma}_c = \mathbf{R}_c \mathbf{Z}_c \quad (2.14)$$

From Eqs.(2.5, 2.11, 2.13, and 2.14) the effective electro-elastic modulus of the composite is obtained as

$$\mathbf{R}_c = \mathbf{R}_m [\mathbf{I} + f \mathbf{B} (\mathbf{R}_m - \mathbf{R}_f)]^{-1} \quad (2.15)$$

2.1.1. Mixed Boundary Condition Problem

When a composite is subject to applied stress $\boldsymbol{\sigma}^o$ and an electric field \mathbf{E}^o , where $\boldsymbol{\sigma}^o$ is a part of flux vector and \mathbf{E}^o is a part of field vector, see Eqs.(2.1, 2.2), this lead the problem to have a mixed boundary condition. Mixed boundary condition should be converted to the non-mixed boundary condition in order to apply the Eshelby's equivalent inclusion method discussed in the previous section. This can

be done by using the effective properties of the composite derived in the previous section, Eq.(2.15).

Equation (2.1a) for composite strain can be rewritten in terms of the composite properties as follows,

$$\boldsymbol{\varepsilon}_c = \mathbf{C}_c^{-1} \boldsymbol{\sigma}^o + \mathbf{C}_c^{-1} \mathbf{e}_c^T \mathbf{E}^o \quad (2.16)$$

where the subscript “c” denotes that the variable is a composite property.

The electric displacement generated in the composite by applied mixed boundary condition ($\boldsymbol{\sigma}^o$ and \mathbf{E}^o) can be obtained by substituting Eq.(2.16) in to Eq.(2.1b)

$$\mathbf{D}_c = \mathbf{e}_c \mathbf{C}_c^{-1} \boldsymbol{\sigma}^o + \mathbf{e}_c \mathbf{C}_c^{-1} \mathbf{e}_c^T \mathbf{E}^o + \boldsymbol{\kappa}_c \mathbf{E}^o \quad (2.17)$$

By using the applied stress ($\boldsymbol{\sigma}^o$) and Eq.(2.17), the mixed boundary condition can be converted to the non-mixed boundary condition represented as

$$\boldsymbol{\Sigma}^o = \begin{bmatrix} \boldsymbol{\sigma}_c \\ \mathbf{D}_c \end{bmatrix} = \begin{bmatrix} \boldsymbol{\sigma}^o \\ \mathbf{e}_c \mathbf{C}_c^{-1} \boldsymbol{\sigma}^o + \mathbf{e}_c \mathbf{C}_c^{-1} \mathbf{e}_c^T \mathbf{E}^o + \boldsymbol{\kappa}_c \mathbf{E}^o \end{bmatrix} \quad (2.18)$$

2.1.2. Stress-only Boundary Condition

We shall consider the composite subjected to the applied stress in the absence of electric field, $\boldsymbol{\sigma}^o = \mathbf{U} \cdot \boldsymbol{\sigma}^o$, where \mathbf{U} is defined by

$$\mathbf{U} = [0 \ 0 \ 1 \ 0 \ 0 \ 0]^T \quad (2.19)$$

The magnitude of the stress applied to the composite needs to initiate stress-induced martensite transformation of the SMA fillers σ_{ms} as shown in Fig.2.2. The boundary condition is obtained from Eq.(2.18) and can be written in terms of stress magnitude σ^o as;

$$\boldsymbol{\Sigma}^o = \mathbf{U}_{\Sigma^o} \sigma^o \quad (2.20)$$

where \mathbf{U}_{Σ^o} is 9 x 1 column vector and given by

$$\mathbf{U}_{\Sigma^o} = \begin{bmatrix} \mathbf{U} \\ \mathbf{e}_c \mathbf{C}_c^{-1} \mathbf{U} \end{bmatrix} \quad (2.21)$$

When the composite is subjected to a far-field uniform flux vector (stress and electric displacement), $\boldsymbol{\Sigma}^o$, field vector (the stress and electric displacement) in the filler, $\boldsymbol{\Sigma}_f$, can be computed by Eq.(2.12a) as,

$$\boldsymbol{\Sigma}_f = \mathbf{U}_{\Sigma_f} \sigma^o \quad (2.22)$$

where

$$\mathbf{U}_{\Sigma_f} = \left[\mathbf{R}_m - (1-f) \cdot \mathbf{R}_m (\mathbf{S} - \mathbf{I}) \cdot \mathbf{B} \cdot (\mathbf{R}_f - \mathbf{R}_m) \right] \cdot \mathbf{R}_m^{-1} \cdot \mathbf{U}_{\Sigma^o} \quad (2.23)$$

The stress that initiates martensitic transformation in the fiber phase at the initial state is called *bias stress* and denoted as σ_{ms}^o . The bias stress can be determined by

using Von-Mises effective stress, σ_{eff} , defined in the SMA filler domain that is equal to the martensite start stress, σ_{ms} , Taya and Arsenault, 1989.

$$\sigma_{eff} = \sigma_{ms} = \Sigma_{f,33} - \Sigma_{f,11} \quad (2.24)$$

where subscripts “33” and “11” represent the components of the vector Σ_f , along the SMA phase (x_3 – axis) and its transverse direction, respectively.

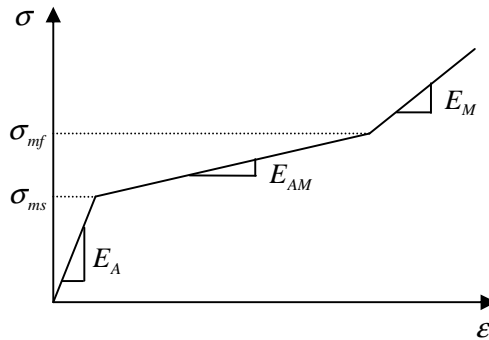


Figure 2.2. Bi-linear stress-strain curve of SMA.

From Eq.(2.22) and (2.24), the bias stress that is required to initiate martensitic transformation can be obtained as

$$\sigma_{ms}^o = \frac{\sigma_{ms}}{U_{\Sigma_f,33} - U_{\Sigma_f,11}} \quad (2.25)$$

where σ_{ms} represents the martensite start stress of the SMA filler, see Fig.2.2.

With stress-only boundary condition, the bias strain in the composite due to the bias stress applied can be computed by Eq. (2.14).

2.1.3. E-Field Boundary Condition

During the phase transformation of SMA filler, from austenite to martensite, the relation between stress and strain of the SMA filler is assumed to be linear between σ_{ms} and σ_{mf} (see Fig.2.2). The applied stress is kept to be constant and its magnitude is computed from Eq.(2.25), while electric field \mathbf{E} is varied. The electric field is then increased such that SMA fillers start to transform from austenite to martensite. When both the stress and electric field are imposed on the composite, the problem can be divided into two subproblems. The first stage is the composite subjected to the applied stress described in the previous subsection (stress only boundary condition). The second stage is the composite subjected to the applied electric field which can be superimposed on the results of the first solution. The analyze of the second stage will be discussed in this section with an arbitrary electric field, $\mathbf{E} = \mathbf{Y} \cdot E^o$, where \mathbf{Y} is defined by

$$\mathbf{Y} = [0 \ 0 \ 1] \quad (2.26)$$

The mixed boundary condition is converted into non-mixed boundary condition by Eq.(2.18)

$$\boldsymbol{\Sigma}^o = \begin{bmatrix} \mathbf{0} \\ \mathbf{e}_c \mathbf{C}_c^{-1} \mathbf{e}_c^T \mathbf{Y} + \boldsymbol{\kappa}_c \mathbf{Y} \end{bmatrix} E^o = \mathbf{Y}_{E^o} E^o \quad (2.27)$$

The flux vector (stress and electric displacement) in the filler domain is computed by Eq.(2.12a), which is rewritten as

$$\Sigma_f = \mathbf{Y}_{\Sigma_f, E^o} E^o \quad (2.28)$$

where

$$\mathbf{Y}_{\Sigma_f, E^o} = [\mathbf{R}_m - (1-f) \cdot \mathbf{R}_m \cdot (\mathbf{S} - \mathbf{I}) \cdot \mathbf{B} \cdot (\mathbf{R}_f - \mathbf{R}_m)] \cdot \mathbf{R}_m^{-1} \cdot \mathbf{Y}_{E^o} \quad (2.29)$$

By using the definition of effective stress and Eq.(2.28), the magnitude of applied electric field (E_{mf}^o) for the fillers to reach the martensite finish (σ_{mf}), is determined as

$$E_{mf}^o = \frac{\sigma_{mf}}{\mathbf{Y}_{\Sigma_f, E^o, 33} - \mathbf{Y}_{\Sigma_f, E^o, 11}} \quad (2.30)$$

After substituting computed E_{mf}^o into Eq.(2.27) the total strain of the composite with SMA fillers fully transformed to martensite is computed under applied electric field, \mathbf{E} only by using Eq.(2.14). Finally, the total strain induced in the composite by both bias stress and electric field is the sum of the strains induced by the results obtained in stress only boundary condition and electric field only boundary condition.

2.2. One-Dimensional Model Based on Parallel Connection

Next, we shall discuss one-dimensional model, i.e. 1-D parallel model as shown in Fig.2.3 where the composite is subjected to applied stress σ^o . The free body

diagram of the composite is shown in Fig.2.4, where each layer is subjected to internal force.

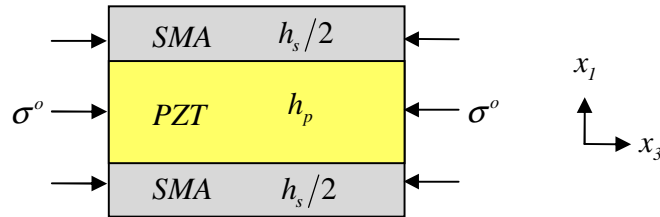


Figure 2.3. Composite with 1-D parallel connection is subjected to applied stress, where h_s and h_p represent the thicknesses of SMA-phase and piezo-phase, respectively.

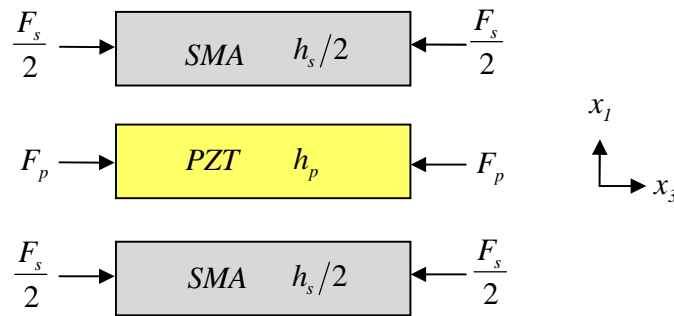


Figure 2.4. Free-body diagram showing forces acting on piezo and SMA layers of 1-D parallel model.

2.2.1. Analysis of a composite under applied stress only

The total force acting on the composite is the sum of forces acting on each phase, from which the applied stress σ^o can be expressed as

$$\sigma^o = \frac{F_s + F_p}{h_s + h_p} \quad (2.31)$$

The strains in each phase are obtained from force, Young's modulus, and thickness, which are given by

$$\varepsilon_s = \frac{\sigma_s}{E_s} = \frac{F_s}{E_s h_s} \quad (2.32a)$$

$$\varepsilon_p = \frac{\sigma_p}{E_p} = \frac{F_p}{E_p h_p} \quad (2.32b)$$

Iso-strain condition of 1-D parallel model ($\varepsilon_s = \varepsilon_p$) gives the relationship between stresses in SMA and PZT phases:

$$\sigma_p = \frac{E_p}{E_s} \sigma_s \quad (2.33)$$

From Eqs.(2.31 and 2.33), the applied stress σ^o can be simply related with the effective stress of SMA filler σ_s as

$$\sigma^o = \sigma_s \frac{fE_s + (1-f)E_p}{E_s} \quad (2.34)$$

The applied stress (σ_{bias}) to start martensite transformation of SMA fibers is obtained from Eq.(2.34) as

$$\sigma_{bias} = \sigma_{ms} \frac{fE_s + (1-f)E_p}{E_s} \quad (2.35)$$

where σ_{ms} is the martensite start stress of SMA. The strain induced in the composite is called bias strain ϵ_{bias} and is given by

$$\epsilon_{bias} = \frac{\sigma_{ms}}{E_s} \quad (2.36)$$

where ϵ_{bias} is the strain corresponding to the applied stress that makes the SMA phase reaching σ_{ms} , see Fig.2.2.

2.2.2. Analysis of a composite under both applied stress and electric field

Next, let's consider the composite additionally subjected to electric field \mathbf{E}^o based on Fig.2.3. With an addition of electric field \mathbf{E}^o so as to induce the compressive strain in the piezo layer, the stress field in the composite is changed as shown in Fig.2.5. The piezo-phase and SMA are in tension and compression, respectively.

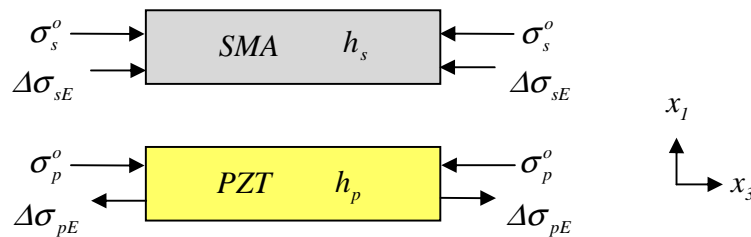


Figure 2.5. Free-body diagram of the composite with applied stress and electric field.

The stress increments in both phases are computed from force equilibrium along the x_3 -axis over the entire composite satisfy

$$h_p \Delta\sigma_{pE} = h_s \Delta\sigma_{sE} \quad (2.37)$$

The total strains in both phases are generated by the applied stress and electric field and are the same:

$$\varepsilon_{bias} + \Delta\varepsilon_{sE} = \varepsilon_{bias} + \Delta\varepsilon_{pE} \quad (2.38)$$

The strains in the SMA and PZT due to the applied electric field are expressed as

$$\Delta\varepsilon_{sE} = \frac{\Delta\sigma_{sE}}{E_{AM}}, \quad \text{and} \quad \Delta\varepsilon_{pE} = -\frac{\Delta\sigma_{pE}}{E_p} + d_{33}E_3, \quad (2.39)$$

where E_{AM} is Young's modulus of SMA during stress-induced phase transformation, see Fig.2.2. Since the bias strains in both phases are the same, the rearrangement of Eq.(2.38) and Eq.(2.39) results in

$$\frac{\Delta\sigma_{sE}}{E_{AM}} = -\frac{\Delta\sigma_{pE}}{E_p} + d_{33}E_3 \quad (2.40)$$

Since the internal stresses in both phases are balanced out, the changes of the stresses in the phases are related with

$$\Delta\sigma_{sE} = \frac{1-f}{f} \Delta\sigma_{pE} \quad (2.41)$$

By inserting Eq.(2.41) into Eq.(2.40), the stress change in the PZT is obtained as

$$\Delta\sigma_{pE} = \frac{fE_{AM}E_p d_{33}E_3}{fE_{AM} + (1-f)E_p} \quad (2.42)$$

The strain induced in the composite by both bias stress and electric field is obtained as

$$\varepsilon_c = \varepsilon_{bias} + \frac{(1-f)E_p d_{33}E_3}{fE_{AM} + (1-f)E_p} \quad (2.43)$$

2.3. One-Dimensional Model Based On Serial Connection

Let's consider a one-dimensional (1-D) model for the composite consisting of layers of PZT and SMA as shown in Fig.2.6, which is subjected to an applied stress σ^o along the x_3 -axis.

Analysis of composite under applied stress only

The initially applied stress σ^o is desired to make SMA phase stress-induced martensite (SIM) phase with starting stress of σ_{ms} , which is already defined as bias stress in the preceding section. The stresses in both PZT and SMA, σ_p and σ_s , are equal due to iso-stress condition inherent in the 1-D series model, which is given by

$$\sigma_p = \sigma_s = \sigma_{ms} \quad (2.44)$$

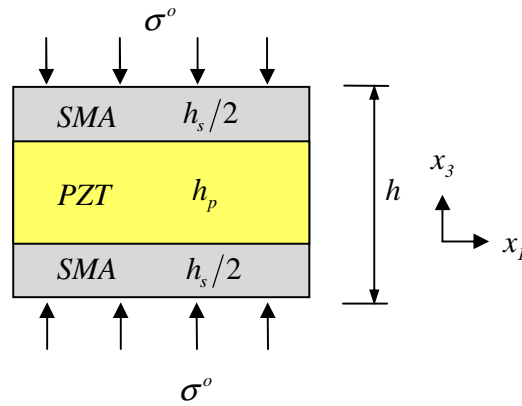


Figure 2.6. Composite with 1-D series connection is subjected to an applied stress, where h_p and h_s represent the thicknesses of PZT and SMA layers, respectively.

The strains in both phases generated by the applied stress can be computed as

$$\varepsilon_p = \frac{1}{E_p} \sigma_{ms} \quad \text{and} \quad \varepsilon_s = \frac{1}{E_A} \sigma_{ms} \quad (2.45)$$

where E_p and E_A denote Young's moduli of PZT and austenitic SMA, respectively. The resultant strain in the composite is called a bias strain and it is obtained as

$$\varepsilon_{bias} = \left(\frac{1-f}{E_p} + \frac{f}{E_A} \right) \sigma_{ms} \quad (2.46)$$

where f denotes the volume fraction of SMA and is equal to h_s/h for this 1-D series model.

Analysis of a composite under both applied stress and electric field

The electric field E^o is additionally applied to the composite under the bias stress σ^o as shown in Fig.2.6. Since the stresses in both phases are maintained as σ_{ms} , the strain in the matrix increases with its electro-mechanical behavior and the strain in the SMA filler does not change. The strains in both phases can be represented as

$$\varepsilon_p = \frac{1}{E_p} \sigma_{ms} + d_{33} E_3 \quad (2.47a)$$

$$\varepsilon_s = \frac{1}{E_A} \sigma_{ms} \quad (2.47b)$$

The strain in the composite induced by both the bias stress and electric field is additive and given by

$$\varepsilon_c = \varepsilon_{bias} + (1-f)d_{33}E_3 \quad (2.48)$$

2.4. The Stiffness Properties of the Piezo-SMA composite

An analytical model to predict the effective stiffness and slope of the stress-strain (SS) curve of a SMA articulate composite which is composed of the particulate SMA phase and piezoelectric matrix phase is constructed. The model is restricted to particulate geometry, and also the role of particulate and matrix can be exchanged. The model is based on Eshelby's theory. A typical SS curve of a composite containing SMA phase is idealized as in Fig.2.7 which consists of three

linear stages, the first stage (100% austenite phase, \mathbf{E}_A^{SMA}), second stage a mixture of austenite and martensite phases (\mathbf{E}_{AM}^{SMA}) and the third stage (100% martensite phase, \mathbf{E}_M^{SMA}). Please note that in the second stage, the fraction of martensite phase increases with an increase in stress, thus this stage is often called “stress-induced-martensite phase transformation (SIM)”. SIM is a key part of superelastic behavior, shown as the loop in Fig.2.7. In the following, details of the model calculations are stated.

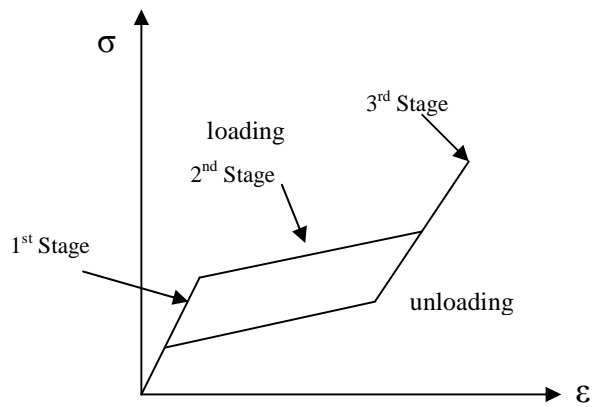


Figure 2.7. Stress-Strain curve of a SMA composite where the first and the third stages are 100% austenite and 100% martensite phase respectively, and the second stage is a mixture of both phases.

1st stage loading curve

For the first stage of the loading curve, the transformation strain $\epsilon_T = \mathbf{0}$. The problem thus reduces to Eshelby’s inhomogeneity problem (Fig. 2.8) where the applied stress causes a relative strain among the matrix and fiber. Using Mori-

Tanaka's Mean Field Theory in association with Eshelby's the stresses in the fiber Ω domain are given by

$$\boldsymbol{\sigma}^0 + \boldsymbol{\sigma} = \mathbf{E}^{SMA} \cdot (\boldsymbol{\varepsilon}^0 + \bar{\boldsymbol{\varepsilon}} + \boldsymbol{\varepsilon}) = \mathbf{E}^{Piezo} \cdot (\boldsymbol{\varepsilon}^0 + \bar{\boldsymbol{\varepsilon}} + \boldsymbol{\varepsilon} - \boldsymbol{\varepsilon}^*) \quad (2.49)$$

Here, $\boldsymbol{\sigma}^0$ is the initial applied stress; $\boldsymbol{\sigma}$ is the change of the stress; $\boldsymbol{\varepsilon}$ is the disturbance strain field; $\bar{\boldsymbol{\varepsilon}}$ is the average strain due to interactions; and \mathbf{E}^{Piezo} is the stiffness tensor of the piezoelectric material.

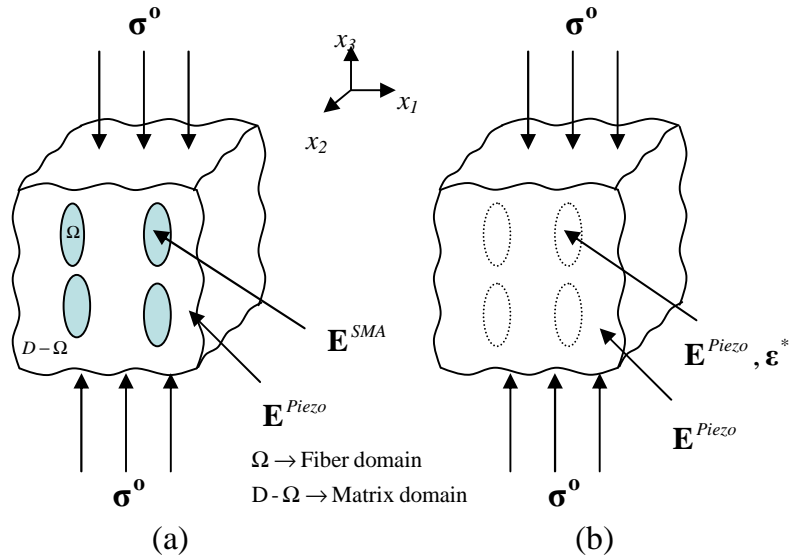


Figure 2.8. (a) Piezo-SMA composite and (b) equivalent Eshelby's inclusion problem for analysis of the first and the third stages in Stress-Strain diagram.

By definition,

$$\boldsymbol{\varepsilon}^0 = (\mathbf{E}^{Piezo})^{-1} \cdot \boldsymbol{\sigma}^0 \quad (2.50)$$

and,

$$\boldsymbol{\sigma} = \mathbf{E}^{Piezo} \cdot (\bar{\boldsymbol{\varepsilon}} + \boldsymbol{\varepsilon} - \boldsymbol{\varepsilon}^*) \quad (2.51)$$

The volume average strain disturbance over the entire domain is zero, thus

$$\bar{\boldsymbol{\varepsilon}} = -f(\boldsymbol{\varepsilon} - \boldsymbol{\varepsilon}^*) \quad (2.52)$$

where f is the SMA volume fraction. Substitute equation (2.52) in (2.49)

$$\mathbf{E}_c = \left[\left(\mathbf{E}^{Piezo} \right)^{-1} + f\mathbf{K} \right]^{-1} \quad (2.53)$$

where

$$\boldsymbol{\varepsilon}^* = \mathbf{K} \cdot \boldsymbol{\sigma}^0$$

$$\mathbf{K} = \left[\left(\mathbf{E}^{SMA} - \mathbf{E}^{Piezo} \right) \cdot \left((1-f)\mathbf{S} + f\mathbf{I} \right) + \mathbf{E}^{Piezo} \right]^{-1} \cdot \left(\mathbf{E}^{Piezo} - \mathbf{E}^{SMA} \right) \cdot \left(\mathbf{E}^{Piezo} \right)^{-1}$$

$$\mathbf{E}^{SMA} \rightarrow \mathbf{E}_A^{SMA} \text{ for stage1 loading and } \mathbf{E}^{SMA} \rightarrow \mathbf{E}_M^{SMA} \text{ for stage3 loading}$$

From equation (2.53) the slope of the compression SS curve of the composite given the input parameters, namely, material properties of constituent phases SMA and Piezo, can be found. But in order to trace the SS curve of the composite, the stress required such that the SMA phase of the composite has a stress value equal to Martensite Start Stress (σ_{Ms}^{SMA}) need to be evaluated. The following set of equations describes the approach to calculate the stress. Applied stress in x_3 -direction can be written with rule of mixtures as

$$\boldsymbol{\sigma}^0 = \mathbf{V}_0 \sigma_{33} = (1-f)\boldsymbol{\sigma}^{Piezo} + f\boldsymbol{\sigma}_{Ms}^{SMA} \quad (2.54)$$

thus the stress in the Piezo will be

$$\begin{aligned} \boldsymbol{\sigma}^{Piezo} &= (\mathbf{I} - f\mathbf{E}^{Piezo} \cdot (\mathbf{S} - \mathbf{I}) \cdot \mathbf{K}_A) \cdot \boldsymbol{\sigma}^0 \\ \Rightarrow \boldsymbol{\sigma}^{Piezo} &= \mathbf{RA} \cdot \boldsymbol{\sigma}^0 \end{aligned} \quad (2.55)$$

where $\mathbf{V}_0 = [0 \ 0 \ 1 \ 0 \ 0 \ 0]^T$, $\mathbf{RA} = (\mathbf{I} - \mathbf{E}^{Piezo} \cdot f(\mathbf{S} - \mathbf{I}) \cdot \mathbf{K}_A)$

and for stage1 loading

$$\mathbf{K}_A = \left[(\mathbf{E}_A^{SMA} - \mathbf{E}^{Piezo}) \cdot \{(1-f)\mathbf{S} + f\mathbf{I}\} + \mathbf{E}^{Piezo} \right]^{-1} \cdot (\mathbf{E}^{Piezo} - \mathbf{E}_A^{SMA}) \cdot (\mathbf{E}^{Piezo})^{-1}$$

use (2.55) in (2.54)

$$(\mathbf{I} - \mathbf{RA})\mathbf{V}_0 \sigma_{33} = f\boldsymbol{\sigma}_{Ms}^{SMA} \quad (2.56)$$

$$\mathbf{RAB} = (\mathbf{I} - \mathbf{RA})\mathbf{V}_0 \quad (2.57)$$

the magnitude of the stress in x_3 direction can be solved as

$$\sigma_{33} = \frac{f\boldsymbol{\sigma}_{Ms}^{SMA}(3,1)}{\mathbf{RAB}(3,1)} \quad (2.58)$$

Thus, applying σ_{33} stress in x_3 direction would produce SIM in the SMA phase of the piezo-SMA composite. Similarly, the total strain in the composite is given by

$$\langle \boldsymbol{\varepsilon} \rangle_{\text{total}} = (1-f)\langle \boldsymbol{\varepsilon} \rangle_{Piezo} + f\langle \boldsymbol{\varepsilon} \rangle_{SMA} \quad (2.59)$$

$$\langle \boldsymbol{\varepsilon} \rangle_{\text{total}} = (1-f)(\boldsymbol{\varepsilon}^o + \bar{\boldsymbol{\varepsilon}}) + f(\boldsymbol{\varepsilon}^o + \bar{\boldsymbol{\varepsilon}} + \boldsymbol{\varepsilon}) \quad (2.60)$$

$$\langle \boldsymbol{\varepsilon} \rangle_{\text{total}} = \boldsymbol{\varepsilon}^o + f\boldsymbol{\varepsilon}^* \quad (2.61)$$

$$\langle \boldsymbol{\varepsilon} \rangle_{\text{total}} = \left[(\mathbf{E}^{\text{Piezo}})^{-1} + f\mathbf{K}_A \right] \cdot \boldsymbol{\sigma}^o = \left[(\mathbf{E}^{\text{Piezo}})^{-1} + f\mathbf{K}_A \right] \cdot \mathbf{V}_o \sigma_{33} \quad (2.62)$$

Thus, the point $(\sigma_{33}, \langle \boldsymbol{\varepsilon} \rangle_{\text{total}}(3,1))$ indicates the first “kink” point of the linear SS curve of the SMA particulate composite.

2nd stage loading curve

In the second stage of loading, an eigenstrain $\boldsymbol{\varepsilon}^T$, phase transformation strain from Austenite to Martensite, exists in the SMA phase. Since the eigenstrain or the non-elastic strain exists only in the fiber phase of the Piezo-SMA composite, the problem is identical to Eshelby’s inhomogeneity inclusion problem (Fig 2.9).

In domain - Ω ,

$$\mathbf{E}_{AM}^{SMA} \cdot (\boldsymbol{\varepsilon}^o + \bar{\boldsymbol{\varepsilon}} + \boldsymbol{\varepsilon} - \boldsymbol{\varepsilon}^T) = \mathbf{E}^{\text{Piezo}} \cdot (\boldsymbol{\varepsilon}^o + \bar{\boldsymbol{\varepsilon}} + \boldsymbol{\varepsilon} - \boldsymbol{\varepsilon}^T - \boldsymbol{\varepsilon}^*) = \mathbf{E}^{\text{Piezo}} \cdot (\boldsymbol{\varepsilon}^o + \bar{\boldsymbol{\varepsilon}} + \boldsymbol{\varepsilon} - \boldsymbol{\varepsilon}^{**}) \quad (2.63)$$

where

$$\boldsymbol{\varepsilon}^{**} = \boldsymbol{\varepsilon}^* + \boldsymbol{\varepsilon}^T$$

$$\boldsymbol{\varepsilon}^T = [-\nu_{SMA} \quad -\nu_{SMA} \quad 1 \quad 0 \quad 0 \quad 0]^T \cdot \boldsymbol{\varepsilon}_{33}^T$$

$$\mathbf{V} = \left[(\mathbf{E}_{AM}^{SMA} - \mathbf{E}^{Piezo}) \cdot \{(1-f)\mathbf{S} + f\mathbf{I}\} + \mathbf{E}^{Piezo} \right]^{-1} \cdot (\mathbf{E}^{Piezo} - \mathbf{E}_{AM}^{SMA}) \cdot (\mathbf{E}^{Piezo})^{-1}$$

$$\mathbf{W} = \left[(\mathbf{E}_{AM}^{SMA} - \mathbf{E}^{Piezo}) \cdot \{(1-f)\mathbf{S} + f\mathbf{I}\} + \mathbf{E}^{Piezo} \right]^{-1} \cdot \mathbf{E}_{AM}^{SMA}$$

$$\boldsymbol{\varepsilon}^{**} = \mathbf{V} \cdot \boldsymbol{\sigma}^0 + \mathbf{W} \cdot \boldsymbol{\varepsilon}^T$$

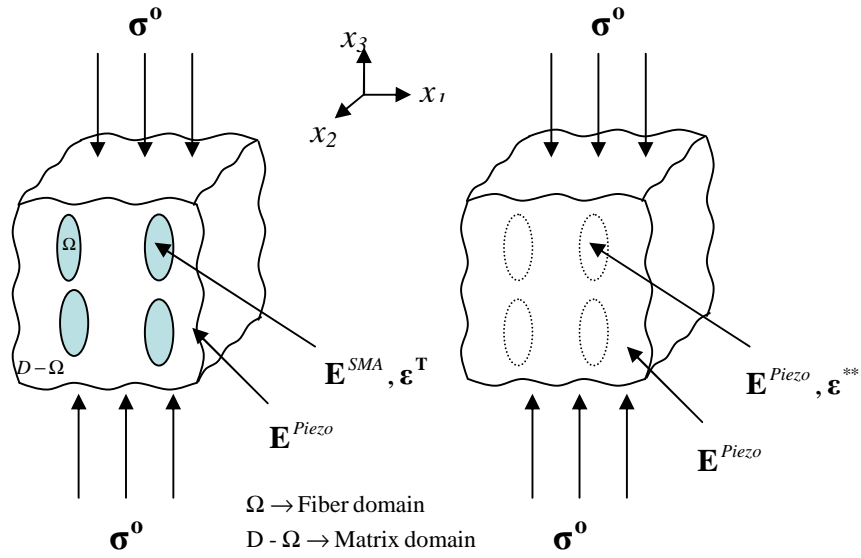


Figure 2.9. Eshelby's inhomogeneity inclusion problem for the simulation of the second stage behavior of Stress-Strain curve of a SMA composite.

Since the Stress-Strain curve of SMA is assumed to be linear, \mathbf{E}_{AM}^{SMA} , the stiffness tensor of SMA phase exhibiting $\boldsymbol{\varepsilon}^T$ eigen strain is written as

$$\mathbf{E}_{AM}^{SMA}(\boldsymbol{\varepsilon}_{33}^T) = \mathbf{E}_A^{SMA} + \frac{(\mathbf{E}_M^{SMA} - \mathbf{E}_A^{SMA})}{\boldsymbol{\varepsilon}_{total}^T} \cdot \boldsymbol{\varepsilon}_{33}^T \quad (2.64)$$

where $\boldsymbol{\varepsilon}_{total}^T$ is the total transformation strain during compression loading of SMA.

The total volume averaged stress in domain-D becomes

$$\langle \boldsymbol{\sigma} \rangle_{\mathbf{D}} = \boldsymbol{\sigma}^0 = (1-f)\mathbf{E}^{Piezo} \cdot (\boldsymbol{\varepsilon}^0 + \bar{\boldsymbol{\varepsilon}}) + f\langle \boldsymbol{\sigma} \rangle_{\mathbf{f}} \quad (2.65)$$

$$\boldsymbol{\sigma}^0 = (1-f)\mathbf{E}^{Piezo} \cdot (\boldsymbol{\varepsilon}^0 - f(\mathbf{S}-\mathbf{I}) \cdot \boldsymbol{\varepsilon}^{**}) + f\langle \boldsymbol{\sigma} \rangle_{\mathbf{f}} \quad (2.66)$$

$$\boldsymbol{\sigma}^0 = (1-f)\boldsymbol{\sigma}^0 - f(1-f)\mathbf{E}^{Piezo} \cdot (\mathbf{S}-\mathbf{I}) \cdot \boldsymbol{\varepsilon}^{**} + f\langle \boldsymbol{\sigma} \rangle_{\mathbf{f}} \quad (2.67)$$

$$\left[\mathbf{I} + (1-f)\mathbf{E}^{Piezo} \cdot (\mathbf{S}-\mathbf{I}) \cdot \mathbf{V} \right] \cdot \boldsymbol{\sigma}^0 + (1-f)\mathbf{E}^{Piezo} \cdot (\mathbf{S}-\mathbf{I}) \cdot \mathbf{W} \cdot \boldsymbol{\varepsilon}^T = \langle \boldsymbol{\sigma} \rangle_{\mathbf{f}} \quad (2.68)$$

or

$$\left[\mathbf{I} + (1-f)\mathbf{E}^{Piezo} \cdot (\mathbf{S}-\mathbf{I}) \cdot \mathbf{V} \right] \cdot \begin{bmatrix} 0 \\ 0 \\ 1 \\ 0 \\ 0 \\ 0 \end{bmatrix} \sigma_{33} + (1-f)\mathbf{E}^{Piezo} \cdot (\mathbf{S}-\mathbf{I}) \cdot \mathbf{W} \cdot \begin{bmatrix} -V_{SMA} \\ -V_{SMA} \\ 1 \\ 0 \\ 0 \\ 0 \end{bmatrix} \boldsymbol{\varepsilon}_{33}^T = \langle \boldsymbol{\sigma} \rangle_{\mathbf{f}}$$

this can be simplified as

$$R(6,1)\sigma_{33} + T(6,1)\boldsymbol{\varepsilon}_{33}^T = \langle \boldsymbol{\sigma} \rangle_{\mathbf{f}} \quad (2.69)$$

$$R(3,1)\sigma_{33} + T(3,1)\boldsymbol{\varepsilon}_{33}^T = \langle \sigma_{33} \rangle_{\mathbf{f}} \Rightarrow \sigma_{33} = \frac{\langle \sigma_{33} \rangle_{\mathbf{f}} - T(3,1)\boldsymbol{\varepsilon}_{33}^T}{R(3,1)} \quad (2.70)$$

where

$$\mathbf{R} = [\mathbf{I} + (1-f)\mathbf{E}^{Piezo} \cdot (\mathbf{S} - \mathbf{I}) \cdot \mathbf{V}] \cdot \begin{bmatrix} 0 \\ 0 \\ 1 \\ 0 \\ 0 \\ 0 \end{bmatrix} \text{ and } \mathbf{T} = (1-f)\mathbf{E}^{Piezo} \cdot (\mathbf{S} - \mathbf{I}) \cdot \mathbf{W} \cdot \begin{bmatrix} -\nu_{SMA} \\ -\nu_{SMA} \\ 1 \\ 0 \\ 0 \\ 0 \end{bmatrix}$$

The volume averaged strain is computed as

$$\begin{aligned} \langle \boldsymbol{\varepsilon} \rangle_{\mathbf{D}} &= (1-f)(\boldsymbol{\varepsilon}^o + \bar{\boldsymbol{\varepsilon}}) + f(\boldsymbol{\varepsilon}^o + \bar{\boldsymbol{\varepsilon}} + \boldsymbol{\varepsilon} - \boldsymbol{\varepsilon}^T) = \boldsymbol{\varepsilon}^o + f(\boldsymbol{\varepsilon}^{**} - \boldsymbol{\varepsilon}^T) \\ &= \left((\mathbf{E}^{Piezo})^{-1} + f\mathbf{V} \right) \cdot \boldsymbol{\sigma}^o + f(\mathbf{W} - \mathbf{I}) \cdot \boldsymbol{\varepsilon}^T \end{aligned} \quad (2.71)$$

where

$$\boldsymbol{\sigma}^o = \begin{bmatrix} 0 \\ 0 \\ 1 \\ 0 \\ 0 \\ 0 \end{bmatrix} \sigma_{33}, \boldsymbol{\varepsilon}^T = \begin{bmatrix} -\nu_{SMA} \\ -\nu_{SMA} \\ 1 \\ 0 \\ 0 \\ 0 \end{bmatrix} \boldsymbol{\varepsilon}_{33}^T$$

Thus, the applied stress σ_{33} required to cause any given $\boldsymbol{\varepsilon}_{33}^T$ transformation strain can be calculated using equation (2.64). Consequently, the total strain exhibited by the composite for the applied stress can be evaluated using (2.68). Plotting σ_{33} versus $\langle \boldsymbol{\varepsilon} \rangle_{\mathbf{D}}$ (3,1) values obtained by varying $\boldsymbol{\varepsilon}_{33}^T$ between $(0, \boldsymbol{\varepsilon}_{total}^T)$ gives us the SS curve for the piezo-SMA. It is to be noted that equation (2.64) makes use of iterative method which uses ‘older’ $\boldsymbol{\varepsilon}_{33}^T$ to compute $\mathbf{E}_{AM}^{SMA}(\boldsymbol{\varepsilon}_{33}^T)$. An iterative process

for the calculation of σ_{33} has been proposed here. ε_{33}^T is varied between $(0, \varepsilon_{total}^T)$ and at each n^{th} step, $\mathbf{E}_{AM}^{SMA}(\varepsilon_{33}^T)$ is calculated using $\varepsilon_{33}^T (n-1)^{\text{th}}$. By increasing the number of steps, the error can be minimized.

3rd stage loading curve

Third stage loading curve is similar to the 1st stage in the sense that there does not exist any transformation strain in the SMA phase. Thus, the problem can be solved as Eshelby's inhomogeneity (Figure 2.8). The first step involves calculation of martensite finish stress for the SMA phase.

$$\boldsymbol{\sigma}^0 = \sigma_{33} \mathbf{V}_o = (1-f)\boldsymbol{\sigma}^{Piezo} + f\boldsymbol{\sigma}_{MF}^{SMA} \quad (2.72)$$

$$\boldsymbol{\sigma}^{Piezo} = (\mathbf{I} - \mathbf{E}^{Piezo} \cdot f(\mathbf{S} - \mathbf{I}) \cdot \mathbf{K}_M) \cdot \boldsymbol{\sigma}^0 \Rightarrow \boldsymbol{\sigma}^{Piezo} = \mathbf{RM} \cdot \boldsymbol{\sigma}^0 \quad (2.73)$$

where $\mathbf{V}_o = [001000]^T$, $\mathbf{RM} = (\mathbf{I} - \mathbf{E}^{Piezo} \cdot f(\mathbf{S} - \mathbf{I}) \cdot \mathbf{K}_M)$ and for stage3 loading

$$\mathbf{K}_M = \left[(\mathbf{E}_M^{SMA} - \mathbf{E}^{Piezo}) \cdot \{(1-f)\mathbf{S} + f\mathbf{I}\} + \mathbf{E}^{Piezo} \right]^{-1} \cdot (\mathbf{E}^{Piezo} - \mathbf{E}_M^{SMA}) \cdot (\mathbf{E}^{Piezo})^{-1}$$

use (2.73) in (2.72)

$$(\mathbf{I} - \mathbf{RM})\mathbf{V}_o \sigma_{33} = f\boldsymbol{\sigma}_{MF}^{SMA} \quad (2.74)$$

define

$$\mathbf{RMB} = (\mathbf{I} - \mathbf{RM})\mathbf{V}_o \quad (2.75)$$

the magnitude of the stress can be solved as

$$\sigma_{33} = \frac{f\sigma_{\text{Mf}}^{\text{SMA}}(3,1)}{\text{RMB}(3,1)} \quad (2.76)$$

Thus, applying σ_{33} stress in x_3 -direction would produce $\sigma_{\text{Mf}}^{\text{SMA}}(3,1)$ in SMA phase of the piezo-SMA composite. The total strain in the composite is given by

$$\langle \boldsymbol{\varepsilon} \rangle_{\text{total}} = (1-f)\langle \boldsymbol{\varepsilon} \rangle_{\text{Piezo}} + f\langle \boldsymbol{\varepsilon} \rangle_{\text{SMA}} \quad (2.77)$$

$$\langle \boldsymbol{\varepsilon} \rangle_{\text{total}} = (1-f)(\boldsymbol{\varepsilon}^0 + \bar{\boldsymbol{\varepsilon}}) + f(\boldsymbol{\varepsilon}^0 + \bar{\boldsymbol{\varepsilon}} + \boldsymbol{\varepsilon}) \quad (2.78)$$

$$\langle \boldsymbol{\varepsilon} \rangle_{\text{total}} = \boldsymbol{\varepsilon}^0 + f\boldsymbol{\varepsilon}^* \quad (2.79)$$

$$\langle \boldsymbol{\varepsilon} \rangle_{\text{total}} = \left[(\mathbf{E}^{\text{Piezo}})^{-1} + f\mathbf{K}_{\text{M}} \right] \cdot \boldsymbol{\sigma}^0 = \left[(\mathbf{E}^{\text{Piezo}})^{-1} + f\mathbf{K}_{\text{M}} \right] \cdot \mathbf{V}_0 \sigma_{33} \quad (2.80)$$

Thus, the point $(\sigma_{33}, \langle \boldsymbol{\varepsilon} \rangle_{\text{total}}(3,1))$ indicates the second “kink” point of the assumed linear Stress-Strain curve of the SMA particulate composite.

2.5. The Experimental Study to Fabricate the Piezo-SMA Laminated Composite

Spark Plasma Sintering (SPS) process is used in order to form mechanical bonding between piezo and SMA which will form laminated composite material discussed in modeling part for the actuator, see Fig.2.10. Dr. Sinter Model SPS-1020 Spark Plasma Sintering System from Sumitomo Coal Mining Co. Ltd. which is designed

for a wide range of experimental research on new materials is used in SPS process. The Dr. Sinter allows sintering inorganic materials including ferrous and non-ferrous metals.

Spark plasma sintering process first compresses the starting powder material, and then applies ON/OFF pulse controlled power using the originally developed sintering DC pulse generator to concentrate high density energy positively in the area of neck formation between particles in order to provide compacts with high dimensional accuracy and uniformity.

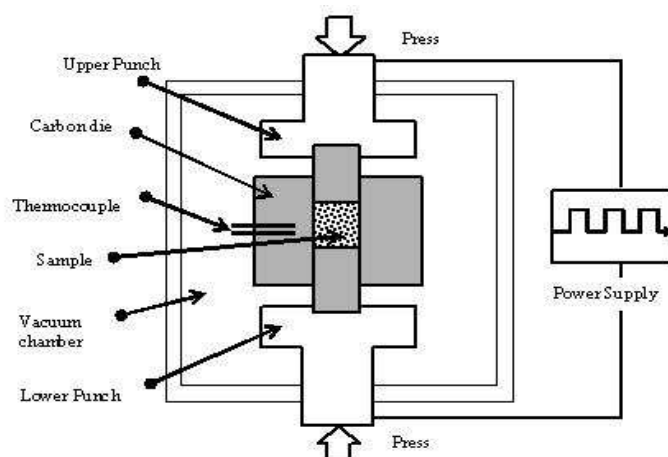
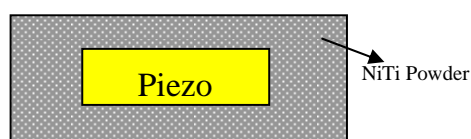


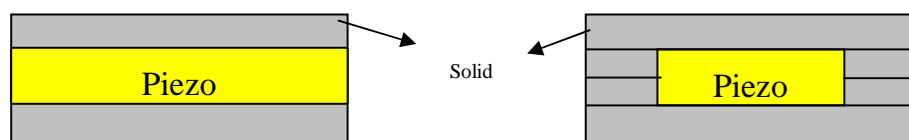
Figure 2.10. Schematic view of Spark Plasma Sintering (SPS) machine.

The SPS system fabricates high-grade sintered compacts at a lower temperature and in shorter time than conventional sintering methods. Amorphous materials can be sintered at below the normal temperature of crystallization. With this process one can control the microstructure of the material and crystal growth. The original

properties of the material are maintained. Sintering can be carried out under atmospheric conditions, with inert gases, or even in a vacuum. The system operates over a wide temperature range up to maximum 1700 °C. Dr. Sinter has optimal functions to aid in development of a broad spectrum of new materials; nano phase materials, tungsten carbides, magnetic materials, titanium alloys, amorphous materials, electronics materials, functional materials, composites and also fine ceramics. The system can also be used to manufacture highly porous materials.



(a) Powder SMA and Piezo Disc



(b) SMA plate and Piezo Disc

(c) SMA plate, SMA ring and Piezo Disc

Figure 2.11. Schematic view for preparing the specimen for SPS process

It is attempted to fabricate piezo-SMA laminated composite first using powders of piezo and SMA (NiTi), Fig.2.11(a). However, piezo powders (PMN) were in non-oxidization condition during high temperature and vacuum SPS process, which causes piezoelectric material to lose its piezoelectric properties. In order to recover

the piezo properties, oxidation process needs to be carried on following SPS process. In other words, heat treatment in an oxidation environment needs to be done to recover the piezoelectric properties which had been destroyed while heating over the Curie temperature. Post heat treatment is carried on in oxidation environment. This causes the composite to have poor piezoelectric properties.

Another approach to fabricate piezo-SMA laminate composite is proposed by using piezo-plate(disc shape) and NiTi plates laminated together, then subjecting the laminate to SPS process, shown Fig.2.11(b). The advantage of this method is to keep the original properties of both piezo (PZT) and SMA (NiTi) plates, while the disadvantage is difficulty of making a strong bonding between piezo plate and NiTi plates. This method resulted in often cracking of PZT material presumably was caused during high pressure of SPS process, and brittle nature of PZT material itself.

Third method, shown in Fig.2.11(c), is carried on with two SMA rings are introduced in the middle layer that helps to keep PZT piezo disc inplace. The number of rings are depends on the thickness of the Piezoelectric material, and the SMA plate thickness itself. In addition, NiTi powders (SMA material that is used in this method) are put in the interface between NiTi plates and piezoelectric disc to enhance the bonding during SPS process. Upon SPS process, the piezo-SMA laminate composite is dissected by diamond saw, shown in Fig.2.12. The cross-section appears to be good in shape without cracking.



Figure 2.12. Cross section of PZT-NiTi laminated composite.

All cases of methods, (a), (b) and (c) applied in fabricating piezo-SMA laminate, are summarized in Table 2.1, where the acceptable piezo-SMA composite process is named as Case 8. The cross section of Case 8 is shown in Fig.2.12. SPS process is carried on with low range pressure option of the SPS machine, starting with Case 6. Pressure control of SPS machine has two selections, in high range the loading can be varied from 5kN to 100kN, where in low range it can be controlled from nearly 1kN to 5kN.

Table 2.1. Summary of SPS processing on piezo-SMA laminates.

Case	Pressure (MPa)	Heating rate (°C/min), Peak Temp (°C)	Piezo (dia, thickness) mm	NiTi disc, (dia, thickness) mm	Setup (Fig.2.11)	Results
1	1.60	100, 800	PMN (20, 1.05)	Powder (fine)	a	PMN color is OK. Several axial cracks. Low porosity, due to fine powder.
2	12	100, 800	PZT (10, 2.05)	(10, 1)	b	PZT is damaged. Pressure is high.
3	3.6	100, 800	PMN (20, 1.05)	(20,1)	b	PMN is damaged; one surface seems to be bounded well, while the other is not. PMN gets black in color.
4	7.96	100, 800	PZT (10, 2.05)	(30, 1)	c	PZT is damaged. Rings are not bounded; also PZT is not bounded to NiTi. Surface polishing should be better.
5	4.6	100, 800	PZT (10, 2.05)	(30, 1)	c	Total thickness of the rings is equal to the PZT thickness. PZT is damaged. Bonding is OK, between PZT and NiTi.
6	0.80	100, 800	PMN (20, 1.05)	Powder, fine around the PMN and SMA contact surfaces; 300µm in the top and bottom of the die.	a	Low range pressure is used for the first time. Only a tiny crack observed in thickness direction. High porosity due to thick powder.

7	1.11	100, 700	PMN (20, 1.05)	(20,1)	b	<p>PMN is damaged on purpose before SPS in order to figure out difference in color through the cracks. After the experiment, it is observed that, some axial and radial cracks; color is black so the difference can't be observed. One side is bounded well while the other not.</p>
8	1.11	100, 700	PZT (10, 2.05)	(30, 1)	c	<p>Low range loading, PZT with 2.05 mm thickness is used. Fine powder is applied in the gaps between the PZT and discs due to the thickness difference in PZT and rings. Also fine powder is applied between NiTi contact layers.</p> <p>Color is OK. No cracks.</p> <p>Bounding seems OK, but should be examined further</p>

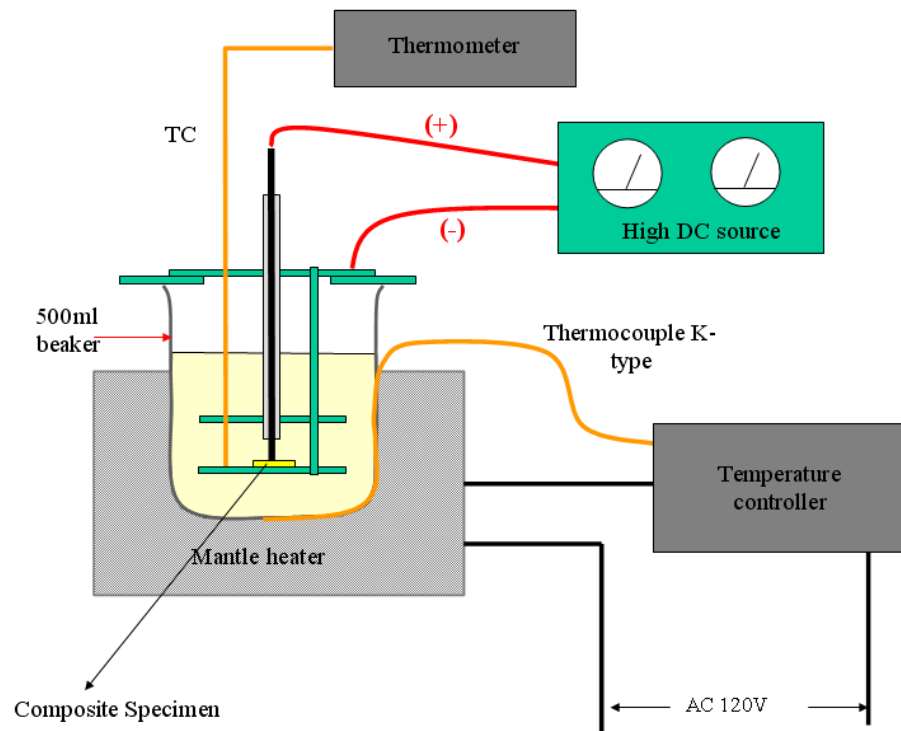


Figure 2.13. Poling setup for Piezo-SMA laminated composite.

Since, PZT material loses its piezoelectric properties at the temperatures higher than the Curie temperature. The material is poled by applying a high voltage (1-1.5kV/mm) at a temperature of 150°C to gain its piezoelectric properties. Poling setup used for the poling purpose, shown as in Fig.2.13.

2.6. Results and Discussion

In this section of the study, the modeled composites are assumed to be composed of SMA (CuMnAl) fillers and piezo (PZT) matrix, whose properties are given in Table 2.2 (Takagi et al., 2002). The data marked by * are not available from the literature and assumed with comparing the materials listed in other literature mentioning the same materials. One-dimensional parallel and three-dimensional

with Eshelby's theory are employed with the material properties given. The fillers for Eshelby model are assumed to be continuous SMA fiber where the aspect ratio of prolate ellipsoidal inclusion is set to infinity. Mixed boundary condition is converted into non-mixed boundary condition by using electromechanical coupling behavior of piezoelectric material. Strain in the composite with respect to applied electric field is predicted with two models.

Table 2.2. Property data of piezo and SMA phases.

	C [GPa]					e [C/m ²]			κ	
	C_{11}	C_{12}	C_{13}	C_{33}	C_{44}	e_{31}	e_{33}	e_{15}	κ_{11}/κ_0^*	κ_{33}/κ_0
PZT	146	95.4	94.3	128	25.3	-3.94	17.5	12.3	916	1654
SMA	$E_A = 29.5$, $E_{AM} = 1.78$, $E_M = 5.75$, $\nu = 0.3$ $\sigma_{ms} = 117\text{MPa}$, $\sigma_{mf} = 217\text{MPa}$									

* $\kappa_0 = 8.85 \times 10^{-12} [\text{C}^2 / \text{Nm}^2]$ = permittivity of free space

Total strain in the composite with respect to applied electric field is predicted with using 1-D parallel model, serial model and 3-D model with Eshelby theory. Figure 2.14 shows the predicted results for the total strain with applied electric field. All strain response starts with a bias strain due to applied bias stress which was defined as; the stress to be applied to the composite in order to have SMA to reach martensite starting condition. This stress value is defined as Martensite starting stress in bilinear stress strain curve of SMA. Piezo only case is also plotted in the same graph; one can easily see that this case there is no bias stress applied therefore initial strain is zero for Piezo only case. The volume fraction of SMA filler is 0.5 for all except piezo-only case.

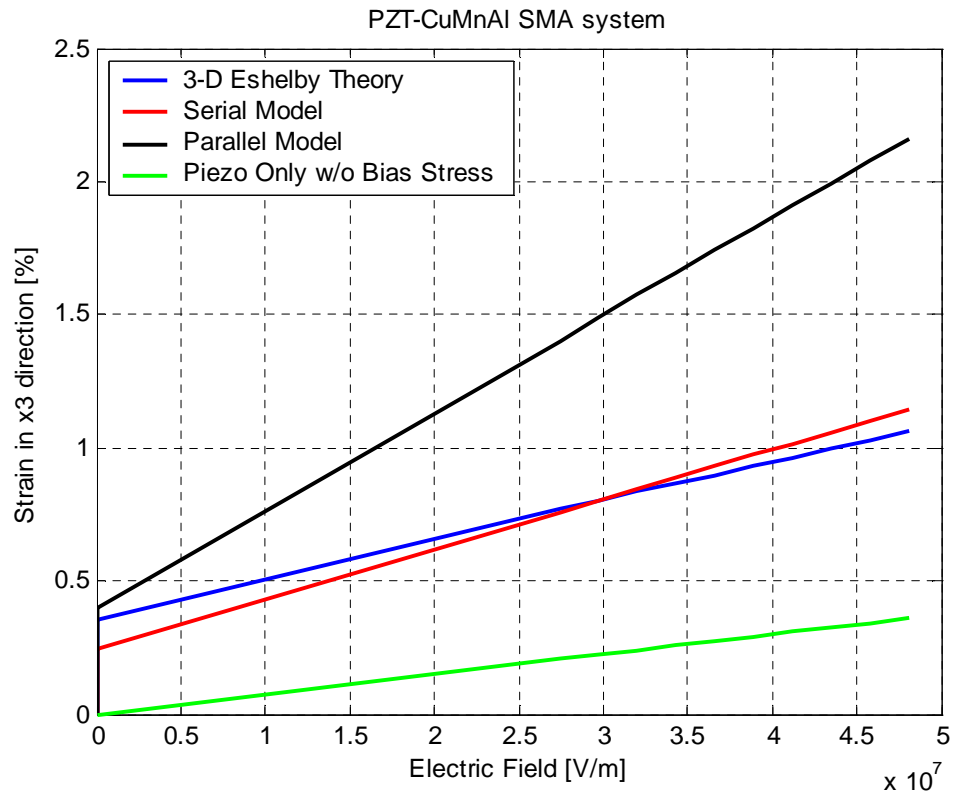


Figure 2.14. Total strain of the piezo-SMA composite with applied electric field.

The Stress-Strain response with different volume fractions of SMA phase is also examined by using 3-D model with Eshelby Theory. Figure 2.15a shows the case when the SMA volume fraction is 0.5. The graph consists of two regions; in first the stress in the composite is linearly increasing, in the second region while composite stress is constant the strain is increasing due to applied electrical field to the composite. These boundary conditions were discussed in Section 2.1.2 and 2.1.3, respectively.

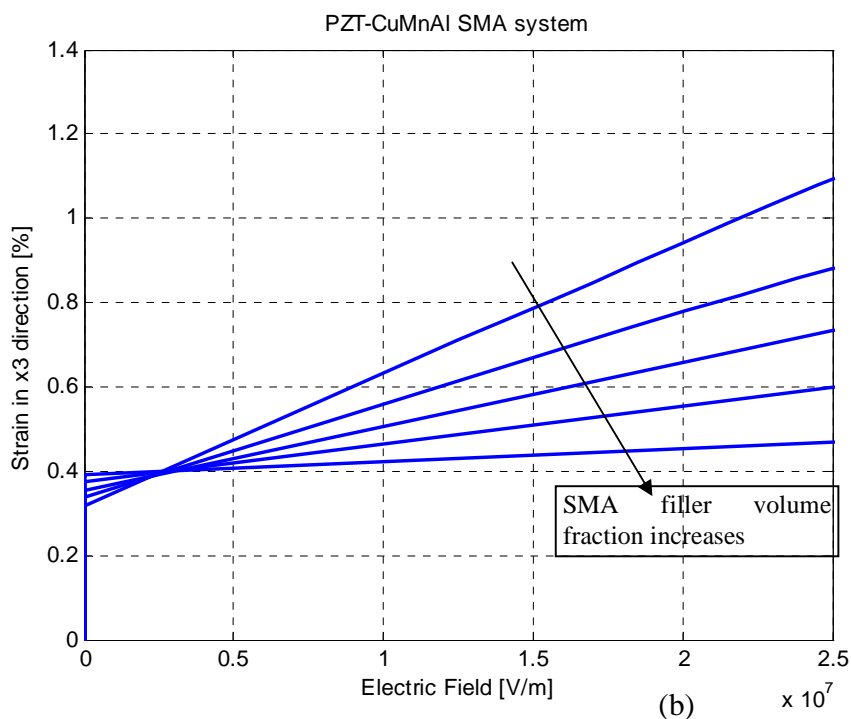
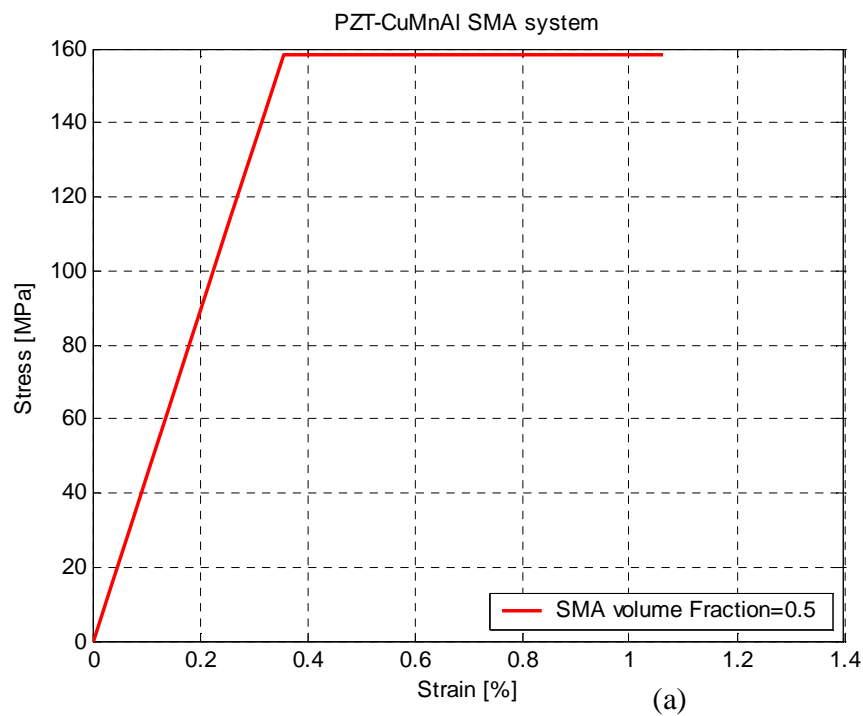


Figure 2.15. (a) Stress – Strain of the piezo-SMA composite SMA volume fraction of 0.5 and (b) E-Field – Strain for different SMA volume fractions by using 3-D model.

As the volume fraction of SMA phase increases, can be followed in Fig.2.15b, the required electric field to reach same amount of strain is also increasing. This is mainly because when the volume fraction of piezo phase decreases, the stress generated by piezoelectric material decreases for the same amount of electric field applied as well.

A new concept of piezo-SMA composite is proposed as a high performance actuator material under bias stress and applied electric field. The best piezo-SMA composite design for achieving highest strain is use of 1-D parallel composite design of Fig.2.3. To this end, a new analytical model based on Eshelby theory is developed, which can account for anisotropic matrix and linear SMA superelastic behavior. The experimental study is also performed in order to manufacture such a composite where the bonding is required between two phases; piezoelectric material and SMA. Spark Plasma Sintering (SPS) machine is used to create such a bonding between two materials. In SPS process, pressure and temperature are controlled to achieve the best sintering condition. In addition to several SPS condition, three different design conditions are also carried out as discussed in Experiments section, Fig.2.7. The overall results for SPS are tabulated. In all cases, the bonding is examined by nondestructive tests.

Chapter 3. The Piezo-SMA composite for Thermal energy harvesting

Piezoelectric materials and shape memory alloys (SMAs) are very common materials for actuators and sensors; however their composites as electrical generators are least explored, although use of piezoelectric as the mechanical energy harvester is increasingly popular.

This chapter of the dissertation thermal energy harvester using piezo-SMA composite is examined. Piezo-SMA composite is subjected to fluctuating temperature. The main mechanism of such a piezo-SMA composite is synergistic effect of piezoelectrics and SMA which are connected in series. Temperature fluctuation induces large straining first in the SMA phase then immediately stressing to the piezoelectric phase, thus, inducing charge by direct piezoelectric effect. In order to make this problem more analytically tractable, we are developing two models, simple laminated 1-Dimensional model and 3-D model with Eshelby's theory.

The piezo-SMA composite is made of two plates of piezoelectric ceramic and SMA, which are connected and compressed by the compression spring. The composite is modeled to have fixed displacement boundary condition to ensure the piezoelectric material is in compression throughout the process. Temperature fluctuation between martensite finish temperature (M_F) and austenite finish temperature (A_F) induces phase transformation in the SMA. Compressive stress is

generated during Austenitic transformation; due to heating in SMA phase and fixed displacement boundary condition and compressive stress reduces while SMA transforms to martensitic phase during cooling. The change in the compressive stress is converted into electrical energy by inverse piezoelectricity. The model predicts the available power according to material properties and thermal fluctuation. The impedance of the system is examined with different thermal fluctuating frequencies. Higher frequencies which result in lower impedance, give higher available power to electrical loading. The experimental and predicted results are in agreement for higher frequencies, while for lower frequencies of thermal fluctuation the prediction is not accurate due to internal loss.

3.1. Analytical Model of the Piezo-SMA Energy harvester

Analytical modeling consists of two sections; in the first step stress generated in the composite will be determined with two analytical models; one-dimensional serial composite model, and three-dimensional model with Eshelby's theory; for the second step the corresponding electric field generated by direct piezoelectricity will be calculated. It is convenient to develop analytical models that can predict the response of composite material made of piezoelectric material and SMA under different input conditions and for known material properties. In this section of the study, for hybrid composite, the analytical modeling is discussed. Stress generated during the thermal cycling environment is the key point in energy harvesting process, and should be predicted by using composite modeling theories. 1-D and

3-D approaches are discussed in this section to predict the stress generated. The predicted stress during phase transformation due to constrained recovery is used to generate electrical charge in piezo-phase by inverse piezoelectric effect, and later in the following sections the electrical model to estimate the available power from piezoelectric material is examined.

The mechanical and electrical behavior of a piezoelectric material can be modeled by two linearized constitutive equations. These equations contain two mechanical and two electrical variables. The direct effect can be modeled by following matrix equations (IEEE standard on Piezoelectricity, ANSI standard 176-1987):

$$\sigma_{ij} = C_{ijmn}\epsilon_{mn} + e_{nij}(-E_n) \quad (3.1)$$

$$\epsilon_{ij} = s_{ijkl}\sigma_{kl} + g_{kij}D_k \quad (3.2)$$

and converse piezoelectric effect can be modeled by following matrix equations:

$$D_i = e_{imn}\epsilon_{mn} - \kappa_{in}(-E_n) \quad (3.3)$$

$$-E_i = g_{ijk}\sigma_{jk} - \beta_{ij}D_i \quad (3.4)$$

Equations (3.1) and (3.3) can be represented in matrix notation as:

$$\Sigma = \mathbf{RZ} \quad (3.5)$$

Equations (3.2) and (3.4) can be represented in matrix notation as:

$$\mathbf{Z} = \mathbf{F}\boldsymbol{\Sigma} \quad (3.6)$$

3.1.1. One-Dimensional Modeling

In this section piezo-SMA composite is considered as one dimensional series composite model. Both piezo electric and SMA have finite thicknesses. They laminated together to form the energy harvesting composite. SMA used in this model is in martensitic phase at room temperature, Fig.3.1(a), this phase is called self-accommodated martensite, see Fig.1.20(a). Prestrain is introduced to SMA by simply loading and unloading it in martensite phase at room temperature, Fig.3.1(b), since SMA is martensitic in room temperature Shape Memory Effect (SME) is observed in this step and deformation in martensite proceeds by the growth of one variant at the expense of the other. Amount of the prestrain is determined by the loading stress, and here in this study it is assumed that the SMA is deformed less than 3% strain, see schematic representation in Fig.3.2. The deformed martensitic SMA, Fig.3.1(c), is attached to piezo and the laminated composite is clamped in a way that it has zero displacement boundary condition, see Fig.3.1(d). It is expected that upon heating above the austenite finish temperature, SMA exhibits shape memory effect and each variant reverts to the Austenitic phase in the original orientation by the reverse transformation, Fig.3.1(e). Due to fixed displacement boundary condition, where mechanical obstacle is assumed to be completely rigid and the contact strain is independent of temperature and stress; the phase transformation induced compressive stress in the composite. Both fiber (SMA phase) and matrix (Piezo phase) will be under

compression. After heating above the A_F temperature, maximum recovery stress is generated, here it is assumed that the stress generated is below the yielding stress of the SMA. The composite then cooled below the M_F temperature to finish the cycle, and the stress in the composite decreases to initial value, Fig.3.1(f).

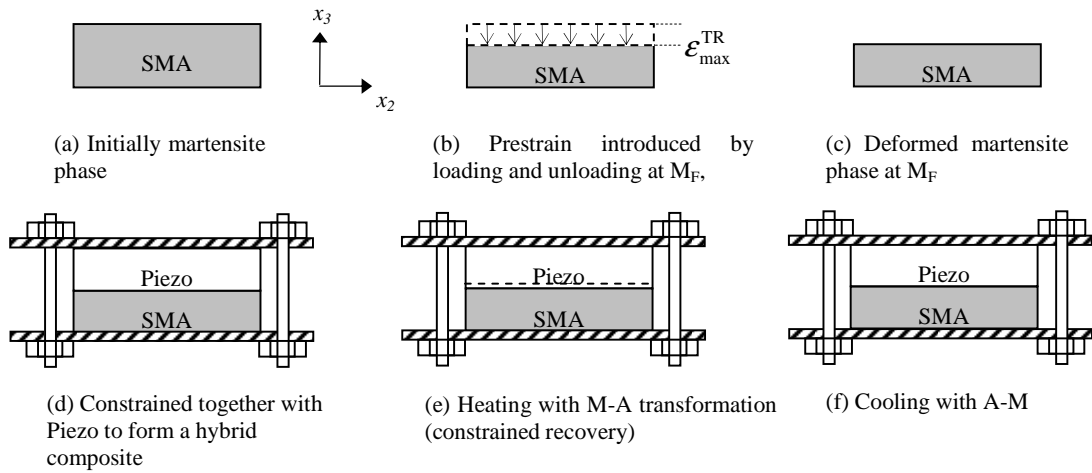


Figure 3.1. Modeling of Piezo-SMA composite.

A one-dimensional model for computing the stress in the Piezo-SMA composite generated by temperature induced martensitic and austenitic transformations is modeled by using iso-stress (constant stress) condition.

$$\sigma_c = \sigma_m = \sigma_f \quad (3.7)$$

where σ_c , σ_m and σ_f are the stress of composite, matrix and fiber, respectively.

Both piezo and SMA assumed to have the same cross-sectional area, and f

denotes the volume fraction of SMA phase in the composite design. During the constrained recovery, total deformation of the composite, δ_c is kept to be zero

$$\delta_c = \delta_f + \delta_m = 0 \quad (3.8)$$

where δ_m and δ_f are the deformation of matrix and fiber, respectively. Equation (3.8) can also be written in terms of constituents strains as

$$\varepsilon_c = f\varepsilon_f + (1-f)\varepsilon_m = 0 \quad (3.9)$$

since the cross-sectional area is uniform through x_3 -direction and the volume fraction of each constituent is linearly proportional to its thickness, deformation can be written as strain.

Total compressive strain for the piezo can be written as

$$\varepsilon_m = \varepsilon_m^{\text{TE}} - \varepsilon_m^{\text{el}} = \alpha_m \Delta T - \frac{\Delta \sigma_m}{E_m} \quad (3.10)$$

where $\varepsilon_m^{\text{TE}}$, α_m , $\varepsilon_m^{\text{el}}$, and E_m are the thermal strain, thermal expansion coefficient, elastic strain and Young's modulus of the piezo matrix. ΔT is the temperature difference between A_F and M_F , $\Delta T > 0$ for reverse (M \rightarrow A) transformation, and $\Delta T < 0$ for martensitic (A \rightarrow M) transformation. Total compressive strain for the SMA can be written as

$$\varepsilon_f = \varepsilon_f^{\text{TE}} + \varepsilon_f^{\text{TR}} - \varepsilon_f^{\text{el}} = \alpha_f \Delta T + \varepsilon_f^{\text{TR}} - \frac{\Delta \sigma_f}{E_f} \quad (3.11)$$

where $\varepsilon_f^{\text{TE}}$, $\varepsilon_f^{\text{TR}}$, $\varepsilon_f^{\text{el}}$, α_f , and E_f are the thermal strain, prestrain, elastic strain, thermal expansion coefficient and the austenite phase Young's modulus of SMA fiber phase. Assuming linear dependence of $\varepsilon_f^{\text{TR}}$, E_f and α_f (Tanaka, 1986)

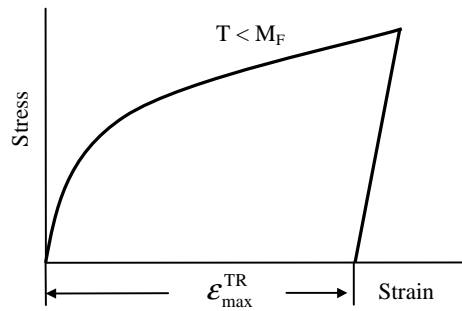


Figure 3.2. Schematic Stress-Strain curve of SMA to introduce prestrain, ε^{TR} .

$$\varepsilon_f^{\text{TR}}(\xi) = (1 - \xi) \times \varepsilon_{\text{max}}^{\text{TR}} \quad (3.12)$$

$$E_f(\xi) = \xi \times E_f^M + (1 - \xi) E_f^A \quad (3.13)$$

$$\alpha_f(\xi) = \xi \times \alpha_f^M + (1 - \xi) \alpha_f^A \quad (3.14)$$

where E_f^M , E_f^A , α_f^M , α_f^A and ξ are martensite phase Young's modulus, austenite phase Young's modulus, CTE of martensite phase, CTE of austenite phase and martensite volume fraction of fibers, respectively. ξ is a function of temperature and stress. ξ can be expressed for martensitic (A \rightarrow M) transformation, (Tanaka, 1986).

$$\xi(T, \sigma)_{A \rightarrow M} = 1 - \exp(a^M \times (M_s - T) + b_M \times \sigma_f) \quad (3.15a)$$

$$a^M = \frac{\ln(0.01)}{M_s - M_f}, \quad b_M = \frac{a^M}{C_M} \quad (3.15b)$$

and for reverse (M \rightarrow A) transformation as

$$\xi(T, \sigma)_{M \rightarrow A} = \exp(a^A \times (A_s - T) + b_A \times \sigma_f) \quad (3.16a)$$

$$a^A = \frac{\ln(0.01)}{A_s - A_f}, \quad b_A = \frac{a^A}{C_A} \quad (3.16b)$$

where T , σ_f , C_M , and C_A are temperature, the effective stress in fiber phase, slope of martensite transformation contour and slope of reverse transformation contour respectively.

Compressive stress across the composite in the x_3 -direction (along the thickness, Fig.3.1) can be found as;

$$\Delta\sigma_c = \frac{f \times (\alpha_f(\xi)\Delta T + \varepsilon_f^{\text{TR}}(\xi)) + (1-f) \times \alpha_m \Delta T}{\left[\frac{f}{E_f(\xi)} + \frac{1-f}{E_m} \right]} \quad (3.17)$$

The stress induced by phase transformation is determined. The value of the stress is highly proportional with the transformation stress that has defined in initial steps as $\varepsilon_{\text{max}}^{\text{TR}}$. Further deformation in martensite phase will induced more stress in the composite that can be converted into electrical energy by inverse piezoelectric

effect. The stiffness of both materials is another parameter that affects the amount of the stress. An increase in the stiffness of the piezo also increases the recovery stress. Stress relaxation during cooling cycle is not calculated since it is assumed that all the stress induced in heating cycle disappears during cooling cycle due to martensitic transformation in the SMA phase, where $\xi \rightarrow 1$.

One-dimensional model of energy harvester is finalized with the determination of the stress generated during the heating cycle; in the next section piezo-SMA composite will be examined by applying Eshelby's theory. The electrical model to convert mechanical energy into electrical energy will be discussed in later sections.

3.1.2. Three-Dimensional Modeling with Eshelby's Theory

A three dimensional analytical model for computing the stress and strain in the Piezo-SMA composite is examined by using Eshelby's inclusion method with Mori-Tanaka mean field theory. The schematic representation of the analytical model for the calculation of composite stress is shown in Fig.3.3 where phase transformation strain of fiber, thermal mismatch strains of fiber and matrix are shown. The composite consists of an infinite piezoelectric matrix (D - Ω) containing a finite volume fraction, f , of spheroidal SMA fillers (Ω). A deformation constraint is applied in x_3 -direction for generating the recovery stress during the thermal induced phase transformation, which is represented by F^o .

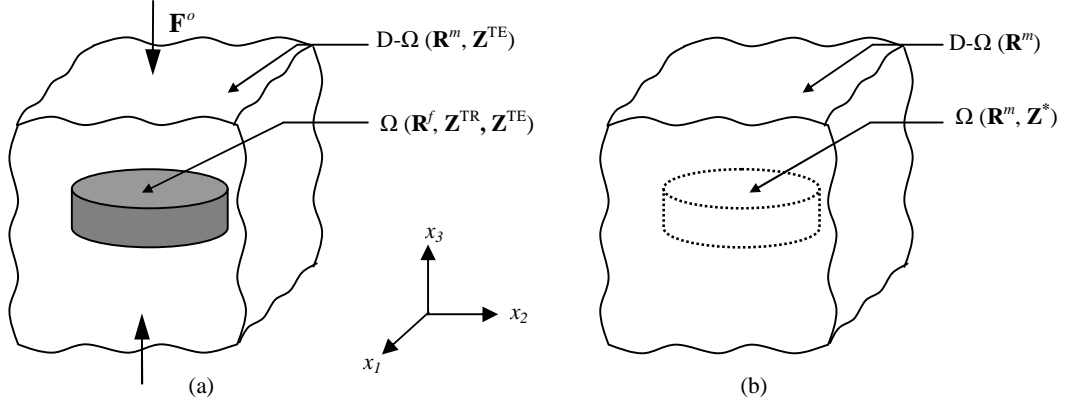


Figure 3.3. Analytical model for predicting residual stresses in SMA filler and piezo matrix, (a) original problem is converted to (b) Eshelby's equivalent inclusion problem.

The phase transformation strain of the SMA by the shape memory effect can be expressed as

$$\mathbf{Z}^{\text{TR}} = \xi \boldsymbol{\varepsilon}^{\text{TR}} \begin{bmatrix} -\nu_f & -\nu_f & 1 & 0 & 0 & 0 & 0 & 0 & 0 \end{bmatrix} = \xi \boldsymbol{\varepsilon}^{\text{TR}} \mathbf{V}^{\text{TR}} \quad (3.19)$$

where $\boldsymbol{\varepsilon}^{\text{TR}}$ and ν_f denote the phase transformation strain from austenite to martensite and Poisson's ratio of the SMA phase, respectively. ξ is expressed for martensitic transformation and for reverse transformation in Eqs.(3.15) and (3.16). The thermal mismatch strain is generated during the cooling and heating processes due to difference in coefficient of thermal expansions (CTEs) of the SMA and PZT, and it is expressed as

$$\mathbf{Z}^{\text{TE}} = \alpha^{\Delta} \begin{bmatrix} 1 & 1 & 1 & 0 & 0 & 0 & 0 & 0 & 0 \end{bmatrix} = \alpha^{\Delta} \mathbf{V}^{\text{TE}} \quad (3.20)$$

where $\alpha^\Delta = (\alpha_f - \alpha_m)\Delta T$, and α_f , α_m and ΔT are the CTEs of the fiber and matrix, and temperature change, respectively. Both Austenite and martensite phase have different CTEs, α_f which can be assumed to be linear function of ξ during the phase transformation, Tanaka (1986).

By using Eshelby's inclusion theory with Mori-Tanaka interaction effect, the stress distribution for SMA phase can be expressed as

$$\boldsymbol{\Sigma}^f = \mathbf{R}^f \cdot (\bar{\mathbf{Z}} + \mathbf{Z} - \mathbf{Z}^{\text{TE}} - \mathbf{Z}^{\text{TR}}) \quad (3.21)$$

$$\boldsymbol{\Sigma}^f = \mathbf{R}^m \cdot (\bar{\mathbf{Z}} + \mathbf{Z} - \mathbf{Z}^*) \quad (3.22)$$

where \mathbf{R} is the electro-elastic stiffness matrix, \mathbf{Z} is the field vector, $\bar{\mathbf{Z}}$ is the average elastic field in the matrix domain, \mathbf{Z}^* is the equivalent eigenfield of the equivalent inclusion, and superscripts f and m refer to the fiber and matrix, respectively. Electro-elastic stiffness of fiber \mathbf{R}^f depends on ξ and is assumed to be a linear function of ξ , Tanaka, 1986. Therefore electro-elastic stiffness matrix for SMA phase can be written as

$$\mathbf{R}^f = \xi \mathbf{R}_M^f + (1 - \xi) \mathbf{R}_A^f \quad (3.23)$$

where \mathbf{R}_M^f and \mathbf{R}_A^f are the electro-elastic stiffness of martensite and austenite phase of SMA, respectively.

The integration of the disturbance stress σ_{ij} over the entire domain (D) vanishes, average field disturbance in the matrix can be written as

$$\bar{\mathbf{Z}} = -f(\mathbf{Z} - \mathbf{Z}^*) \quad (3.24)$$

The total strain field \mathbf{Z} and \mathbf{Z}^* are related through

$$\mathbf{Z} = \mathbf{S} \cdot \mathbf{Z}^* \quad (3.25)$$

where \mathbf{S} is the coupled electro-elastic analog of Eshelby's tensor as defined by equation given in Mikata (2000) where $\beta \rightarrow \infty$ for elliptic crack like inclusions normal to x_3 -direction in transversely isotropic piezoelectric matrix. The tensor also can be found as a flat oblate spheroid (penny-shaped) inclusion embedded in a transversely isotropic piezoelectric matrix, is given by 9 by 9 matrixes, Taya (2005).

Rewrite Eq.(3.22) by plugging Eqs.(3.24) and (3.25) in terms of \mathbf{Z}^*

$$\boldsymbol{\Sigma}^f = (1-f)\mathbf{R}^m \cdot (\mathbf{S} - \mathbf{I}) \cdot \mathbf{Z}^* \quad (3.26)$$

In order to define eigenstrain, \mathbf{Z}^* one can equate Eqs.(3.21) and (3.22) and plug Eq.(3.25) to get,

$$\mathbf{Z}^* = \left[(1-f)(\mathbf{R}^f - \mathbf{R}^m) \cdot \mathbf{S} + \mathbf{R}^m + f(\mathbf{R}^f - \mathbf{R}^m) \right]^{-1} \cdot \mathbf{R}^f \cdot (\mathbf{Z}^{\text{TE}} + \mathbf{Z}^{\text{TR}}) \quad (3.27)$$

Equation (3.27) can be used in Eq.(3.26) to determine the flux vector

$$\begin{aligned} \boldsymbol{\Sigma}^f = & (1-f)\mathbf{R}^m \cdot (\mathbf{S}-\mathbf{I}) \cdot \left[(1-f)(\mathbf{R}^f - \mathbf{R}^m) \cdot \mathbf{S} + \mathbf{R}^m + f(\mathbf{R}^f - \mathbf{R}^m) \right]^{-1} \\ & \cdot \mathbf{R}^f \cdot (\mathbf{Z}^{\text{TE}} + \mathbf{Z}^{\text{TR}}) \end{aligned} \quad (3.28)$$

The average flux vector in the fiber, $\langle \boldsymbol{\Sigma}^f \rangle$ obtained as

$$\langle \boldsymbol{\Sigma}^f \rangle = \mathbf{RE} \cdot (\mathbf{Z}^{\text{TE}} + \mathbf{Z}^{\text{TR}}) \quad (3.29)$$

Since internal flux field over the entire composite domain vanishes, for matrix average flux vector,

$$\langle \boldsymbol{\Sigma}^m \rangle = \frac{f}{f-1} \mathbf{RE} \cdot (\mathbf{Z}^{\text{TE}} + \mathbf{Z}^{\text{TR}}) \quad (3.30)$$

where

$$\mathbf{RE} = (1-f)\mathbf{R}^m \cdot (\mathbf{S}-\mathbf{I}) \cdot \mathbf{A} \cdot \mathbf{R}^f \quad (3.31)$$

$$\mathbf{A} = \left[(1-f)(\mathbf{R}^f - \mathbf{R}^m) \cdot \mathbf{S} + \mathbf{R}^m + f(\mathbf{R}^f - \mathbf{R}^m) \right]^{-1} \quad (3.32)$$

It is noted that bold face, \mathbf{RE} , \mathbf{R}^i and \mathbf{A} are 9 by 9 matrices.

From Eq.(3.6) field tensor in matrix domain can be obtained as

$$\mathbf{Z}^m = \mathbf{F}^m \langle \boldsymbol{\Sigma}^m \rangle \quad (3.33)$$

where the material properties of matrix are used in determining the compliance property tensor, \mathbf{F}^m .

Stress generated during the reverse transformation of the SMA is predicted with using two approaches; one-dimensional model, and 3-D model with Eshelby's theory. Material properties and characterization of SMA will be discussed in the following section of this Chapter. Electrical model to predict the available power to an electrical load will be introduced. Characterization of the Piezo material used in thermal energy harvester will be also discussed later in the following sections.

3.1.3. 3-D Modeling with Superposition Principle

Two-phase composite comprised of piezo-SMA is proposed to harvest the energy from temperature cycle in the earlier sections. Estimation of work/energy that can be extracted from SMA which is under thermo mechanical induced transformation will be examined by examining the response of the composite during temperature cycling. Here the free energy response of the SMA should be described; Fig.3.4 shows the sketch of free energy response with respect to temperature of austenite and martensite phase of the SMA material. With stress free the austenite transformation happens around temperature T_0 , while with stress applied the free energy band for martensite phase decreased that cause transformation to happen in higher temperatures, shown as T_H in Fig.3.4. The austenitic transformation (martensite-to-austenite) occurs when the free energy of austenite becomes less than the free energy of martensite at a temperature higher than a critical temperature T_0 . The free energies of the two phases are equal at temperature T_0 . However, the transformation does not begin exactly at T_0 , in the absence of stress, at a temperature A_S (austenite start), which is higher than T_0 . The transformation

continues to evolve as the temperature is increased until a temperature denoted A_F (austenite finish) is reached. This temperature difference $A_F - A_S$ is an important factor in characterizing shape memory behavior.

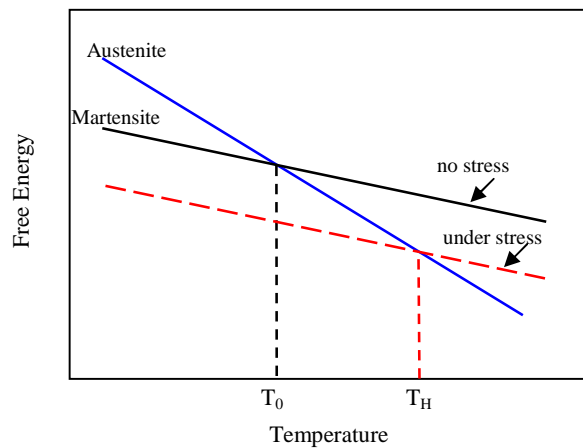


Figure 3.4. Free energy – Temperature diagram of SMA

When the SMA is cooled from the martensitic phase in the absence of stress, the reverse transformation (austenite-to-martensite) begins at the temperature M_S (Martensite start), and at the temperature M_F (martensite finish) the material is fully martensite. The equilibrium temperature T_0 is in the neighborhood of $(M_S + A_F)/2$. The spreading of the cycle ($A_F - A_S$) is due to stored elastic energy, whereas the hysteresis ($A_S - M_F$) is associated with the energy dissipated during the transformation. Due to the character of the martensitic transformation, applied stress plays an important role. During cooling of the SMA material below temperature M_S in absence of applied stresses, the variants of the martensitic phase arrange themselves in a self-accommodating manner through twinning, resulting in no observable macroscopic shape change. By applying mechanical loading to

force martensitic variants to reorient (detwin) into a single variant, large macroscopic inelastic strain is obtained. After heating to a higher temperature, the low-symmetry martensitic phase returns to its high-symmetry austenitic phase, and the inelastic strain is thus recovered. The martensitic phase transformation can also be induced by pure mechanical loading while the material is in the austenitic phase, in which case detwinned martensite is directly produced from austenite by the applied stress (Stress Induced Martensite, SIM) at temperatures above M_s .

SMA phase in piezo-SMA thermal energy harvester has constrained recovery boundary condition; i.e. the increase in the temperature induced stress which suppress the Austenitic transformation a bit. In order to complete further transformation, the temperature has to increase more. In this section of the dissertation, one complete cycle of the thermal energy harvester is examined with application of similar principle concept, i.e. Eshelby's theory, covered in the earlier section of the dissertation, however in a simpler way; where superposition principle is considered to simulate the Boundary Conditions (BCs) involved in the problem.

(1) The process of constrained recovery is possible only if the structure of SMA is stress-induced or oriented martensite. Therefore in the piezo-SMA thermal energy harvester concept the SMA phase initially cooled to lower temperature, in order to have martensite phase; then compression strain is introduced to SMA, $-\varepsilon^T$, schematically shown in Fig.3.5.

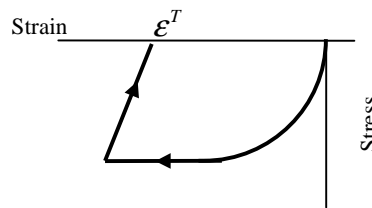


Figure 3.5. Stress–Strain curve for SMA which is at martensite phase

(2) Piezo-SMA composite formed where piezo is matrix and SMA phase has volume fraction, f , as can be seen in Fig.3.6. Here it is assumed that the interface between Piezo and SMA phases is stress free and perfectly bonded. And as mentioned before in the first stage, the temperature is less than M_F (martensite finish temperature).

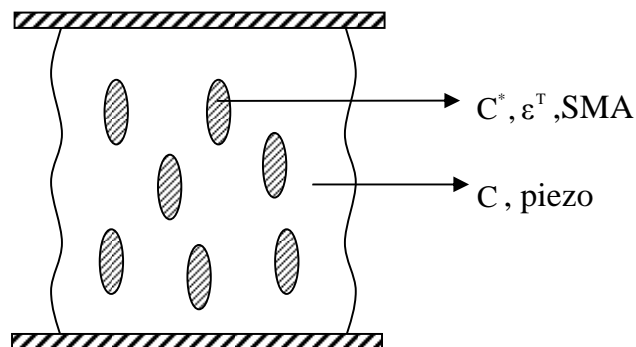


Figure 3.6. Schematic view of 2-phase Piezo-SMA composite with fixed displacement boundary condition.

(3) This stage the composite is subjected to heating with austenitic transformation. During heating when A_S is reached, reverse transformation starts and $\delta\epsilon_T$ is recovered and causes the compressive stress to induce. Then the reverse transformation is suppressed. To induce further transformation, the temperature

has to be increased. Eventually when the temperature at which σ_F is reached, reverse transformation completes, Fig.3.7.

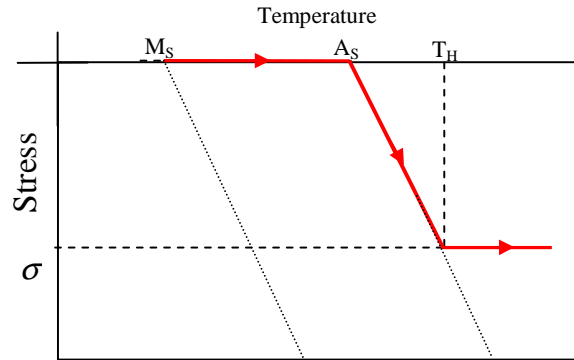


Figure 3.7. Temperature - Stress for heating cycle of Piezo-SMA composite.

During the complete austenitic transformation, amount of heat absorbed by SMA can be written as

$$\delta Q(T_H) = (T_H - T_0)\Delta s \quad (3.34)$$

where Δs is entropy difference between Martensite and Austenite phases of SMA.

(4) This stage the composite is subjected to cooling with A-M transformation. During cooling when M_S' is reached, forward transformation starts, compressive stress reduces by an amount of $\delta\sigma_F$ and forward transformation suppressed. To induce further forward transformation, temperature is decreased. Eventually when the compressive stress is totally released complete forward transformation occurs, schematically shown in Fig.3.8.

During complete martensitic transformation, heat that dissipates to the environment from SMA can be written as

$$\delta Q(T_L) = (T_L - T_0)\Delta s \quad (3.35)$$

where T_L is equal to the martensite start temperature, M_S .

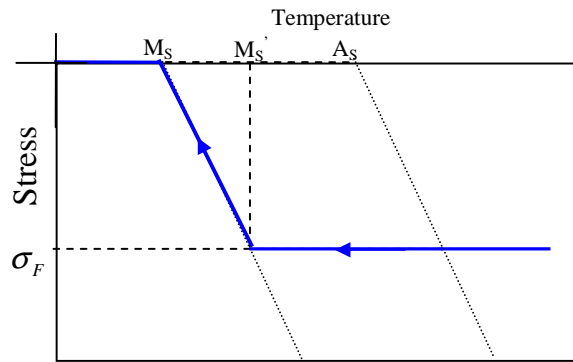


Figure 3.8. Temperature vs. Stress for cooling cycle of Piezo-SMA composite.

Total energy into SMA is can be represented as

$$\delta Q(T_H) + \delta Q(T_L) \quad (3.36)$$

However, the energy dissipation δW_D , which is shown as shaded area in Fig.3.9, should be subtracted from the total work, therefore total work extracted will be

$$\delta W = \delta Q(T_H) + \delta Q(T_L) - \delta W_D \quad (3.37)$$

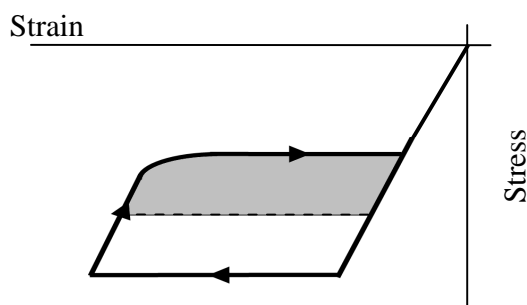


Figure 3.9. Stress-strain curve for SMA at a temperature higher than Austenite transformation finish temperature.

After covering what happens for a complete temperature cycle, mean value of stress in the Piezo domain will be calculated by the use of superposition principle in the following part of the dissertation.

The condition shown in Fig.3.6, which has fixed boundary in x_3 axis, can be divided into two different sub problems by superposition principle. The concept is schematically described in Fig.3.10.

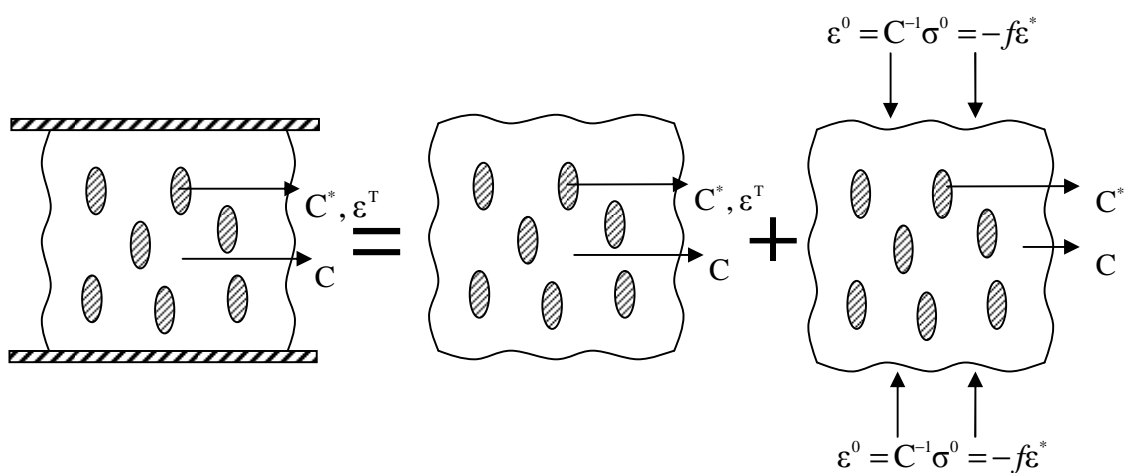


Figure 3.10. Original problem can be solved by superposition principle.

In order to calculate stress and strain in each individual problems; the subproblems are converted into Eshelby's equivalent inclusion problems, as referred by I and II respectively, shown in Fig.3.11.

(I) Boundary is stress (traction) free.

Actual eigenstrain in SMA = ε^T

The average stress in SMA can be found by using Eshelby theory with mean field method to reproduce average stress for equivalent inclusion as,

$$\begin{aligned} \langle \sigma \rangle_F^I &= C^* [-f(S-I)\varepsilon^* + S\varepsilon^* - \varepsilon^T] \\ &= C [-f(S-I)\varepsilon^* + S\varepsilon^* - \varepsilon^*] \end{aligned} \quad (3.38)$$

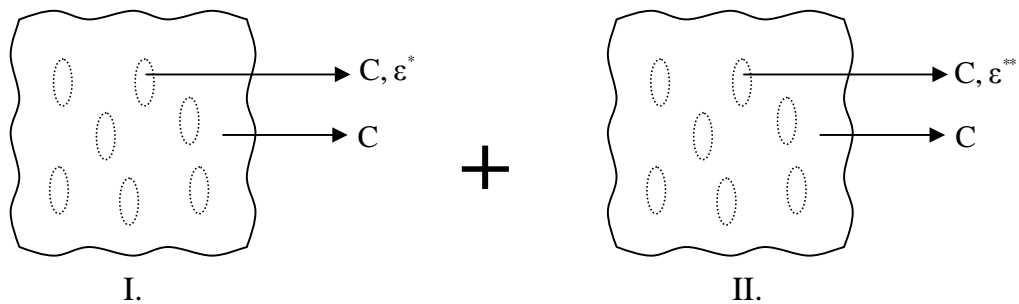


Figure 3.11. Original problem converted into Eshelby's equivalent inclusion problems.

Solving for ε^* gives the average stress in SMA domain.

The average stress in piezo,

$$\langle \sigma \rangle_M^I = -\frac{f}{1-f} \langle \sigma \rangle_F = -fC(S-I)\varepsilon^* \quad (3.39)$$

Note Eqs.(3.38) and (3.39) satisfies

$$f\langle \sigma \rangle_F^I + (1-f)\langle \sigma \rangle_M^I = 0 \quad (3.40)$$

Strain (total) in SMA,

$$\gamma_F^I = S\varepsilon^* - f(S-I)\varepsilon^* \quad (3.41)$$

Strain (total) in piezo,

$$\gamma_M^I = -f(S-I)\varepsilon^* \quad (3.42)$$

(II) Strain in x_3 -direction is set to be zero

In the traction free boundary condition (I), composite shows the average total strain as follows, by using rule of mixtures with Eqs.(3.41) and (3.43)

$$\langle \gamma \rangle = f\varepsilon^* \quad (3.43)$$

therefore to get zero strain in x_3 -direction the composite is elastically strained back by

$$\varepsilon^0 = -\langle \gamma \rangle = -f\varepsilon^* \quad (3.44)$$

Using Eshelby's theory with Mori-Tanaka mean field approach to reproduce average stress for equivalent inclusion yields,

$$\langle \sigma \rangle_F^{\text{II}} = C^* [\varepsilon^0 - f(S-D)\varepsilon^{**} + S\varepsilon^{**}] = C [\varepsilon^0 - f(S-D)\varepsilon^{**} + S\varepsilon^{**} - \varepsilon^{**}] \quad (3.45)$$

solving for ε^{**} gives the average stress in SMA domain.

The average stress in piezo,

$$\langle \sigma \rangle_M^{\text{II}} = \sigma^0 - fC(S-D)\varepsilon^{**} \quad (3.46)$$

Strain (total) in SMA,

$$\gamma_F^{\text{II}} = \varepsilon^0 + S\varepsilon^{**} - f(S-D)\varepsilon^{**} \quad (3.47)$$

Strain (total) in piezo

$$\gamma_M^{\text{II}} = \varepsilon^0 - f(S-D)\varepsilon^{**} \quad (3.48)$$

Summation of Eqs.(3.38) and (3.45) is the stress in SMA phase, when the composite has fixed displacement boundary condition (total strain=0). The stress in piezo can be found by superposing the solutions for (I) and (II) as,

$$\langle \sigma \rangle_M^{\text{I}} + \langle \sigma \rangle_M^{\text{II}} = -fC(S-D)\varepsilon^* + \sigma^0 - fC(S-D)\varepsilon^{**} \quad (3.49)$$

Equation (3.49) is used to determine the stress in piezo domain during thermal cycling. Strain in the Piezo domain can be also found by superimposing the solutions found in Eqs.(3.42) and (3.48).

Martensite Volume Fraction

Martensite volume fraction as a function of temperature is shown in Fig.3.12. During heating since a bit of transformation strain is recovered, compressive stress increases in the SMA domain, which suppresses the reverse transformation. Further transformation occurs when temperature is increased.

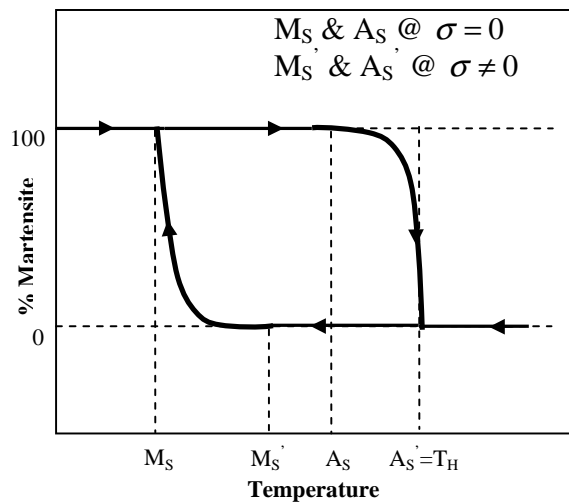


Figure 3.12. Martensite volume fraction as a function of Temperature of Piezo-SMA composite.

After determining the mean field stress in Piezo domain, the piezoelectricity will be used to convert mechanical energy into electrical energy.

3.2. Shape Memory Alloy (SMA) Material Characterization

In a shape memory alloy (SMA), the shape memory effect (SME) and super-elasticity (SE) or transformation pseudo-elasticity appear and are dependent on stress and temperature. In nitinol (NiTi) SMA, SME and SE appear due to the martensitic transformation (MT) and the rhombohedral phase transformation (RPT), Miyazaki (1984 and 1986), and Otsuka (1990). In applications as an actuator, a robot and a solid-state heat engine, a SMA is used as a working element which performs cyclic motions. The working characteristics of the SMAs are specified by the beginning and completion temperatures of the motion, the working stroke and the working force. These characteristic values are determined by the transformation temperature, the transformation strain and the transformation stress of the material.

In this section of the study, the material properties of SMA are examined. The experimental equipment used to characterize the shape memory behavior includes Differential Scanning Calorimeter (DSC), and Instron Mechanical Testing (Instron) machine. DSC is used to determine the temperatures associated with phase transformation within the SMA. Compression testing is performed with mechanical testing device to examine the SME of the material. Figure 3.13 shows the experimental setup used for homogenization of the SMA material used in this work. Homogenization conditions are 1000°C for 24 hours, Argon atmosphere followed by an ice water quenching. Rotary type vacuum pump is used to sweep the air environment prior to balancing inside of the quartz tube with Argon.

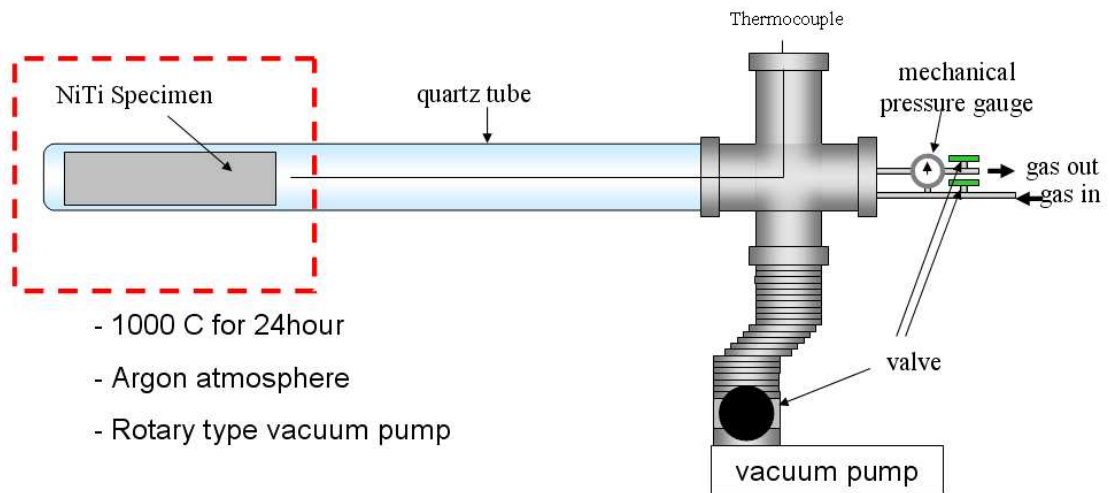


Figure 3.13. Setup used for homogenization of NiTi based SMA.

Nitinol (NiTi) material used in Piezo-SMA energy harvester model is a 51.2Ti-48.8Ni(at.%) SMA. In order to determine the transformation temperatures of the material, DSC is performed to the homogenized sample. A precise method of determining the transformation values at zero stress is to use a Differential Scanning Calorimeter (DSC). This DSC method yields a plot such as Fig.3.14 by measuring the amount of heat given off or absorbed by a tiny sample of the alloy as it is cooled or heated through its phase transformations. The DSC yields excellent, repeatable results on fully annealed samples (annealed at temperatures above 700°C for sufficient time to achieve a full anneal, generally about 10 to 15 minutes for small samples). One important drawback to the DSC method is that tests on partially cold worked materials, such as those used to optimize superelasticity, can yield poor, inconclusive results. This same drawback also may apply to samples which have undergone a heat treatment in the range of 400-600°C following cold working. Fully annealed DSC results are often used as

the basis for NiTi raw material selection since they effectively characterize the baseline properties of the material prior to cold working and heat treatment. The DSC results for the fully annealed material reported as: $M_S=313$ K, $M_F=293$ K, $A_S=328$ K and $A_F=343$ K. DSC graph is shown in Fig.3.14, note the temperature values are in Celsius in the graph. The hysteresis in transformation is measured to be approximately 50K.

The peak in cooling curve, Fig.3.14, is called martensitic, $B2 \rightarrow B19'$ transformation, the starting and ending temperature values corresponds the martensitic starting temperature, M_S and martensitic finish temperature, M_F , respectively. This helps to find the critical temperatures for the SMA that is used in experimental part of the dissertation.

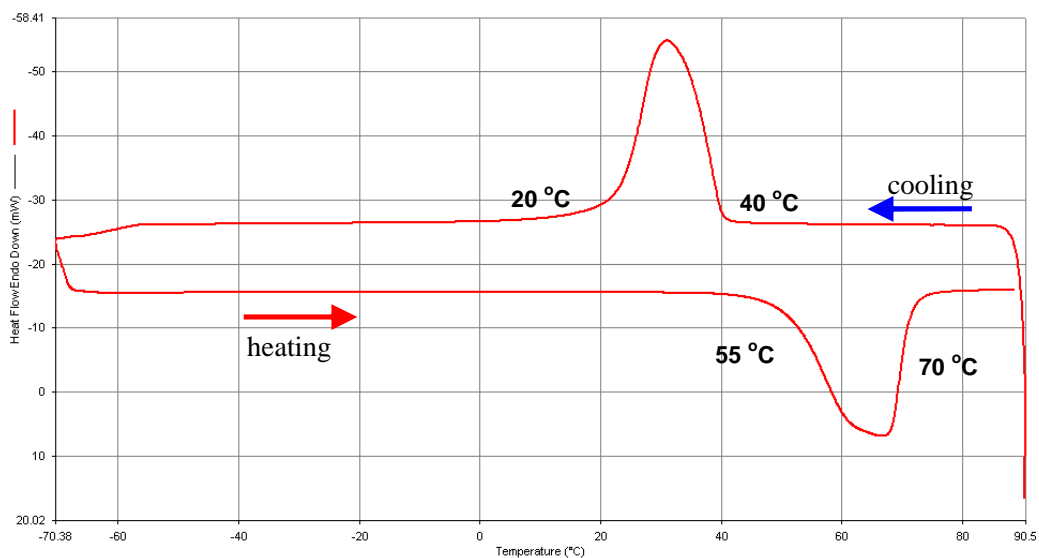


Figure 3.14. DSC result of 51.2Ti-48.8Ni (at.%) SMA.

It is experienced from the study that Ti-content, aging, thermo-mechanical treatment and additional of alloying elements, are important for controlling the memory behavior, in other words one can change the critical transformation temperatures by simple changing the Ti content in the NiTi alloy and heat treatment. Since having a martensite phase SMA at room temperature the material described above, in Fig.3.14 is used in the experimental work of the dissertation.

The stress-strain properties of the SME were examined for the SMA material, see Fig.3.15. At first, the loading and unloading processes with maximum strain $\epsilon_{\max}^{\text{TR}}$ were performed at a low temperature T_L below martensite finish temperature, M_F . While maintaining zero loading, by simple using the load control option of Mechanical Testing device, the sample was heated to high temperature T_H above Austenite finish temperature, A_F and the process is followed by cooling to T_L .

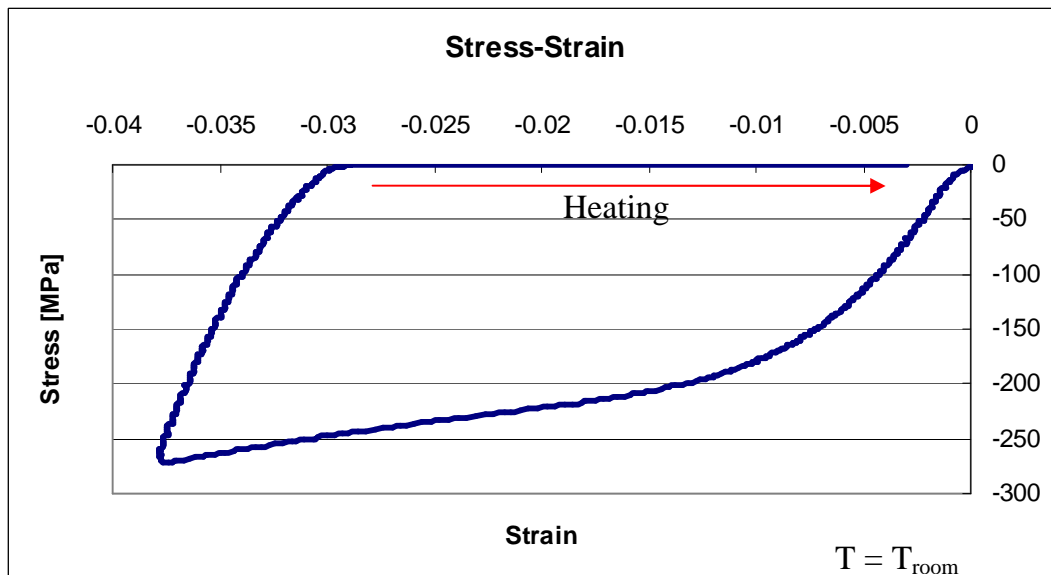


Figure 3.15. Stress-Strain response of 51.2Ti-Ni (at.%) SMA, at 300K

Starting material for SMA phase used in energy harvester is deformed (twinned) martensite as discussed before; therefore the pre-strain introduced by compressive stress is a key parameter to be measured before going to further steps in the experimental study. Defining the pre-strain is performed simply by using the Stress-Strain curve generated by compressive testing followed by heating above A_F temperature.

After Stress-Strain testing, the case that shown in Fig.3.15 is selected to be used as the material properties of the SMA used in experimental study and analytical modeling. Approximately 2.5% compressive strain is introduced to NiTi material, as it can be seen from the figure most of the strain can be recovered by Shape Memory Effect (SME) simply by heating above the A_F temperature.

Experiments in order to characterize the material properties of SMA yield the design variables such as critical temperatures of phase transformations, pre-strain that is introduced by simply loading and unloading the SMA at a temperature below than the martensite finish temperature and other mechanical properties such as Martensitic and Austenitic Young's modulus. With all parameters, 1-D model and 3-D model with Eshelby's theory, the stress generation in the composite, especially in piezoelectric material phase, will be predicted.

The results are shown in Fig.3.16 for 1-D model and Fig.3.17 for 3-D model, respectively. From both 1-D and 3-D result one can tell that during heating when A_S is reached, reverse transformation starts and small amount of transformation

strain, $\delta\varepsilon_{TR}$ is recovered and causes the compressive stress to induce. Then the reverse transformation is suppressed. If the temperature had not been increasing at this point, the recovery stress generation would have stopped; however, temperature increases and induces further transformation. Eventually when the temperature at which maximum recovery stress is reached; reverse transformation is complete.

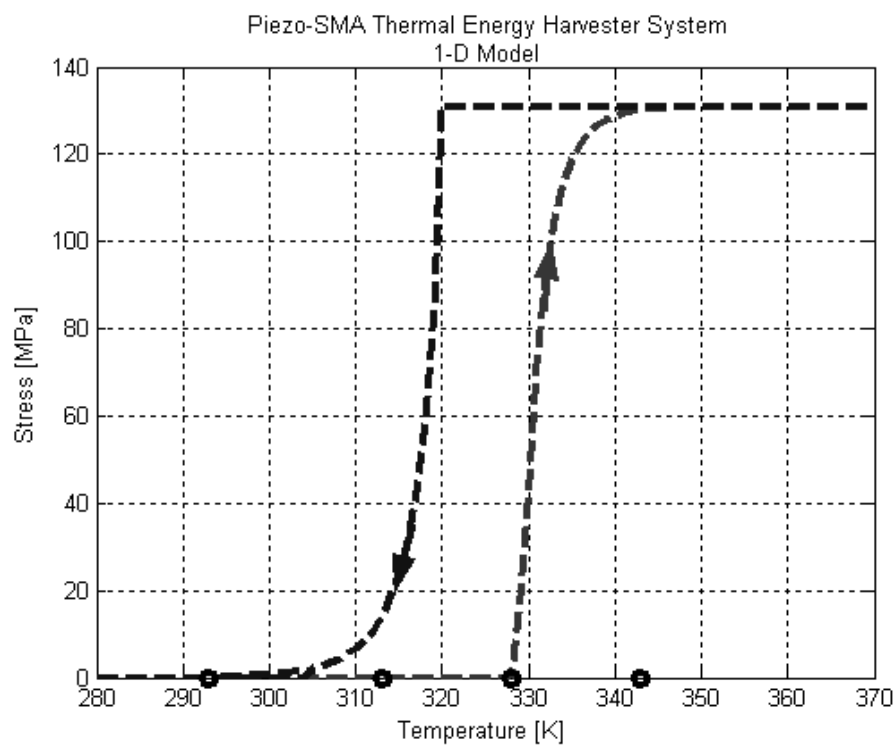


Figure 3.16. Effective piezo stress based on 1-D model as a function of temperature (Namli and Taya, 2011).

During cooling when M_S is reached, forward transformation starts, compressive stress reduces by an amount of $\delta\varepsilon_{TR}$ and forward transformation suppressed. To

induce further forward transformation, temperature is decreased. Eventually when the compressive stress is totally released complete forward transformation occurs.

With the material properties and thermal boundary conditions, i.e. heating above the A_F followed by cooling below M_S temperature, the stress generated during constrained recovery in piezoelectric phase, x_3 -direction, calculated as ~ 130 MPa with 1-D model and ~ 110 MPa with 3-D Model with Eshelby's Theory. It is noted that even though it has been taken into consideration in the analytical model calculation, thermal expansion is neglected in predicting the results.

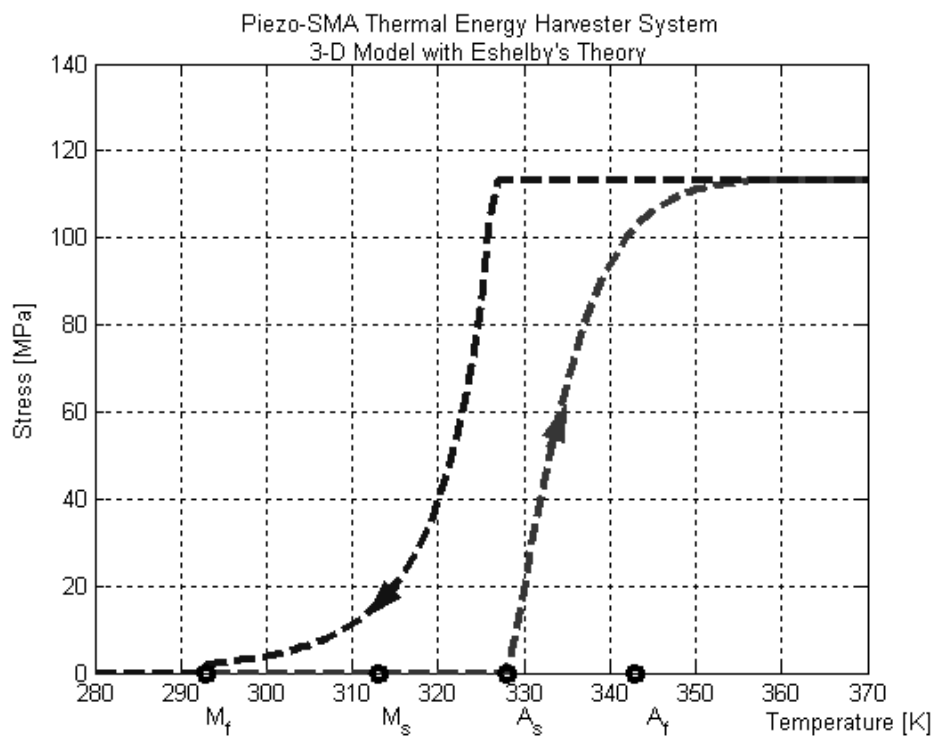


Figure 3.17. Effective piezo stress based on 3-D model with Eshelby's Theory as a function of temperature (Namli and Taya, 2011).

Martensite volume fraction of the SMA phase is exponentially related to temperature and effective stress in SMA phase within the composite, as formulated in Eqs.(3.15 and 3.16). For the numerical computation of the effective matrix stress the martensite volume fraction with respect to temperature is also plotted as in Fig. 3.18.

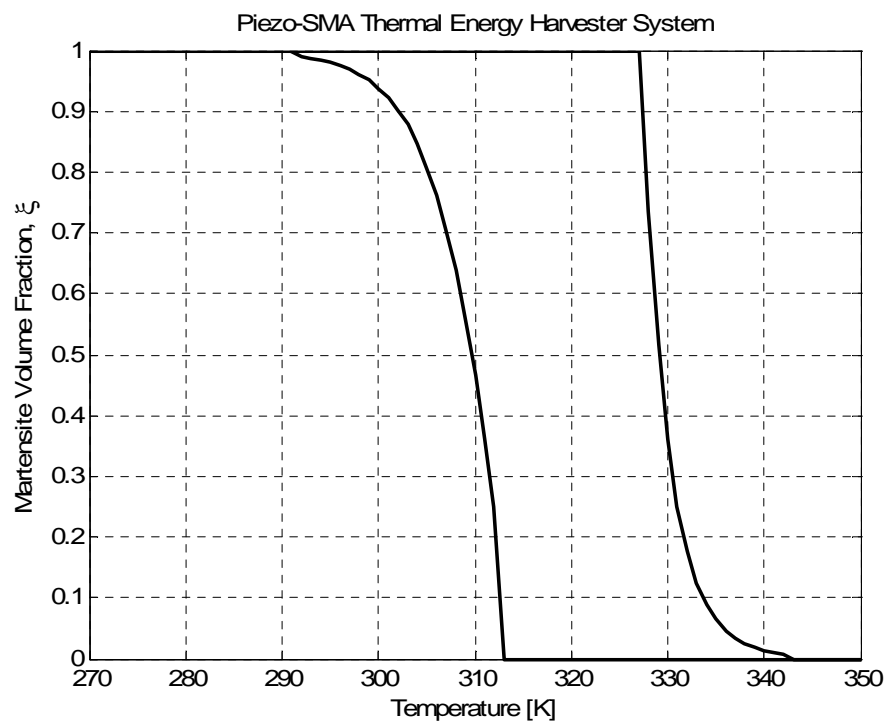


Figure 3.18. Martensite volume fraction of the piezo-SMA composite during thermal cycling based on 3-D model with Eshelby's Theory

3.3. Electrical Model

It is convenient to develop analytical models that can predict the response of these piezoelectric elements under different input conditions and for various material properties. It is known that piezoelectric material properties are not constant at all

as they depend in a nonlinear fashion on conditions such as mechanical and electrical boundary conditions, and the frequency and amplitude of the excitation force profile. These effects must be considered when using this model to predict piezoelectric response under conditions significantly different from those for which the model parameters are determined.

The piezoelectric material also has a considerable impact on achievable performance of the transducer. Commonly used piezoelectric materials are based on Lead Zirconate Titanate (PZT) ceramics. Assuming that a PZT disk is directly used as a transducer, the significant material parameters can be outlined to provide the material figure of merit. There are many factors that influence the selection of the PZT composition. The constitutive equations for a linear piezoelectric material under low stress levels can be written by recalling Eqs.(3.2) and (3.4) as;

$$\varepsilon_{ij} = s_{ijkl}\sigma_{kl} + g_{kij}D_k \quad (3.2)$$

$$-E_i = g_{ijk}\sigma_{jk} - \beta_{ij}D_i \quad (3.4)$$

where σ is the stress, D is the electric displacement, E is the electric field, s is the elastic compliance, and g is the piezoelectric voltage coefficient given as

$$g = \frac{d}{\kappa_o \kappa} \quad (3.50)$$

here, d is the piezoelectric constant and κ is the dielectric constant. The constant β in Equation (3.4) is the dielectric susceptibility, and equal to the inverse

dielectric permittivity tensor component. Under applied force $F = \sigma \cdot A$ (where A is the effective area), the open circuit output voltage (V) of the piezoelectric material can be computed from Eq(3.4), and given as;

$$V = E \cdot t = -g \cdot \sigma \cdot t = -\frac{g \cdot F \cdot t}{A} \quad (3.51)$$

where t is the thickness of the piezoelectric material. The charge (Q) generated on the piezoelectric can be determined from Eq(3.2) and given as;

$$D = \frac{Q}{A} = \frac{E}{\beta} = \frac{V \cdot \kappa_o \kappa}{t} \quad (3.52)$$

or

$$Q/V = \frac{\kappa_o \kappa \cdot A}{t} = C \quad (3.53)$$

where C is the capacitance of the material. The above relationship shows that at low frequencies a piezoelectric plate can be assumed to behave like a parallel plate capacitor. Hence, electric power available under the cyclic excitation with frequency, f , is given as follows;

$$P = \frac{1}{2} CV^2 \cdot f \quad (3.54)$$

or

$$P = \frac{1}{2} \frac{d^2}{\kappa_o \kappa} \cdot F^2 \cdot \frac{t}{A} \cdot f \quad (3.55)$$

Under certain experimental conditions, for a given material of fixed area and thickness, the electrical power is dependent on the d^2/κ ratio of the material. A material with a high d^2/κ ratio will generate high power when the piezoelectric ceramic is directly employed for harvesting energy.

It is also worth investigating the maximum open circuit output voltage that the sample can reach by pyroelectric effect. The piezoelectric governing equation can be rewritten to include pyroelectricity as

$$D_i = e_{ijk} \epsilon_{jk} - \kappa_{in} (-E_n) + p_i (\Delta T) \quad (3.56)$$

where ΔT is the temperature difference between cold and hot state, and p is the pyroelectric constant. Open circuit voltage can be found as

$$V_{pyro} = \frac{A \cdot p \cdot \Delta T}{C} \quad (3.57)$$

where A is the surface area and C is the capacitance of the piezo material. Available power, with pyroelectric effect, can be calculated by parallel plate estimation

$$P_{pyro} = \frac{1}{2} C V_{pyro}^2 \cdot f \quad (3.58)$$

3.4. Experimental Study

Modeling of piezo-SMA composite as a thermal energy harvester material has been discussed in previous sections, here design specifications are summarized based on modeling and material properties. Prediction of the experimental condition is done based on simple 1-D model. The material properties used in experimental study is shown in Table 3.1. These properties are used in 1-D modeling to predict stress in piezo phase and the power available to electrical loading which will be discussed in later sections.

Table 3.1. Material Properties of PZT and SMA

	PZT 855 ^a	SMA - 51.2Ti-Ni(at.%) SMA	
		Austenite	Martensite
Young's Modulus [GPa]	$C_{11} = 56, C_{33} = 51$	46	28
CTE [$10^{-6}/^{\circ}\text{K}$]	7.5	11	6.6
Piezoelectric Charge Constant [10^{-12} C/N]	$d_{33} = 600, d_{31} = -276, d_{15} = 720$		
Piezoelectric Voltage Constant [10^{-3} Vm/N]	$g_{33} = 21, g_{31} = -9, g_{15} = 27$		
Transformation Temperatures [K]		$M_F = 293 \text{ K}, M_S = 313 \text{ K}, A_S = 328 \text{ K}, A_F = 343 \text{ K}$	
Permittivity of free space [F/m]	8.85×10^{-12}		

^a APC International Ltd, http://www.americanpiezo.com/materials/apc_properties.html

One-Dimensional serial model is used to predict stress generated during thermal cycling process of the composite. By neglecting the thermal expansion term in Eq.(3.17) the stress equation reduces to;

$$\Delta\sigma = \frac{f\varepsilon_f^{\text{TR}}(\xi)}{\left[\frac{f}{E_f(\xi)} + \frac{1-f}{E_m} \right]} \quad (3.59)$$

As martensite volume fraction $\xi \rightarrow 0$, the stiffness of the SMA phase approaches the Austenite stiffness, $E_f(\xi) \rightarrow E_f^A$. With volume fraction $f = 0.1$ and pre-strain, as shown in Fig.3.5, $\varepsilon_f^{\text{TR}}(\xi) = 0.025$, the stress change is calculated as approximately 130 MPa. The material dimensions for SMA are given as; diameter 4.4 mm, the peak force exerted on PZT can be calculated as;

$$F = \Delta\sigma \cdot A = (130)(\pi d^2 / 4) = 2 \text{ kN} \quad (3.60)$$

Now that the force is predicted by using one dimensional model the response of PZT for the same loading condition with different frequencies are experimentally measured in order to find the power available to electrical load.

The voltage can be calculated by inverse piezoelectricity, Eq.(3.51), and it is found to be ~200 Volt with the given material properties, See Table 3.1 and the predicted load from, Eq.(3.60). Assuming at low frequencies the PZT behaves like a parallel plate capacitor, power available from PZT can be calculated for the known excitation frequency, f .

Here the concept of impedance matching is also convenient to discuss; in electrical engineering, the maximum power transfer theorem states that to obtain maximum external power from a source with a finite internal impedance, the impedance of the load must be made as same as that of the source. Therefore the power equation for the electrical load, P_L connected to PZT source can be derived by using the simple circuit shown in Fig.3.19.

The current, I , can be written as;

$$I = \frac{V}{Z + Z_L} \quad (3.61)$$

and the voltage, V_L , over the electrical load Z_L ;

$$V_L = V \frac{Z_L}{Z_L + Z} \quad (3.62)$$

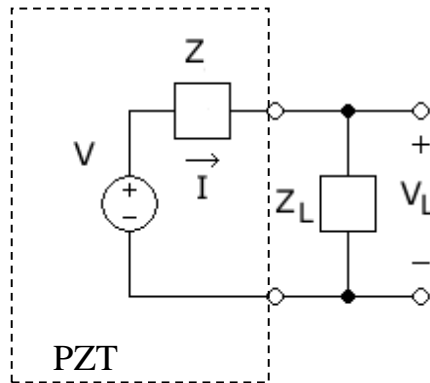


Figure 3.19. Schematic representation of PZT that is connected to electrical loading.

The maximum power transfer theorem states that $Z_L = Z$, then power at electrical load can be calculated from $P_L = I \cdot V_L$

$$P_L = \left[\frac{V}{Z + Z_L} \right] \cdot \left[V \frac{Z_L}{Z_L + Z} \right]_{Z=Z_L} = \left[\frac{1}{4} \right] \frac{V^2}{Z} \quad (3.63a)$$

Open circuit power, P , for piezoelectric material is predicted with Eq.(3.54) or Eq.(3.55),

$$P_L = \left[\frac{1}{4} \right] \frac{V^2}{Z} = \left[\frac{1}{4} \right] \frac{1}{2} CV^2 \cdot f \quad (3.63b)$$

Equations (3.63) relates the power at electrical load to power available from PZT material, and it shows that only $\frac{1}{4}$ of the power is available for electrical loading. This information is very important before going in to further steps in experimental study where the impedance of the piezoelectric material will be determined at different frequencies with different electrical loading conditions; in order to find impedance of the piezoelectric system and the maximum power available to electrical load.

3.5. Piezoelectric Material (PZT) Characterization

In order to determine the power available to electrical load from the PZT material in the piezo-SMA thermal energy harvester some sets of experiments are carried out with different frequencies.

For each case, at a fixed frequency, different load resistances are connected to PZT material. Cyclic mechanical loading is applied to PZT in order to determine the impedance for the PZT that is used in thermal energy harvesting design. The schematic representation of the electrical circuit used in these set of experiments are shown in Fig.3.19. Here it is modeled that PZT behaves as a voltage generator with an internal impedance of Z and the electrical load Z_L is connected to output of the PZT material. The voltage over electrical load is monitored with DAQ. And the current over the electrical load is simply calculated by Ohm's Law.

Figures 3.20 and 3.21 summarize the experiments performed by loading condition, 2kN at 0.01Hz. In this experiment piezoelectric material is subjected to cyclic loading with mechanical testing device, loading is compressive all time which is varying from 0 to 2kN. Load resistance is increased and the experiment performed with the same condition till the voltage across the load resistance is saturated the voltage and current is plotted versus load resistance as can be seen in Fig.3.20, and the power available to electrical load is shown in Fig. 3.21.

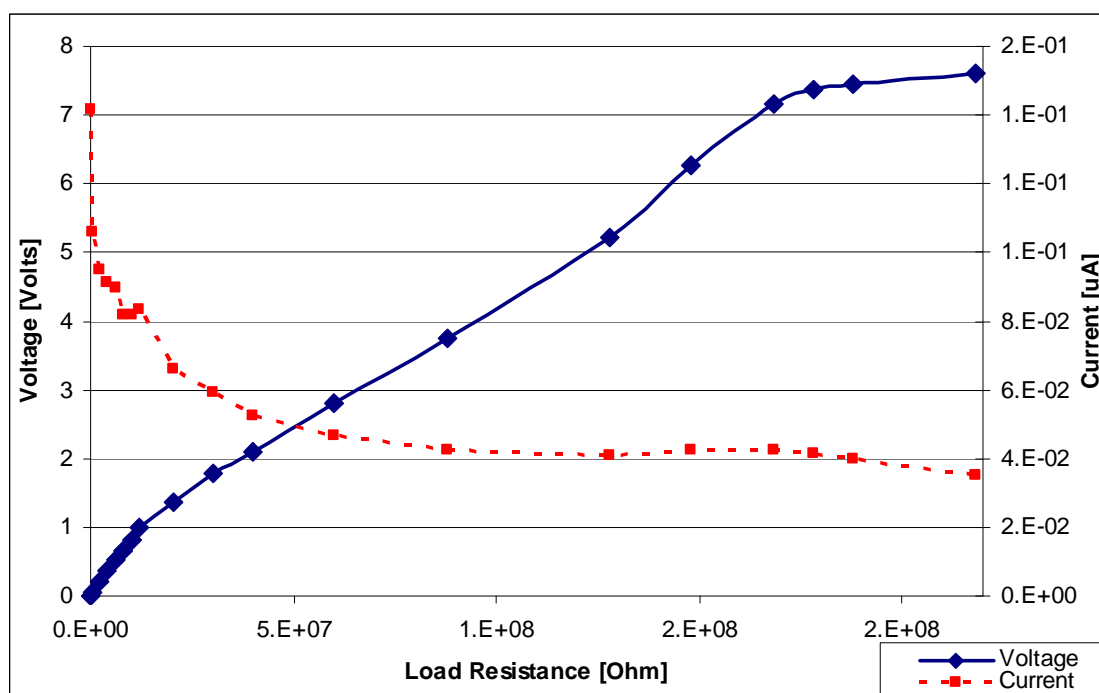


Figure 3.20. Voltage and Current response for 0.01 Hz, 2kN loading

As it can be seen from Fig.3.20, the maximum average power at the electrical load can be found at electrical load of $\sim 180 \text{ M}\Omega$ where the voltage is measured to be

~7.4 Volts, and the current over the resistance, calculated by Ohm's Law, is 0.042 μA . The average power is measured as

$$P_L^m = V_L^m \cdot I_L^m = 0.31 \mu\text{W}. \quad (3.64)$$

where superscript “ m ” represents the values are measured.

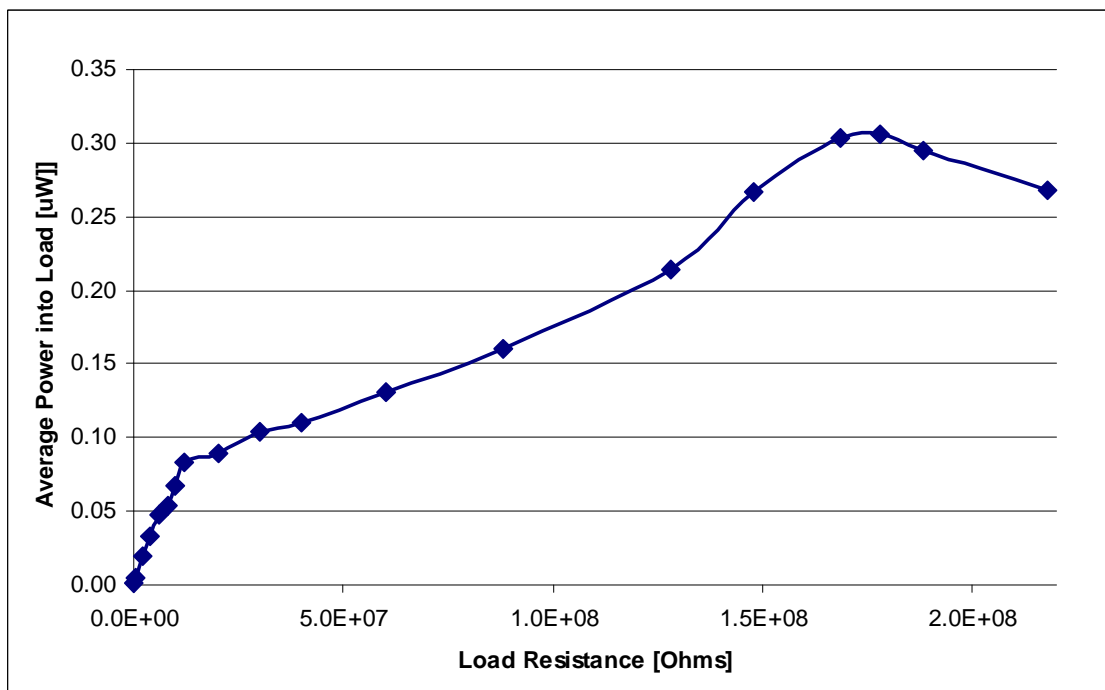


Figure 3.21. Average power at the electrical load for different electrical loading 0.01 Hz, 2kN loading

Recall Equation (3.63) which relates the power at electrical load to power available from PZT material with known excitation frequency, which is 0.01 Hz;

$$P_L = \left[\frac{1}{4} \right] \frac{V^2}{Z} = \left[\frac{1}{4} \right] \frac{1}{2} CV^2 \cdot f = 0.95 \mu\text{W} \quad (3.65)$$

By comparing the results in (3.64) and (3.65) it is convenient to say that the analytical approach by predicting the stress and the power available at electrical loading is not predicting the power available at electrical load accurately. This is because of the internal loss due to low frequency excitation which is not considered in the analytical model.

In the 0.01 Hz 2 kN experiments the impedance of the PZT from maximum load transfer theorem is found to be 180 M Ω , which is relatively high in order to build an electrical circuit to store the available power from the energy harvesting composite.

The frequency is a key variable in the power calculation as discussed previous sections, in order to see the effect of frequency to the average power available at the electrical load, PZT experiment is carried out with different frequency conditions; the second set of the experiments performed with 0.05 Hz, 2kN loading condition. The results are summarized in Figs.3.22 and 3.23. With an increase of 5 times in the frequency the maximum power available at electrical load is measured to be $\sim 2.6 \mu\text{W}$.

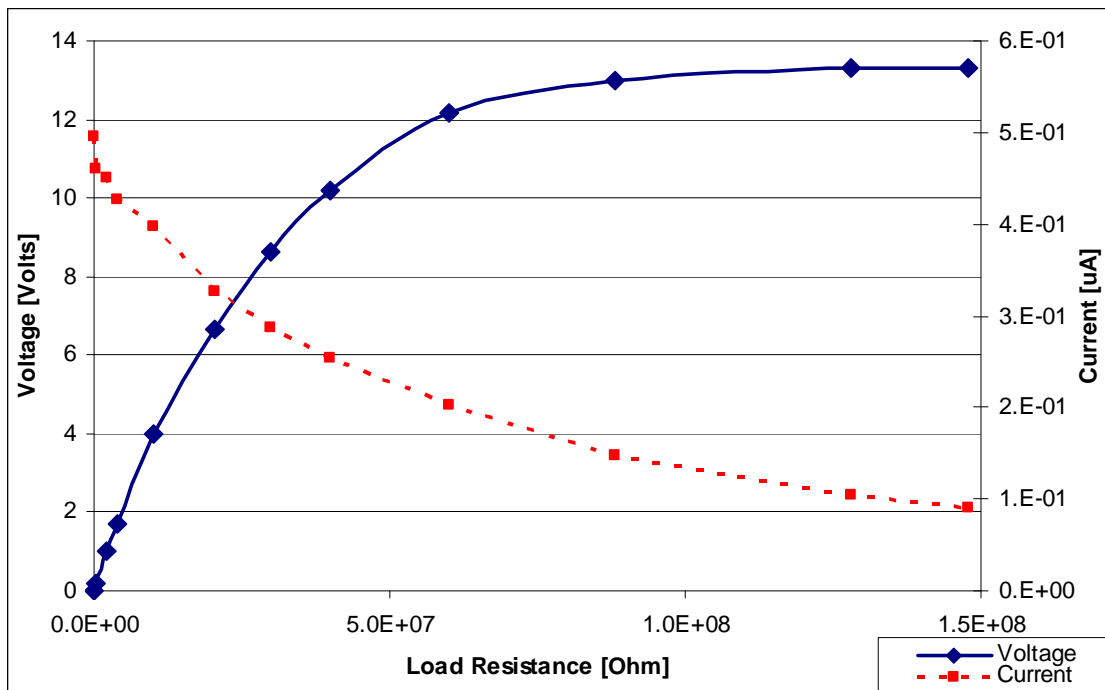


Figure 3.22. Voltage and Current response for 0.05 Hz, 2kN loading

At low values of resistance no voltage is produced (short circuit) and no power is generated. At high resistances (open circuit) no current flows and no power is generated. As the input frequency increases, the maximum efficiency occurs at smaller load resistance values. This is the behavior expected for an essentially capacitive device; as the excitation frequency increases, the source impedance $Z = 1/j\omega C$ will decrease. Therefore by assuming the capacitance is not changing during the process the expected internal impedance at 0.05 Hz is expected to be 5 times smaller than the internal impedance determined for 0.01 Hz case. By checking the maximum power transfer theorem for 0.05 Hz, the internal resistance is found to be 40 M Ω , which is 4.5 times smaller than the load value found in 0.01

Hz experiment with maximum power theorem. Analytical model shows a reasonable agreement with experimental results in this manner.

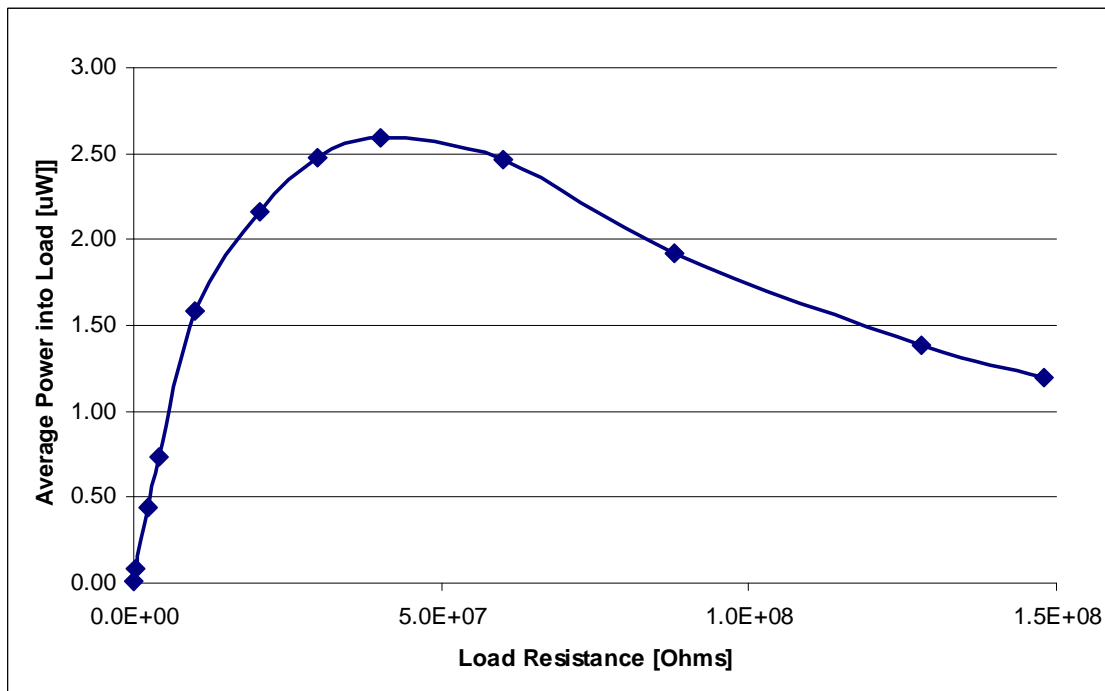


Figure 3.23. Average power at the electrical load for different electrical loading 0.05 Hz, 2kN loading

As it can be seen from Fig.3.23, the maximum average power at the electrical load can be found at electrical load of $\sim 40 \text{ M}\Omega$ where the voltage is measured to be $\sim 10.2 \text{ Volts}$, and the current over the resistance, calculated by Ohm's Law, is $0.26 \mu\text{A}$. The average power is measured as

$$P_L^m = V_L^m \cdot I_L^m = 2.6 \mu\text{W}. \quad (3.66)$$

where superscript “*m*” represents the values are measured.

Recall Equation (3.63) which relates the power at electrical load to power available from PZT material with known excitation frequency, which is 0.05 Hz;

$$P_L = \left[\frac{1}{4} \right] \frac{V^2}{Z} = \left[\frac{1}{4} \right] \frac{1}{2} CV^2 \cdot f = 4.75 \mu\text{W} \quad (3.67)$$

Again the analytical prediction for power available at electrical load over predicts the value for 0.05 Hz case.

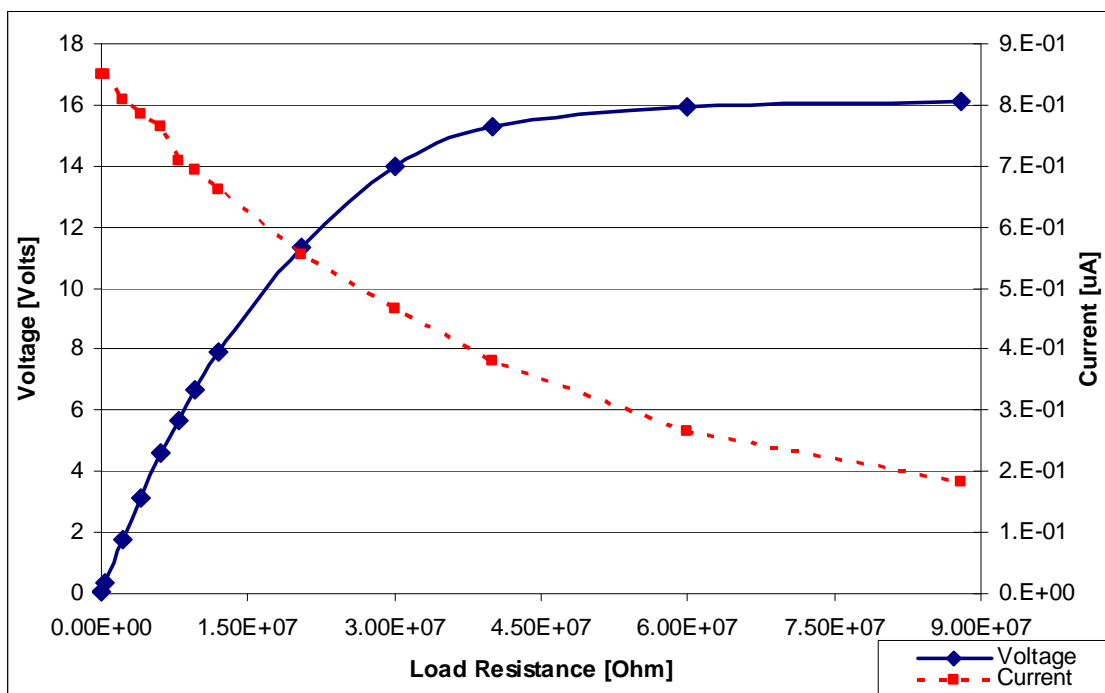


Figure 3.24. Voltage and Current response for 0.1 Hz, 2kN loading

The third set of the experiments performed with 0.1 Hz, 2kN loading condition. The results are summarized in Figs.3.24 and 3.25. With an increase of 2 times in the frequency the maximum power available at electrical load is measured to be ~6.4 µW.

As it can be seen from Fig.3.25, the maximum average power at the electrical load can be found at electrical load of $\sim 22 \text{ M}\Omega$ where the voltage is measured to be $\sim 13 \text{ Volts}$, and the current over the resistance, calculated by Ohm's Law, is $0.52 \mu\text{A}$. The average power is measured as

$$P_L^m = V_L^m \cdot I_L^m = 6.4 \mu\text{W}. \quad (3.68)$$

where superscript “ m ” represents the values are measured.

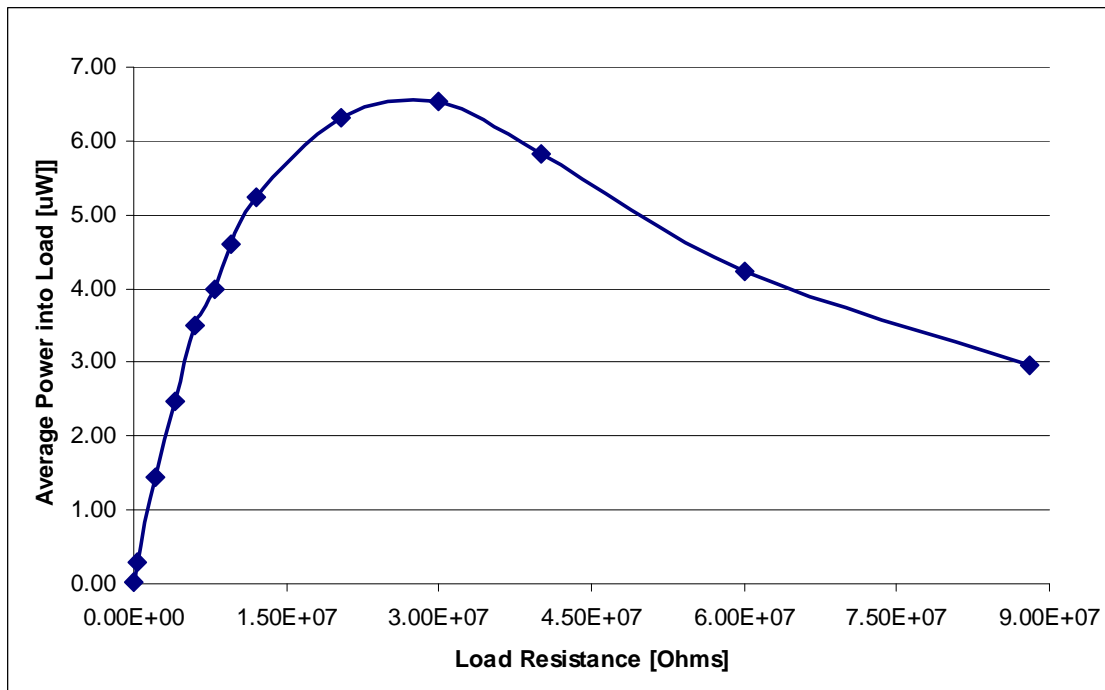


Figure 3.25. Average power at the electrical load for different electrical loading 0.1 Hz, 2kN loading

Recall Equation (3.63) which relates the power at electrical load to power available from PZT material with known excitation frequency, which is 0.1 Hz;

$$P_L = \left[\frac{1}{4} \right] \frac{V^2}{Z} = \left[\frac{1}{4} \right] \frac{1}{2} CV^2 \cdot f = 9.5 \mu\text{W} \quad (3.69)$$

Again the analytical prediction for power available at electrical load over predicts the value for 0.1 Hz case. It can be noted that the increase in frequency leads the prediction in better agreement; this is mainly because internal loss is relatively getting smaller.

The fourth set of the experiments performed with 0.5 Hz, 2kN loading condition. The results are summarized in Figs.3.26 and 3.27. With an increase of 5 times in the frequency with respect to third experiment the maximum power available at electrical load is measured to be $\sim 45 \mu\text{W}$.

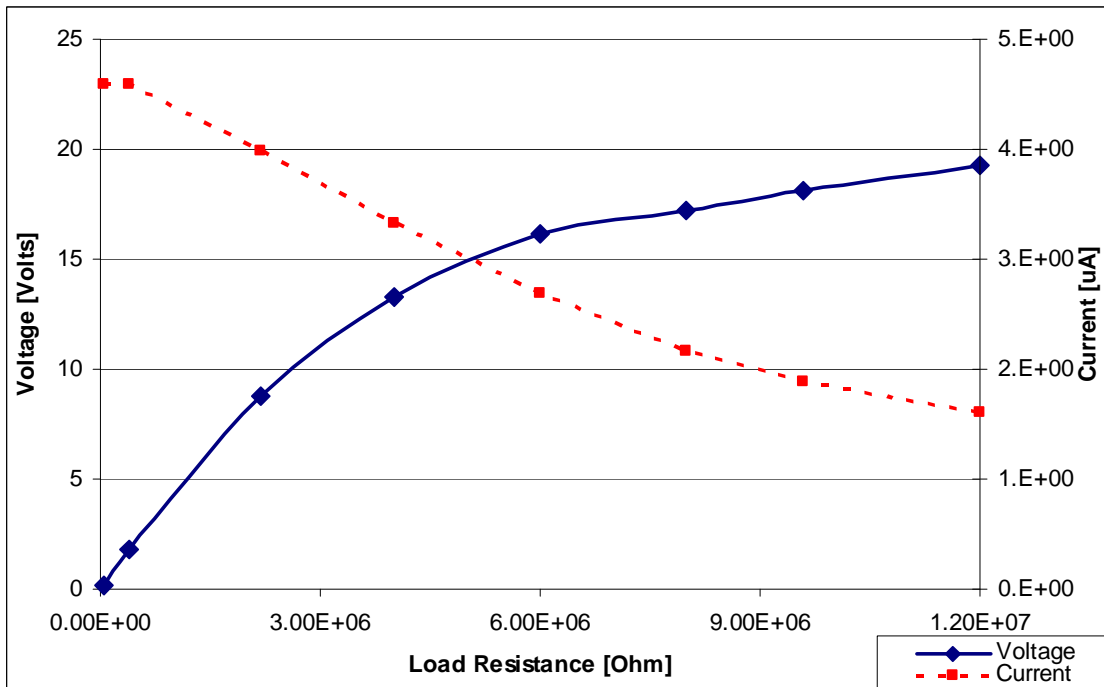


Figure 3.26. Voltage and Current response for 0.5 Hz, 2kN loading

As it can be seen from Fig.3.27, the maximum average power at the electrical load can be found at electrical load of $\sim 4 \text{ M}\Omega$ where the voltage is measured to be $\sim 13 \text{ Volts}$, and the current over the resistance, calculated by Ohm's Law, is $3.3 \mu\text{A}$. The average power is measured as

$$P_L^m = V_L^m \cdot I_L^m = 45 \mu\text{W}. \quad (3.70)$$

where superscript “ m ” represents the values are measured.

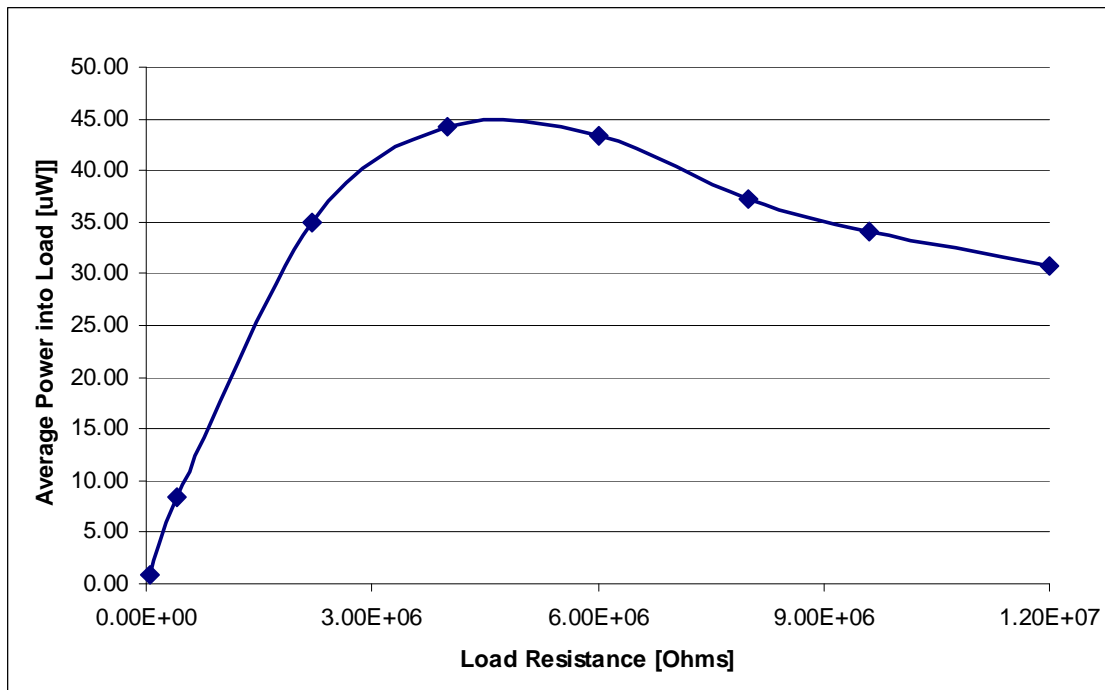


Figure 3.27. Average power at the electrical load for different electrical loading 0.5 Hz, 2kN loading

Recall Equation (3.63) which relates the power at electrical load to power available from PZT material with known excitation frequency, which is 0.5 Hz;

$$P_L = \left[\frac{1}{4} \right] \frac{V^2}{Z} = \left[\frac{1}{4} \right] \frac{1}{2} CV^2 \cdot f = 47.5 \mu\text{W} \quad (3.71)$$

Analytical prediction for power available at electrical load well predicts the value for 0.5 Hz case.

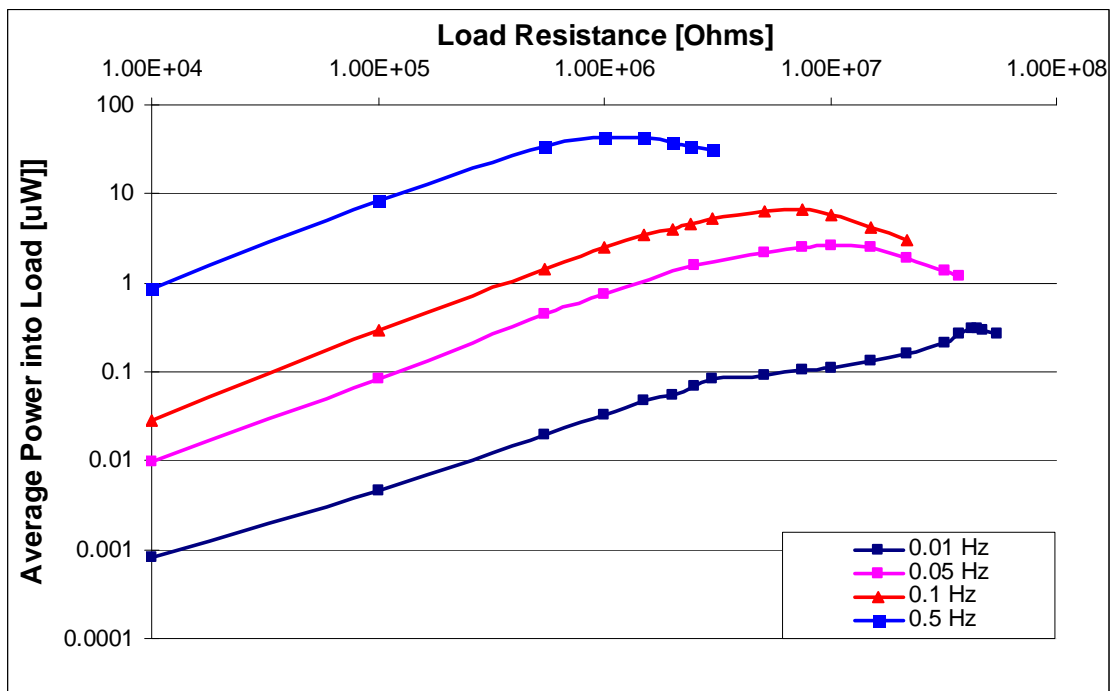


Figure 3.28. Average power at the electrical load for all frequency conditions in logarithmic scale, with respect to load resistance

All four experimental conditions which are at different excitation frequencies are summarized in Fig.3.28. Logarithmic scale is used to show all data in the same plot. As it can be seen higher the frequency the power available at the electrical load is higher. The impedance at the higher frequencies is also lower than the impedance values for lower frequencies. This study with piezoelectric material

gives an idea about the internal impedance of the piezoelectric material, in other words parameter identification of piezoelectric material is done by doing cyclic loading experiments with different frequencies and different load resistance. It can be noted again here that maximum power available at electric load when the impedance of the piezoelectric material matches with the connected load resistance.

Figure 3.29 shows the smaller frequencies; 0.01 Hz, 0.05 Hz and 0.1 for cyclic loading condition. This figure is not in logarithmic scale to give the reader better understanding of the relation between maximum power available at electrical load with respect to load resistance.

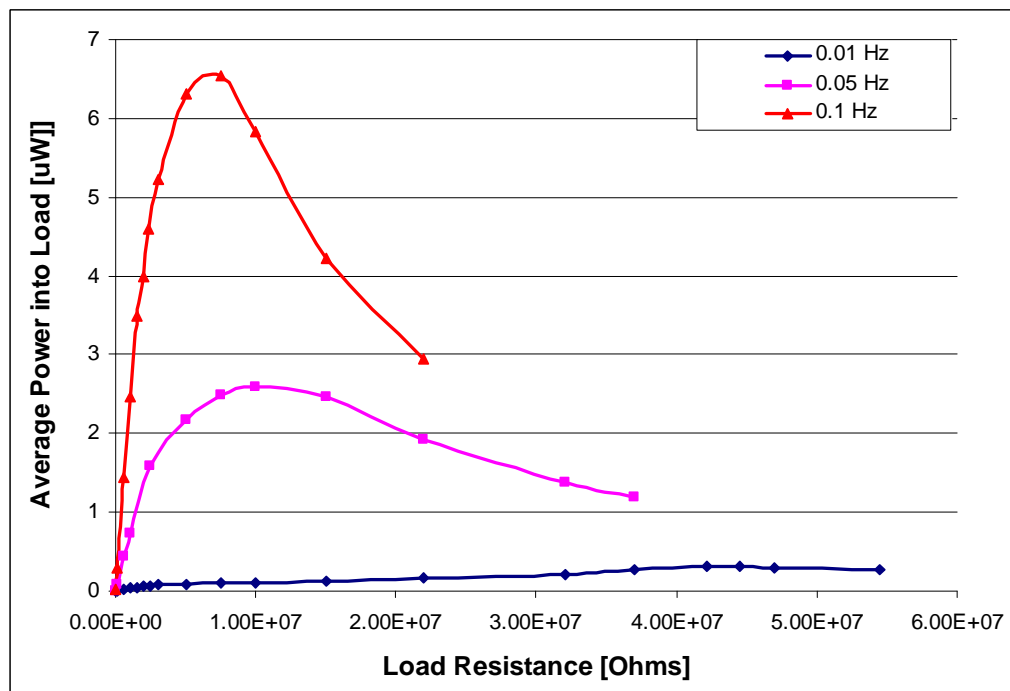


Figure 3.29. Average power at the electrical load for small frequency conditions with respect to load resistance

3.6. Experimental Procedure

Now that the modeling and parameter identification for materials that is used in the experimental study is discussed, we shall examine the experimental procedure that is done in order to simulate temperature cycling. Figure 3.30 shows the setup of the piezo-SMA module, two piece of PZT is used in the setup in order to prevent short circuit event in the electrical schema, positive poled are attached together, and the negative poles are connected via single electrode. With this simplification the use of a separate insulation material is no more necessary. Ni-51.2% Ti is used for SMA material, the transformation temperatures are given in Fig.3.14.

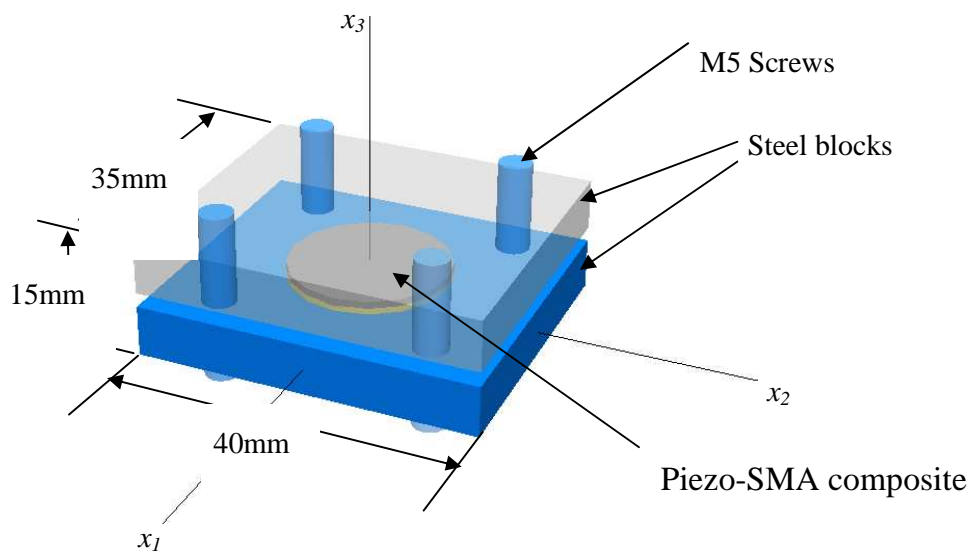


Figure 3.30. Schematic representation of the Piezo-SMA composite module in thermal energy harvesting experiment

In Fig.3.31 the setup for temperature cycle is shown. Two different temperature environments are prepared according to the SMA's transformation temperature.

Hot environment is controlled by simply on-off type thermostat; the temperature is set to be higher than the Austenite finish temperature. Cold bath is prepared with accordingly Martensite finish temperature. The specimen prepares as shown in Fig.3.30 is subjected to hot and cold environments, surface temperature of the SMA specimen is monitored with a thermocouple attached on the surface. Output voltage of the PZT is monitored by Data Acquisition System (DAQ). Electrical connection is prepared with respect to Fig.3.19. Here Z_L is a known electrical resistance element. The resistance value of electrical load is determined with respect to experimental study that is performed with piezoelectric material. The value of electrical load at which the maximum power is reached at the load is used for the experimental study performed in Thermal cycling simulations. Two PZT discs are used in the composite which are serially connected with positive electrodes are touching each other, and the negative electrodes are in contact with SMA and the fixture. This creates electrical insulation for the experimental set-up, can also be called self-insulation.

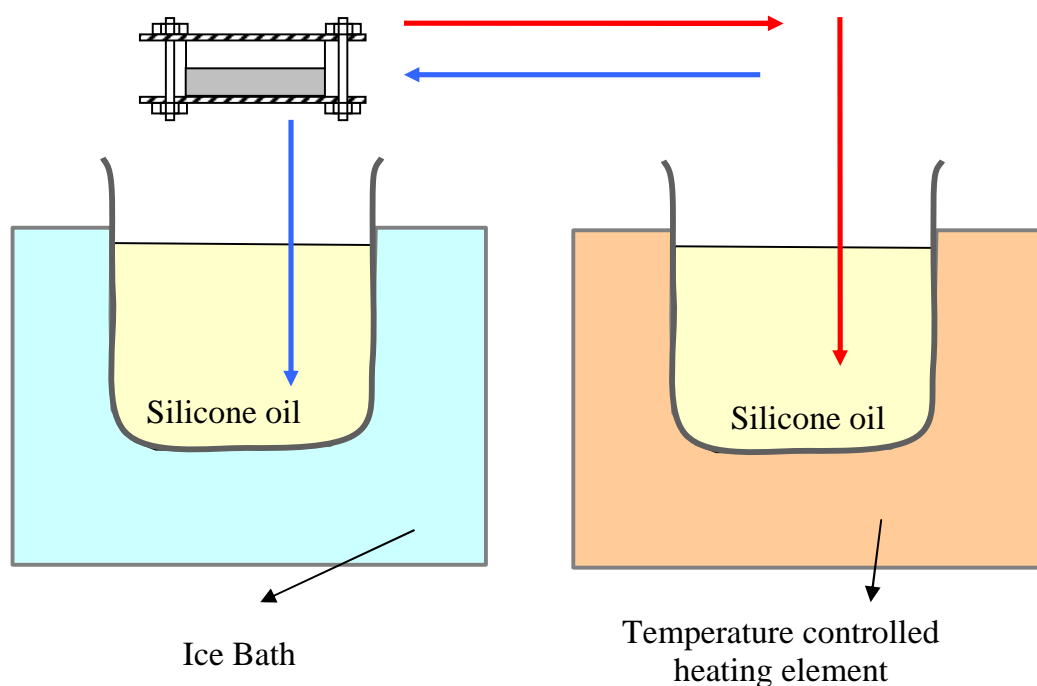


Figure 3.31. Temperature cycle simulation for piezo-SMA thermal energy harvester

Figure 3.32 shows the output results of the thermal cycling experiment of Piezo-SMA composite as an energy harvester. PZT module's electrodes are connected to DAQ system directly, which is not an accurate way to measure the voltage generated by the PZT material in general as we discussed earlier, the load resistance that is determined from impedance matching should have been used in this experiment. However this method provides a way to monitor the charge generated during heating and cooling periods of the thermal cycling process. As expected a positive voltage is generated during heating; SMA constrained recovery suppresses compressive stress in the system.

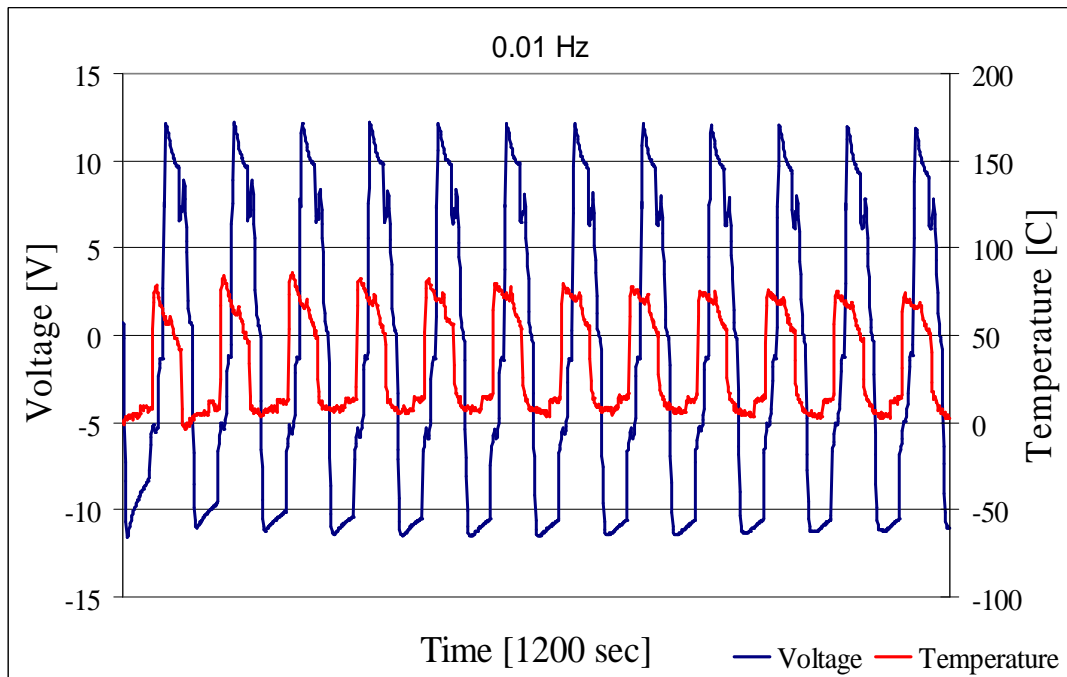


Figure 3.32. Output voltage and Temperature results for Thermal Cycling process, 0.01 Hz

Compressive stress on the PZT causes a positive charge accumulation. Poling direction of the PZT is also x_3 -direction which is the same direction of applied force due to compressive stress, therefore d_{33} effect takes place in heating process. Cooling on the other hand causes SMA to have martensitic transformation and the compressive stress is released in the system. The rate of change in the loading on PZT is opposite to poling direction and negative voltage generated.

Temperature is monitored by a thermocouple attached to the surface of the SMA. Monitoring the surface temperature is one of the solutions in order to check if the material is subjected a thermal cycle between critical transformation temperatures;

it this case Martensite finish M_F and Austenite finish A_F temperatures which are predetermined by DSC test as shown in Fig.3.14.

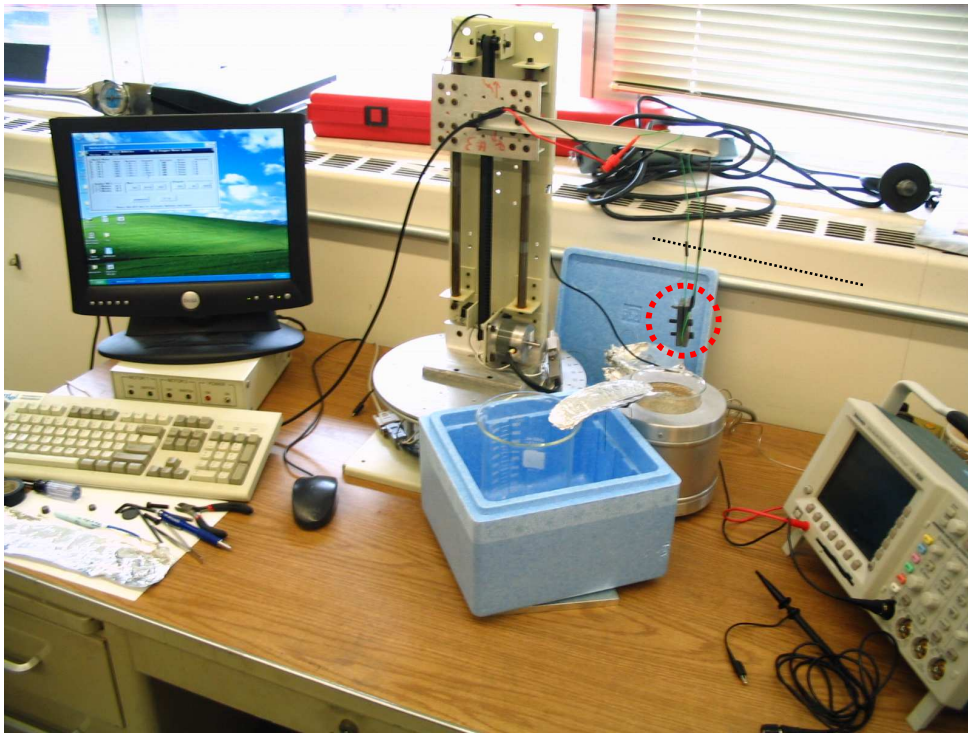


Figure 3.33. Experimental setup for piezo-SMA composite subjected to thermal cycling.

Experimental setup can be seen in Fig.3.23, thermal energy harvester, shown in circle is dipped in to hot and cold baths with the help of a robotic arm, as schematically represented in Fig.3.31. The robotic arm is driven by an open loop control system, the duration and the position can be determined accordingly by just changing the speed of the arm to simulate the thermal cycling process.

Cold and hot baths are placed next to each other in order to minimize the temperature variation during robotic arms travel between the positions. The

traveling time is minimized in order to have a better simulation. It is convenient to say that all the inertial effects limit the optimization of the temperature fluctuation.

Second sets of experiment is carried out with Instron mechanical testing machine Model 8521S, where the piezo-SMA composite is clamped with the help of the testing machine's compression punches and the control is switched to position control in order to have zero displacement boundary condition. Heating and cooling are applied to the composite with hot and cold air streams alternatively. The temperature is measured with a thermocouple, which is attached inside the SMA material from the contact free side. In order to have experimental comparison, piezoelectric material without SMA is also tested with the same loading boundary conditions. Both experimental setups are schematically shown in Fig.3.34. The piezoelectric material is electrically connected to a known electrical load. This resistance is selected based on impedance matching experiments for piezoelectric material shown back in Fig.3.28.

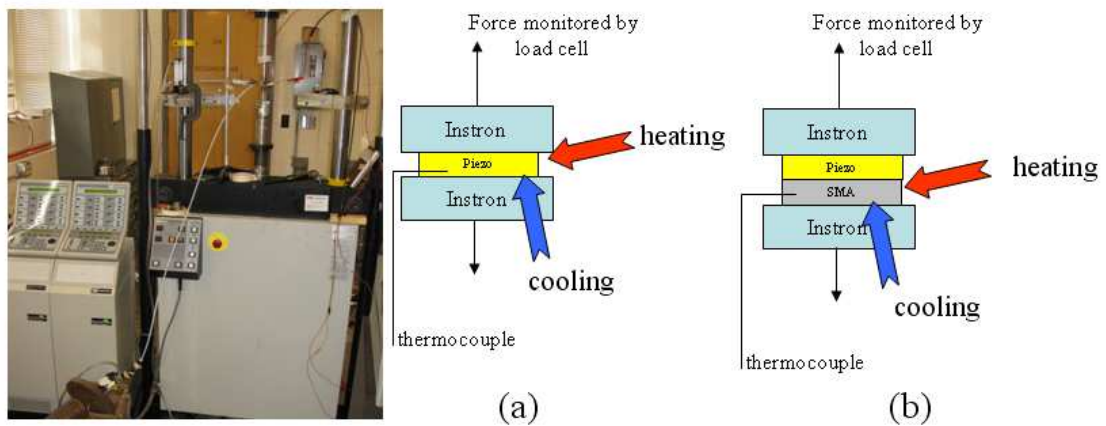


Figure 3.34. Experimental setup to simulate thermal cycling with the use of Instron machine that creates zero displacement boundary condition. (a) Piezo only, (b) Piezo-SMA Laminate

As expected, a positive voltage is generated during heating; SMA constrained recovery suppresses compressive stress in the system. Compressive stress on the PZT causes a positive charge accumulation. Poling direction of the PZT is also in the x_3 -direction, which is the same direction of applied force due to compressive stress; therefore, d_{33} effect takes place during the heating process. Cooling, on the other hand, causes SMA to have martensitic transformation and the compressive stress is released in the system. The rate of change in the loading on PZT is opposite to the poling direction and negative voltage is generated. Figure 3.35 shows the voltage (shown in solid curves) measured across the load resistance during the heating and cooling process for the 0.05 Hz and 0.1 Hz experimental studies. Temperature (shown in dashed curves) is also monitored by a thermocouple attached to the surface of the SMA.

Monitoring the surface temperature with a thermocouple is one of the solutions to check if the material is subjected to a thermal cycle between critical transformation temperatures, martensite finish M_F and austenite finish A_F temperatures, which are determined experimentally before and listed in Fig.3.28.

The result can be compared with two previously examined cases; analytical model to estimate the power available and results from parameter identification experiments performed with the same frequency. Overall study is summarized in the Table 3.2. Where the predicted power is based on Eq(3.63) and the measured values are recorded from piezoelectric material's parameter identification experiments and thermal fluctuation experiment performed with cold and hot bath/stream. Experimental results for both piezo-only and piezo-SMA cases are shown in the same table for 0.05 Hz and 0.1 Hz. The experimental study performed for 0.01 Hz is not tabulated since the piezo-SMA composite was not electrically connected to a known load resistance. The 0.5 Hz experimental study was not performed due to a limitation in experimental setup.

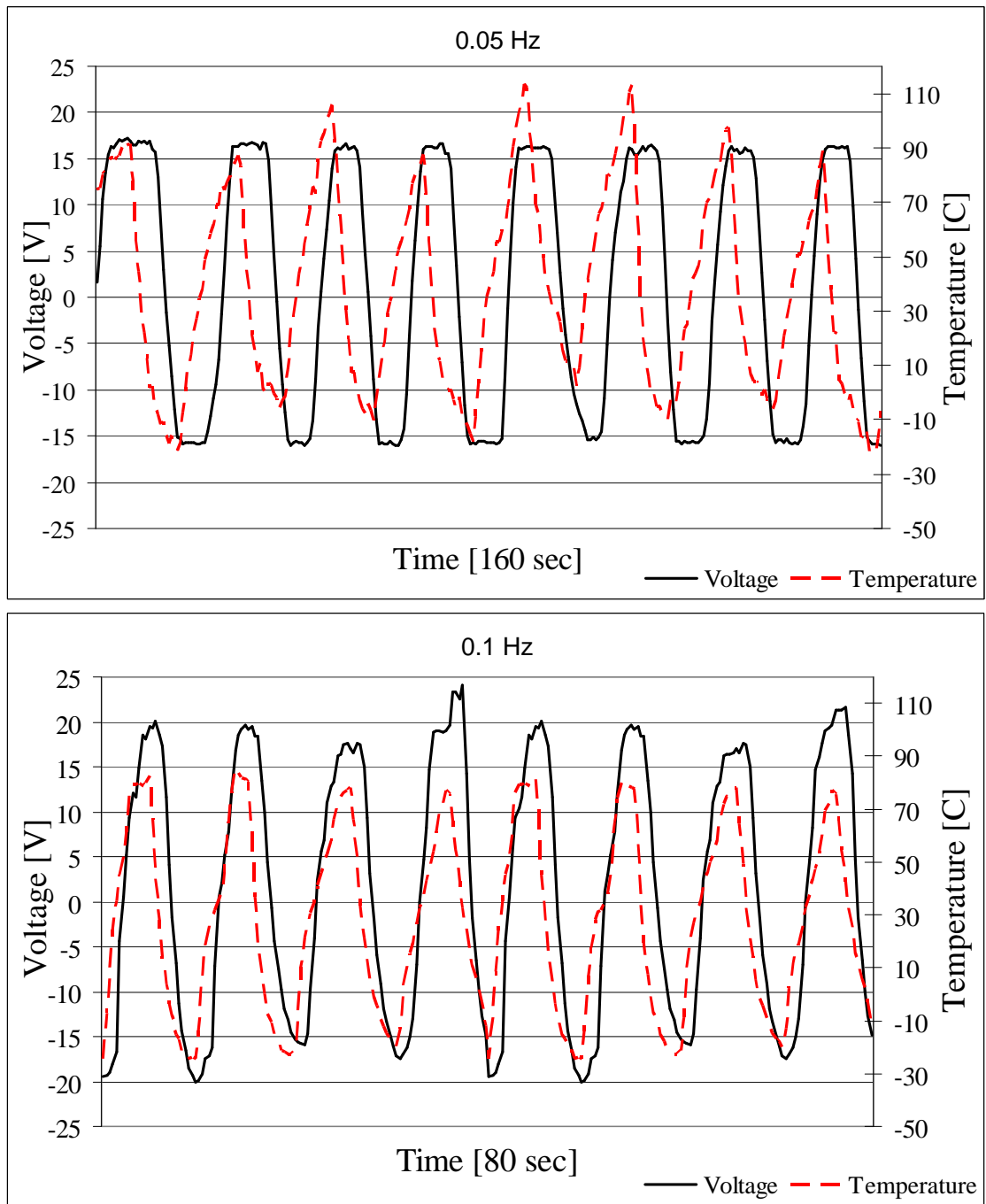


Figure 3.35. Temperature and Voltage response for 0.05 Hz and 0.1 Hz experimental study (Namli and Taya, 2011)

Table 3.2. Prediction and Experimental results for power available at electrical load

Frequency [Hz]	Predicted Power [μ W]	Power Measured with Piezo only Experiments [μ W]	Power Measured with Thermal fluctuation [μ W]	Power Measured by pyroelectric Effect [μ W]
0.01	0.95	0.31	*	-
0.05	4.75	2.6	3.6	0.12
0.1	9.5	6.4	8.6	0.19
0.5	47.5	44	-	-

* The power is not measured since no electrical load is used in thermal cycling experiment

Finally, the experimental data for sample temperature and the corrected value for stress from the load cell are plotted, as shown in Fig.3.36. An analytical model considering thermal expansion is also shown in the same plot. It is noted here that the analytical prediction of the cyclic loop in Fig.3.36 has sharp kink points as compared with the experimental curves; this is due to the phenomenological constitutive equations used, i.e., Eqs.(3.15) and (3.16), as the predicted curves shown in Figs. 3.16 and 3.17 exhibit similar sharp kinks.

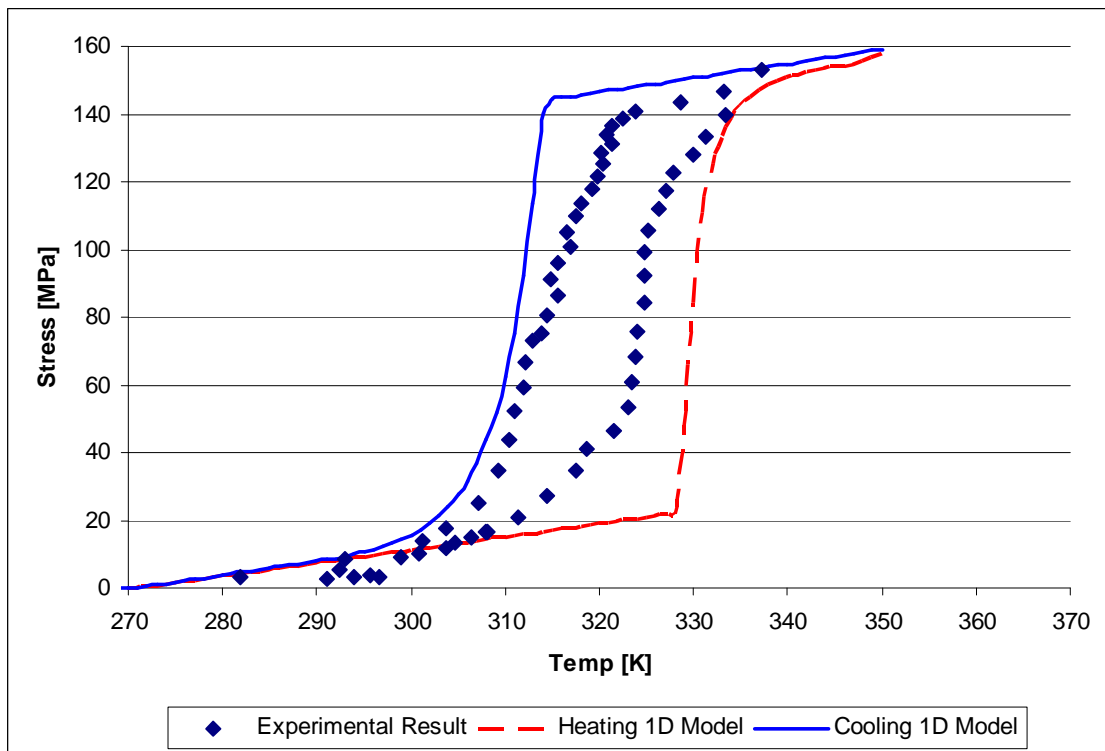


Figure 3.36. Experimental and analytical results for stress versus temperature (Namli and Taya, 2011)

Piezo-SMA, as a thermal energy harvester, is modeled with the 1-D serial model and the 3-D model with the Eshelby theory. Power available for electrical load is predicted. Experimental study for material characterization is performed. Temperature fluctuation is simulated in the laboratory; piezo-SMA is subjected to temperature fluctuation in different frequencies and experimental and predicted results are compared. Compressive stress induces during austenitic transformation due to heating in SMA phase together with the zero displacement boundary condition and then reduces while SMA transforms to martensitic phase during cooling. The change in the compressive stress is converted into electrical energy

by inverse piezoelectricity. The model predicts the available power according to material properties and thermal fluctuation. The impedance of the system is examined with different thermal fluctuating frequencies. Higher frequencies, which result in lower impedance, give higher available power to electrical loading. The experimental and predicted results are in agreement for higher frequencies while for lower frequencies of thermal fluctuation, the prediction is not accurate due to internal loss. Although we did not perform the experiment for higher frequencies beyond 0.5 Hz due to the limitation of the experimental set up, the power generation from the composite subjected to fluctuating temperature is expected to be increasing with higher frequencies.

Chapter 4. Conclusions

The goal of this research is to analyze to use of piezoelectricity and SMA properties in a composite material. A new concept of piezo-SMA composite is proposed as a high performance actuator material under bias stress and applied electric field. The best piezo-SMA composite design for achieving highest strain is use of 1-D parallel composite design of Fig.2.3. To this end, a new analytical model based on Eshelby theory is developed, which can account for anisotropic matrix and linear SMA superelastic behavior. The experimental study is also performed in order to manufacture such a composite where the bonding is required between two phases; piezoelectric material and SMA. Spark Plasma Sintering (SPS) machine is used to create such a bonding between two materials. In SPS process, pressure and temperature are controlled to achieve the best sintering condition. In addition to several SPS condition, three different design conditions are also carried out as discussed in Experiments section, Fig.2.7. The overall results for SPS are tabulated. In all cases, the bonding is examined by nondestructive tests.

Piezo-SMA composite as a thermal energy harvester is also examined in chapter 3 of the dissertation. Piezo-SMA composite subjected to fluctuating temperature uses synergistic effect of piezoelectrics and SMA which are connected in series. Temperature fluctuation induces large straining first in the SMA phase then immediately stressing to the piezoelectric phase, thus, inducing charge by direct piezoelectric effect. In order to make this problem more analytically tractable, two

models were developed, simple laminated 1-Dimensional model and 3-D model with Eshelby's theory. The material properties of SMA are examined. In order to determine the power available to electrical load from the PZT material in the piezo-SMA thermal energy harvester some sets of experiments are carried out with different frequencies. The method of energy conversion is suited to convert heat to electricity in situations where the heat is available at a fluctuating temperature.

REFERENCES

- Arsenault, R. J., Taya, M., *Acta Metall.* 35, pp. 651. 1997.
- Auricchio, F. and E. Sacco, "A One-Dimensional Model for Superelastic Shape Memory Alloys with Different Elastic Properties Between Austenite and Martensite", *International Journal of Non-Linear Mechanics*, Vol. 32, No. 6, pp. 1101-1114, 1997.
- Auricchio, F., L. Faravelli, G. Magonette and V. Torra, "Considerations on the Constitutive Modeling of Shape-Memory Alloys", *Shape Memory Alloys: Advances in Modelling and Applications*, pp. 125, 2001.
- Badcock, R. A., Birt, E. A., "The Use of 0-3 Piezocomposite Embedded Lamb Wave Sensors for Detection of Damage in Advanced Fiber Composites. *Smart Material and Structures*", 9: 291-297, (2000).
- Banno, H., "Recent Developments of Piezoelectric Ceramic Products and Composites of Synthetic Rubber and Piezoelectric Ceramic Particles. *Ferroelectrics*", 50: 3-12, (1983)
- Beeby, S.P., Grabham, N.J. and White, N.M., "Microprocessor implemented self-validation of thick-film PZT/silicon accelerometer", *Sensors and Actuators A* 92 (2001) 168-174
- Bhikkaji, B., Ratnam, M. and Moheimani, S.O.R., "PVDF control of piezoelectric tube scanners", *Sensors and Actuators A* 135 (2007) 700-712
- Birman, V., "Review of Mechanics of Shape Memory Alloy Structures," *Applied Mechanics Reviews*, vol 50(11), pp. 629-645, 1997.
- Boyd, J. G. and D. C. Lagoudas, "A Thermodynamical Constitutive Model for Shape Memory Materials. Part I. The Monolithic Shape Memory Alloy", *International Journal of Plasticity*, Vol. 12, No. 6, pp.805-842, 1996.
- Boyd, J. G. and D. C. Lagoudas, "A Thermodynamical Constitutive Model for Shape Memory Materials. Part II. The SMA Composite Material", *International Journal of Plasticity*, Vol. 12, No. 7, pp.843-873, 1996.
- Boyd, J. G., Lagoudas, D. C., "A Thermodynamical Constitutive Model for Shape Memory Materials - Part I: The Monolithic Shape Memory Alloy", *Int. J. of Plasticity*, vol 12, pp. 805-842, 1996.
- Brinson, L. C., "One Dimensional Constitutive Behavior of Shape Memory Alloys: Thermomechanical Derivation with Non-Constant Material Functions," *J. of Intell. Matl. Syst. and Struct.*, vol. 4:2, pp. 229-242, 1993.

- Chen, T. Y. (1994). Some Exact Relations of Inclusions in Piezoelectric Media. *International Journal of Engineering Science*, 32: 553-556.
- Cimaa, L. and Remiens, D., "Ferroelectric active sensors" *Sensors and Actuators A* 119 (2005) 120–127
- Damjanovic, D., *Ferroelectric, Dielectric and Piezoelectric Properties of Ferroelectric Thin Films and Ceramics*, Laboratory of Ceramics, Department of Material Science, Swiss Federal Institute of Technology-EPFL, 5 May 1998 Lausanne, Switzerland.
- Dana, S. S., Etzold, K. F. and Clabes, S., *Journal of Appl. Phys.* 69, 4398-1991.
- Deeg, W. F., (1980). *The Analysis of Dislocation, Crack and Inclusion Problem in Piezoelectric Solids*. PhD Dissertation, Stanford University.
- Dunn, M.L., Taya, M., (1993b). *Proc. Roy. Soc. London*. A443, 265.
- Dunn, D. L., Taya, M. (1993). Micromechanics Predictions of the Effective Electroelastic Moduli of Piezoelectric Composites. *International Journal of Solids and Structures*, 30: 161-175.
- Dunn, M. D. (1993a). Exact Relations Between the Thermoelastoelectric Moduli of Heterogeneous Materials. *Proceedings of the Royal Society of London A*, 441: 549-557.
- Dunn, M. D. (1993b). Micromechanics of Coupled Electroelastic Composites: Effective Thermal Expansion and Pyroelectric Coefficients. *Journal of Applied Physics*, 73(10): 5131-5140.
- Dunn, M. L. (1994). Thermally Induced Fields in Electroelastic Composite Materials: Average Fields and Effective Behavior. *Journal of Engineering Materials and Technology*, 116: 200-207.
- Dunn, M. L., Taya, M. (1993). An Analysis of Composite Materials Containing Ellipsoidal Piezoelectric Inhomogeneities. *Proceedings of the Royal Society of London, Series A*, 443: 265- 287.
- Dunn, M.L., Taya, M., (1993a). *Intl. J. Solids. Struct.* 30, 161.
- Engel, T. G. "Energy conversion and high power pulse production using miniature piezoelectric compressors," *IEEE Trans. Plasma Sci.*, vol. 28, no. 5, pp. 1338-1340, Oct. 2000.
- Eshelby, J. D., "The Determination of the Elastic Field of an Ellipsoidal Inclusion, and Related Problems," *Proc. Roy. Soc. London* vol. 241 , pp. 376-396, 1957.

- Gabbert, U., Kreher, W., Ko" ppe, H. (1999). Mathematical Modeling and Numerical Simulation of Smart Structures Controlled by Piezoelectric Wafers and Fibers. In: Proceedings of the EUROMAT '99 Conference, Munich.
- Glynne-Jones, P., Beeby, S. P., White, N. M., "Towards a piezoelectric vibration-powered microgenerator," IEE Proc. Sci. Meas. Technol., vol. 148, no. 2, pp. 68-72, 2001.
- Goldstein, D., A Source Manual for Information on NITINOL and NiTi, Naval Surface Weapons Center, Silver Spring, Maryland, February 1980.
- Grujicic, M., Zhao, C.L. and Austin, E.M., "Optimization of a piezoelectric bimorph grasper for use in minimally invasive surgical applications", Proc. IMechE Vol. 219 Part B: J. Engineering Manufacture, p 673-683, 2005
- Hagood N.W. et al., "Development of micro-hydraulic transducer technology," in Proc. 10th Int. Conf. Adaptive Structures and Technologies, Paris, France, Oct. 1999, pp. 71-81.
- Harrison, W.B. (1976). Flexible Piezoelectric Organic Composites. In: Smith, P.L. and Pohanka (eds.), Proceedings of the Workshop on Sonar Transducer Materials. National Research Lab, Washington, D.C., 257-268.
- Hatta, H., Taya, M., J. Appl. Phys. 59, 1851, (1986)
- Hatta, H., Taya, M., Intl. J. Eng. Sci. 24, 1159, (1986)
- Hugo Schmidt, V. "Piezoelectric energy conversion in windmills," in Proc. Ultrasonics Symp., 1992, pp. 897-904.
- Hwang, J. H., Yu, J. S. (1994). Electroelastic Eshelby Tensors for an Ellipsoidal Piezoelectric Inclusion. Composites Engineering, 4(11): 1169-1182.
- Ikeda, T., 1990, Fundamentals of Piezoelectricity, Oxford, Oxford University Press
- James , R. D., Wuttig, M. , (1998). Philosophical Magazine A, 77 . 1273-1299.
- James, R. D. Tickle, R., Wuttig, M. (1999). Materials Science and Engineering A, 273 ,320.
- Jeong, S., Ha, M. and Song, J., "Effect of geometry on properties of multilayer structure actuator", Sensors and Actuators A 116 (2004) 509-518
- Jiang , B., Batra, R.C. (2002). Continuum Mech. Thermodyn. 14, 87.
- Jiang, B., Fang, D. N., Hwang, K. C. (1999). A Unified Model for the Multiphase Piezocomposites with Ellipsoidal Inclusions. International Journal of Solids and Structures, 36(18): 2707-2733.

- Johnson, L., Gupta, A. K., Ghafoor, A., Akin, D. and Bashir, R., "Characterization of vaccinia virus particles using microscale silicon cantilever resonators and atomic force microscopy", *Sensors and Actuators B* 115 (2006) 189–197
- Kato, H. , Wada, T. , Tagawa, T. , Liang , Y., Taya, M. (2001). *Proc. of 50th Anni. of Japan Society of Mater. Sci.*, Osaka, May 21-26, 296.
- Kumar, S. and S. M. Sivakumar, "Numerical Simulation of Shape Memory Effect and Superelasticity in SMA Wires and Beams", *Proceedings of SPIE*, Vol. 5062, p. 936, 2003.
- Kuo , W.S., Huang, J.H. (1997). *Intl. J. Solids. Struct.* 34, 2445.
- Kymissis, J, Kendall, C., Paradiso, J.J., Gershenfeld, N., "Parasitic power harvesting in shoes," in *Proc. 2nd IEEE Int. Conf. Wearable Computing*, Los Alamitos, CA, Aug. 1998, pp. 132-139.
- Lagoudas, D. C., *Shape Memory Alloys: Modeling and Engineering Applications*, Springer Verlag, 2008.
- Leclercq, S. and C. Lexcellent, "A General Macroscopic Description of the Thermomechanical Behavior of Shape Memory Alloys", *Journal of the Mechanics and Physics of Solids*, Vol. 44, No. 6, pp.953-957, 1996.
- Li, J. Y., Dunn, M. L., 1998 *Phil. Mag.*, A77 (5), 1341-1350
- Li, J. Y., Dunn, M. L., Ledbetter, H. M., 1999, *J. Appl. Phys.*, 86(8), 4626-4634
- Li, J.F. , Takagi, K. , Terakubo, N., Watanabe, R. (2001). *App. Phys. Lett.* 79, 2441.
- Liang, C. and C. A. Rogers, "A Multi-Dimensional Constitutive Model for Shape Memory Alloys", *Journal of Engineering Mathematics*, Vol. 26, No. 3, pp.429-443, 1992.
- Liang, C. and C. Rogers, "One-Dimensional Thermomechanical Constitutive Relations for Shape Memory Materials", *Journal of Intelligent Material Systems and Structures*, Vol. 1, No. 2, pp.207-234, 1990.
- Liang, Y. , Kato, H. , Taya , M., Mori, T. (2001). *Scripta Mat.*, 45 , 569.
- Liang, Y., Kato H., Taya, M. (2000). *Proc. Plasticity '00: 8th Int. Symp. on Plasticity and Current Applications*, 193.
- Lin, C. T., Scanlan, B. W., Mcneill, J. D., Webb, J. S. and Li, L., *Journal of Mater. Res.* 7, 2546-1992.
- Marino, S., Castriota, M., Strangi, G., Cazzanelli, E. and Scaramuzza, N., "Asymmetric nematic liquid crystal cells containing lead zirconium titanate (PZT) films", *Journal of Applied Physics* 102, 013112, 2007

- Mikata, Y. (2001). *Intl. J. Solids. Struct.* 38, 7045.
- Mikata, Y., “Determination of piezoelectric Eshelby tensor in transversely isotropic piezoelectric solids,” *Int. J. of Engineering Science*, vol.38, pp. 605-41, (2000).
- Miyazaki S., Otsuka K., 1984 Mechanical behavior associated with the premartensitic rhombohedral-phase transition in a Ti50Ni47Fe3 alloy *Phil. Mag. A* 50 393-408
- Miyazaki S., Otsuka K., 1986 Deformation and transition behavior associated with the R-phase in Ti-Ni alloys *Metall. Trans. A* 17 53-63
- Mok, K. S., *Shape-Memory Alloys: Stress-Inducted Phase Transformation, Constitutive Model, and Nonlinear Finite-Element Formulation*, Ph.D. Thesis, University of Florida, 2003.
- Mori, T., Tanaka, K. (1973). Average stress in matrix and average elastic energy of materials with misfitting inclusion. *Acta Metallurgica*, 21: 571-574.
- Murray, S. J. , Frinelli, M. , Kantner, C. , Huang, J. K. , Allen, S. M., O'Handley, R. C. (1998). *Journal of Applied Physics*, 83 (1998) 7297.
- Namli, Onur C. and Taya, Minoru, “Design of piezo-SMA composite for thermal energy harvester under fluctuating temperature”, *Journal of Applied Mechanics*, v 78, n 3, p 031001 (8 pp.), May 2011
- Namli, Onur C.; Jae-Kon Lee; Taya, Minoru, “Modeling of piezo-SMA composites for thermal energy harvester” *Proceedings of the SPIE - The International Society for Optical Engineering*, v 6526, p 65261L (12 pp.), 2007
- Newnham, R. E., Bowen, L. J., Klinker, K. A., Cross, L. E. (1980). *Composite Piezoelectric Transducers. Materials in Engineering*, 2: 93-106.
- Newnham, R. E., Skinner, D. P., Cross, L. E. (1978). *Connectivity and Piezoelectric-Pyroelectric Composites. Materials in Engineering*, 2: 93-106.
- Odegard, G.M. (2004). *Acta Mater.* 52, 5315.
- Otsuka K., (1990). Introduction to the R-phase transformation *Engineering Aspects of Shape Memory Alloys* ed T W Duerig et al (London: Butterworth-Heinemann) pp 36-45
- Otsuka, K. and C. M. Wayman, *Shape Memory Materials*, Cambridge University Press, 1999.
- Otsuka, K., Wayman, C. M., *Shape Memory Materials*, Cambridge University Press, Cambridge, UK, (1998).

- Pearce, D.H., Hooley, A. and Button, T.W., On piezoelectric super-helix actuators, *Sens. Actuators A: Phys.* 100 (2002) 281–286.
- Qin, Q.H., (2004)., *Comp. Struct.* 66, 295.
- Rahman, M. A., \Patents on Superelastic Shape Memory Alloy", *Recent Patents on Mechanical Engineering*, Vol. 1, pp. 65-67, 2008.
- Record, P., Popov, C., Fletcher, J., Abraham, E., Huang, Z., Chang, H. and Whatmore, R.W., "Direct and converse magnetoelectric effect in laminate bonded Terfenol-D–PZT composites" *Sensors and Actuators B*, article in press
- Roundy, S., "The power of good vibrations," *Lab Notes-Research from the College of Engineering, University of California, Berkeley*, vol. 2, no. 1, Jan. 2002.
- Seffen, K.A., "Theoretical performance of a coiled coil piezoelectric bimorph", *Sensors and Actuators A* 133 (2007) 486–492
- Shenck, N. S., Paradiso, J., "Energy scavenging with shoe-mounted piezoelectrics," *IEEE Micro*, vol. 21, no. 3, pp. 30-42, May-Jun. 2001.
- Simsek, M., *Fracture Mechanics Analysis of Shape Memory Alloys Using Finite Elements*, Master's Thesis, Bogazici University, 2009.
- Sitti, M., "Piezoelectrically Actuated Four-Bar Mechanism with Two Flexible Links for Micromechanical Flying Insect Thorax", *IEEE/ASME Transactions on Mechatronics*, Vol. 8, No. 1, 2003
- Smith, W. A., Auld, B. A. (1991). *Modeling 1-3 Composite Piezoelectrics: Thickness-Mode Oscillations*, *IEEE Transactions on Ultrasonics, Ferroelectrics, and Frequency Control*, 38: 40-47.
- Sohmura, T., Oshima, R., Fujita, F.E. (1980). *Scripta Metallurgica*, 14 ,855-856.
- Souza, A., E. Mamiya and N. Zouain, "Three-Dimensional Model for Solids Undergoing Stress-Induced Phase Transformations", *European Journal of Mechanics A Solids*, Vol. 17, No. 5, pp.789-806, 1998.
- Takagi, K. , Li, J.F. , Yokoyama, S. , Watanabe, R. , Almajid, A., Taya, M. (2002). *Sci. & Tech. Adv. Mater.* 4, 55.
- Tanaka, K. and S. Nagaki, "A Thermomechanical Description of Materials with Internal Variables in the Process of Phase Transitions", *Archive of Applied Mechanics*, Vol. 51, No. 5, pp.287-299, 1982.
- Tanaka, K., "Thermomechanical Sketch of Shape Memory Effect: One-Dimensional Tensile Behavior," *Res Mechanica*, vol.18, pp.251-263, 1986.

- Taya, M. (2005). *Electronic Composites*, 1st ed. Cambridge University Press, Cambridge.
- Taya, M., Furuya, Y., Yamada, Y., Watanabe, R., Shibata, S., Mori, T., "Strengthening mechanisms of TiNi shape memory fiber/Al matrix composite" *Proc. SPIE* 1916, pp. 373-383, 1993
- Taya, M., Hayashi, S., Kobayashi, A.S., Yoon, H.S., (1990). *J. Amer. Ceram. Soc.* 73, 1382
- Taylor, G. W., Burns, J. R., Kammann, S. M., Powers, W. B., Welsh, T. R., "The energy harvesting eel: A small subsurface ocean/river power generator," *IEEE J. Ocean. Eng.*, vol. 26, no. 4, pp. 539-547, Oct. 2001.
- Uchino, K., and Ishii, T., "Energy Flow Analysis in Piezoelectric Energy Harvesting Systems", *Ferroelectrics*, 400, 1, pp.305-320, 2010.
- Ullakko, K. , Huang, J. K. , Kokorin , V. V., O'Handley, R. C. (1997). *Scripta Materialia*, 36 , 1133.
- Wang, B. (1992). Three-dimensional Analysis of an Ellipsoidal Inclusion in a Piezoelectric Material. *International Journal Solids and Structures*, 29: 293-308.

VITA

Onur C. Namli was born in Koycegiz, Mugla, Turkey, on 27 January 1979, the son of Seher & Nadir Namli and the brother of Ece Karaca. After completing his work at Kirikkale Anadolu High School, he went on to the Marmara University where he studied Mechanical Engineering and received his Bachelor of Science in June 2002. For the next three years he pursued a career in Mechanical Engineering at Assan Aluminum Company in Istanbul, Turkey. He also got his Master of Science Degree in Mechanical Engineering from Marmara University while working full time at Assan. He moved to Seattle in September 2005 to pursue PhD in Mechanical Engineering at University of Washington at Seattle.

Permanent Address: Sahrayicedit Mah. Ataturk C. Ucar S. Dilkum 2 D:40
Kadikoy, Istanbul, 34473, Turkey

Bilingual (Turkish and English), Japanese and German (Poor)

Software: MS Office, MATLAB, I-DEAS, ANSYS, AutoCad, Mathematica, CATIA, Pro/Engineer and NI-Labview.

Engineering Experience

Assan Aluminum Company, Istanbul, Turkey, 2002-2005

Leading company in sheet aluminum production market of Turkey and a subsidiary of Kibar Holding, a conglomerate composed of 10+ companies in various manufacturing and service industries.

Worked as Mechanical Maintenance and Manufacturing Specialist

Academic Experience

University of Washington, Seattle, WA

- Research Assistant at Center for Intelligent Materials and Systems Laboratory since January 2006.
- Instructor, College of Engineering, Introduction to Engineering Design, Fall 2008.
- Teaching Assistant/ Lab Instructor for several different classes;
 - Mechanical Engineering Department; Mechanics of Materials Lab, Kinematics and Dynamics, Elasticity/Elastostatics and Laboratory in Electronic Packaging and Materials.
 - Physics Department; Mechanics Lab, Basic principles of mechanics and experiments in mechanics for physical science and engineering majors.
 - Chemical Engineering Department; Introduction to Thermodynamics.

Education

University Of Washington, Seattle, WA

Graduate Student, PhD Candidacy granted working on Dissertation,

- Ph.D. Mechanical Engineering,
- Dissertation: “Analytical Modeling of Piezo-SMA Composite as an Actuator and Energy Harvester”, advisor Prof. Minoru Taya.

Marmara University, Istanbul, Turkey

M.S. in Mechanical Engineering, June 2005

- MS Thesis Project: “Kinematic and Dynamic Analysis of a Curved Link Robot Arm”, advisor Prof. Arif Adli

B.S. (Summa Cum Laude) in Mechanical Engineering, June 2002

Graduation Project: “Identification and PID Control of Three-Axis Cartesian Robot Arm”, advisor Prof. Arif Adli

LIST OF PUBLICATIONS

“Two-way reversible bending actuator based on a shape memory alloy/shape memory polymer composite”

Howie, Tucker; Liang, Yuanchang; Namli, Onur C. and Minoru Taya, Journal of Intelligent Material Systems and Structures, Submitted 24 May 2012.

“Design of piezo-SMA composite for thermal energy harvester under fluctuating temperature”

Namli, Onur C. and Taya, Minoru, Journal of Applied Mechanics, v 78, n 3, p 031001 (8 pp.), May 2011

“Design of Active Composites”,

Taya, Minoru; Namli, Onur C.; Howie, Tucker, “Design of Active Composites”, Final report for AFOSR, Defense Technical Information Center (DTIC), March 2009

“Modeling of piezo-SMA composites for thermal energy harvester”

Namli, Onur C. (Dept. of Mech. Eng., Washington Univ., Seattle, WA, USA); Jae-Kon Lee; Taya, Minoru, Proceedings of the SPIE - The International Society for Optical Engineering, v 6526, p 65261L (12 pp.), 2007

“Design of active composites”

Taya, Minoru; Gururaja, Shuasini; Namli, Onur C. and Lee, Jae Kon. Proceedings of the SPIE - The International Society for Optical Engineering, v 6526, p 652614 (7 pp.), 2007